Test background estimates for resonance measurements using a combination of mixed events and like sign pairs.

by

Fabian Alexander Jürgen Thiele

Master's Thesis in Particle Physics
Lund University

Supervised by
Associate Professor Dr. Peter Christiansen

Autumn Semester 2014

LUND
UNIVERSITY

Abstract

Two approaches for extracting properties of neutral resonances out of invariant mass distributions are presented: like-sign and event-mixing signal. Additionally a correction function based on event-mixing, aimed at revising detection differences of opposite charged particles, which is applied to the like-sign signal is tested. The analysis is conducted using pp collisions at 7 TeV and concludes an improved description of the residual background by the correction function. Furthermore no change of the resonance's extracted parameters is observed. The event-mixing method exhibits a problematic description of the background which is concluded in this thesis to be caused by the necessity of an azimuthal angle rotation for event-mixing.

Meinen geliebten Eltern
für die wundervolle Unterstützung.

Acknowledgement

First and foremost I would like to thank my supervisor Peter Christiansen for his unfailing support and many fruitful discussions. The idea to conduct this analysis as well as his constant input at any time was indispensable and much appreciated. Furthermore I was lucky enough to write my thesis within the ALICE group of the particle physics division in Lund. The experience I gained of this „look behind the curtain“ was wonderful and as informative as it could be. Therefore I would like to thank my office colleagues Tuva Richert, Martin Ljunggren and Vytautas Vislavičius for their company, their openness for discussions and the great time I spent with them at CERN. My gratitude extends to Anders Oskarsson and Evert Stenlund who were assisting me with valuable opinions and administrative matter and who I learnt a great deal of within the past two years.

Naturally I can not name all the people who enabled me to conduct my research. Separately I want to mention my friends with their never ending love and support. They can not be valued high enough and I am very grateful for being part of their lives.

Contents

List of Figures

CHAPTER 1

Introduction

The question whether matter can be divided infinite times has occupied scientists for more than two hundred years now. The aim to describe matter and its elementary constituents is the definition of particle physics. In order to examine these constituents matter is smashed together at large energy and the fragments analyzed. This is done, among other places, at the CERN organization in Geneva, Switzerland, using the Large Hadron Collider. Some of these basic constituents, quarks, reformat to hadrons: particles that consist of two or three quarks (at least to prevalent awareness). In experiments such as ALICE at CERN the particles created are measured using elaborate detectors. Along with problems occurring of tracks traversing detectors in dead areas there are particles which have a lifetime far too short to ever reach the first detector and therefore are naturally never detected. They are produced shortly after the collision and decay already before reaching the first possibility for detection. They are called *resonances* and their study is naturally difficult.

The most common way to detect them is to look at the decay products. As energy-momentum conservation has to hold, one can calculate the four-momentum of the possible mother particle for any number of particle tracks. Assuming two decay products one would calculate the four-momentum of a pair. Based on this, one can calculate the invariant mass which, as the name suggests, is the rest mass of the particle and invariant among any change of inertial system. As the uncertainty principle holds the mass of the resonance can vary, the shorter it lives the greater the variation. In a distribution of invariant mass one can find a peak due to the correlation of particles originating from such a decay. As this paragraph suggests the peak width and position is directly linked to the properties of the resonance which created it. Naturally the peak needs to be described mathematically to extract this information. Due to the statistical nature of the invariant mass distribution one needs to account for a certain background. The description of the background is what is the core topic of this thesis.

After describing the underlying theory including the standard model of particle physics and quantum chromodynamics in Chapt. 2 and introducing the detector systems used for finding the particles after a collision in Chapt. 3, two different ways for describing the background are presented. Additionally an attempt to further correct one of them is motivated and described. The results are then given in Chapt. 5 and conclusions are drawn in Chapt. 6. The two approaches in question are the like-sign method which eliminates possible correlation of a pair by their charge and event-mixing which does so by selecting particles from different events. The correction factor which is treated specifically in this thesis is applied to the like-sign method and supposed to correct for detector acceptance differences.

CHAPTER 2

Theory

2.1 The Standard Model of Particle Physics

> ,,Why does water not admit its bulk of every kind of gas alike? - This question I have duly considered, and though I am not yet able to satisfy myself completely, I am nearly persuaded that the circumstance depends upon the weight and number of the ultimate particles of the several gases [...]“ - John Dalton, 1805[1]

Introduction The ever recurring question of what material is made of is not a modern thought. Instead we know that as early as Democritus in the 5th century BC the idea of an indivisible unit of matter existed. John Dalton was revisiting the idea in the beginning of the 19th century by concluding the existence of ,,ultimate particles“ [1, p.286] while researching on absorption of gases by liquids. The following research and the phenomena that were able to be explained by atoms left no doubt about their existence and their nature.

But it was not for long until the idea of it being the smallest constituent of matter had to be given up. In 1897 the electron was discovered by Thompson [2] and the indivisibility of what we now call *atom* was gone. The question if such an indivisible particle exists still remains though and for more than a hundred years people have tried to find the smallest constituents of matter. The findings of this research during this period up until today include a variety of particles as well as different forces that let them interact. Extensive research has been conducted with large particle accelerators to define the fundamental particles and their way of interacting. The findings of this comprehensive research are included in a theoretical framework called the standard model.

Constituents The standard model is often visualized as in figure 2.1 and includes three groups of particles: quarks, leptons and gauge bosons. Gauge bosons posses, as the name suggests, integer spin and quarks and leptons half-integer spin which consequently characterizes them as fermions. All constituents, in the following referred to as *elementary particles* or simply *particles*, differ in at least one of the three defining properties: mass, spin or charge.

It is especially important to mention that most particle have an antiparticle that has the same mass and spin but opposite charge. Neutral particles can but do not need to be their own antiparticle as for an example the neutron and antineutron show. Furthermore the quark group has an additional property called *colour charge* or *colour* which we will more deeply treat in a later part of this section.

[1] [1, p.286]

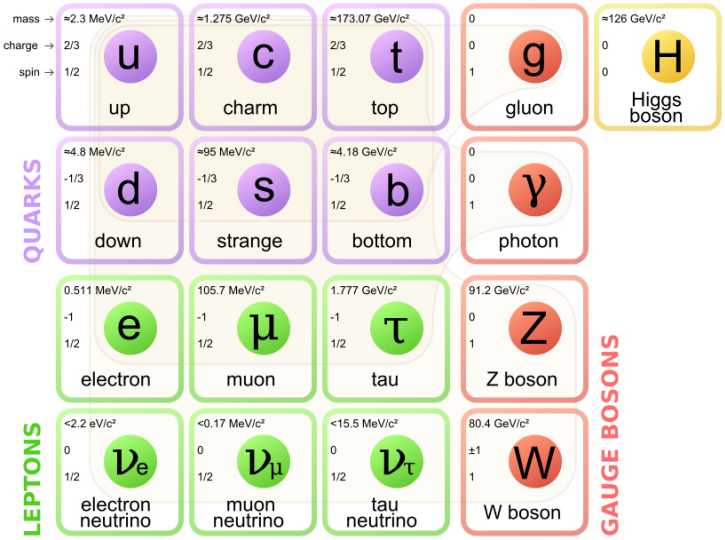

Figure 2.1: From [3], under creative commons license CC-BY[2]

Interaction An interaction between two elementary particles is a correlated change of at least one physical property of both particles. In order for an interaction to take place information about the two particles has to be transmitted. The role of this information transfer is played by the gauge bosons.

The standard model describes three out of the four known fundamental forces: Strong interaction, electromagnetic interaction and weak interaction. The last remaining one, gravitation, is not described. The strong interaction is intermediated by gluons, electromagnetic interaction by photons and the weak interaction by the $W^{\pm}$ and Z bosons. The *strength* of an interaction is the probability to which it occurs. It is described by the so called *coupling constant*.

2.2 Quantum Field Theory

Theoretical Framework The standard model itself, therefore the description of particles and their interaction, is a special formulation of a more general theoretical framework called Quantum Field Theory (QFT). It models particles as excited states of an underlying field. The often heard theories of quantum electrodynamics and quantum chromodynamics are applications of QFT that describe certain particles and their interaction. Quantum electrodynamics for instance describes one particle, the electron, and one gauge boson, the photon. It therefore makes use of two fields. An interaction between particles in QFT is the interaction between the fields. Fields are described generally via Lagrangians L that are the spatial integrals over the Lagrangian density $\mathcal{L}$ of the field. It has its origin in classical field theory where the action S for a field ϕ is observed within

$$S = \int L \, \mathrm{d}t = \int \mathcal{L}(\phi, \partial_\mu \phi) \, \mathrm{d}^4 x$$

and the principle of least action implies for an evolving system the Euler-Lagrange equation of motion for a field ϕ

$$\frac{\partial \mathcal{L}}{\partial \phi} - \partial_\mu \frac{\partial \mathcal{L}}{\partial(\partial_\mu \phi)} = 0 \tag{2.2.1}$$

where for multiple fields $\phi_i, i \in \mathbb{N} - \{0\}$ for each field holds this equation [4, p.15].

In order to describe particles the underlying field is quantized which is the assignment of discrete energy, momentum and spin to parcels of the field. Within the *second quantization* the fields are transformed into field operators and the amplitude, which can be considered as a

[2] https://creativecommons.org/licenses/by/3.0/deed.en

probability of occurence, of a four-dimensional movement of a quantized particle from $\vec{x} = (t_x, \boldsymbol{x})$ to $\vec{y} = (t_y, \boldsymbol{y})$ is described for a spin-0 particle by the Feynman propagator for Klein-Gordon particle

$$D_F(x-y) = \begin{cases} D(x-y) & ; \ x^0 > y^0 \\ D(y-x) & ; \ x^0 < y^0 \end{cases}$$

for

$$D(x-y) = \int \frac{1}{2E_{\boldsymbol{p}}} e^{-ip(x-y)} \frac{\mathrm{d}^4 p}{(2\pi)^4} \tag{2.2.2}$$

where E_p simply denotes the energy of a particle and a spin-$\frac{1}{2}$ particle is described by the Dirac Feynman propagator

$$S_F(x-y) = \int \frac{i(\not{p} + m)}{p^2 - m^2} \frac{\mathrm{d}^4 p}{(2\pi)^4}. \tag{2.2.3}$$

The $\not{p}$ denotes in the Feynman slash notation $\gamma^\mu p_\mu$ with γ^μ being the gamma matrices. Compare to [4, Ch. 2 & 3].

Perturbative QFT The Feynman propagators in (2.2.2) and (2.2.3) describe only a free particle without any interaction that is moving through space-time. They are used as a basis for performing perturbative quantum field theory in which multiple fields are interacting. It is this interaction that implies the exchange of gauge bosons as force mediators. The derivation of perturbative QFT reaches beyond the scope of this thesis and can be followed for instance in [4]. An illustrative example is the extension of the two-point correlation function

$$\langle \Omega | T \phi(x) \phi(y) | \Omega \rangle$$

which describes the propagation probability of a spin-0 particle from x to y for the interaction ground state of interaction theory Ω. Without interactions this is simply given by the Feynman propagator for a Klein-Gordon particle (2.2.2), as already mentioned before. T in this equation is the time-ordering symbol that allows a convenient treatment. Using the ϕ^4 theory one reaches at an expression that depends on the interaction Lagrangian, the Klein-Gordon Lagrangian, the free particle ground state and includes as well the exponential function. The exact description can be found in [4, (4.31)]. The perturbative nature originates from the approximation of the exponential function by a Taylor series. Only terms to a certain order are paid attention to where higher order corresponds to some kind of loops of particles while propagating from x to y.

The Lagrangian to describe our standard model hence separates the free and interaction part where each interaction (strong, electromagnetic and weak) is independent from the other. It may therefore be split up in various parts that describe certain particles and their respective interactions. Unifying the electrodynamic and weak interaction into the electroweak interaction would then give us a Lagrangian for the standard model of

$$\mathcal{L} = \mathcal{L}_{\mathrm{EW}} + \mathcal{L}_{\mathrm{QCD}} + \mathcal{L}_{\mathrm{H}} \tag{2.2.4}$$

where $\mathcal{L}_{\mathrm{EW}}$ denotes the Lagrangian of the electroweak theory, $\mathcal{L}_{\mathrm{QCD}}$ the Lagrangian of quantum chromodynamics and $\mathcal{L}_{\mathrm{H}}$ the Lagrangian of the Higgs-field. Again we neglected here the last force gravitation as so far no complete quantum theory exists to describe it and no mediating gauge boson (graviton), although it has been suggested, has been found.

Gauge Transformation Let $f : X \to Y$ be a function. f is called *transformation* if $X = Y$ holds. Let furthermore $\mathcal{L}$ be a Lagrangian. $\mathcal{L}$ is said to be invariant under transformation f if $\mathcal{L} \circ f$ fulfills the Euler-Lagrange equation (2.2.1). f is then said to be a *gauge transformation*. In case of $f(x) = f(y), \ \forall x \in X$ one speaks of a *global phase transformation*. In case $\exists x, y \in X : f(x) \neq f(y)$ it is called a *local phase transformation*. The problem with local phase transformations is, that additional terms might appear when differentiating that have to be canceled by additional gauge fields in order to be a gauge transformation.

Quantum Chromodynamics The theory of quantum chromodynamics describes the interaction that is mediated by the massless spin-1 gluon. It couples solely to colour charge similar to QED that treats solely the interaction of electrically charged particles. There are three colours, following the degree of the SU(3) gauge group, and colour charge is therefore arbitrarily set to: *red*, *green* and *blue*. As quarks are fermions the wavefunctions are antisymmetric regarding swapping of colours, just as it is required by the Pauli principle.

The in (2.2.4) mentioned Lagrangian of QCD is given by

$$\mathcal{L}_{\mathrm{QCD}}(\phi, A) = \bar{\phi}(i\gamma^\mu D_\mu - m)\phi - \frac{1}{4}F^a_{\mu\nu}F^{\mu\nu}_a$$

where $D_\mu = \partial_\mu - igT_aA^a_\mu$ is the covariant derivative and the field ϕ is the triplet of the three colour fields red, green and blue in the following way:

$$\phi = \begin{pmatrix} \phi_r \\ \phi_g \\ \phi_b \end{pmatrix}.$$

The given Lagrangian is invariant under global SU(3) transformations of the form

$$f(x) = e^{i\vec{h}\cdot\vec{a}}(x)$$

where $\vec{h}$ is a row vector containing one representation of the eight generators of the SU(3) and $\vec{a}$ a real column vector (element of $\mathbb{R}^8$). The „$\cdot$“ denotes the usual defined matrix multiplication. In order to make f a local gauge transformation for $\mathcal{L}_{\mathrm{QCD}}$ one needs to add terms to the Lagrangian. Therefore massless vector fields F_μ are introduced. For each of the entries in $\vec{h}$ one field is required: eight in total. The Lagrangian extends to

$$\mathcal{L}_{\mathrm{QCD}}(\phi, A) = \bar{\phi}(i\gamma^\mu D_\mu - m)\phi - \frac{1}{4}F^a_{\mu\nu}F^{\mu\nu}_a$$

where the field strength tensors are given by

$$F^{\mu\nu}_a := \left(\partial^\mu F^\nu_j - \partial^\nu F^\mu_j\right) + g_s f_{abc} F^\mu_b F^\nu_c \tag{2.2.5}$$

with g_s being fundamental colour charge and f_{abc} structure constants of SU(3) that arise because of the non-commutative character of the SU(3) group.

The vector fields F_μ represent the gluons that are the gauge bosons of the strong interaction and mediate it. They carry a colour charge and hence upon emission a particle changes its own colour charge. As they couple to colour, interaction between gluons (in contrast to photons) is possible. This can be seen in the last term of equation (2.2.5). Appearing virtual quark loops are having a screening effect on the strength of the strong interaction (similar to QED) whereas virtual gluon loops have an antiscreening effect (which is not possible for photons since they do not couple to each other). The antiscreening effect has the larger impact and hence the strong interaction decreases strength with decreasing distance leading to the phenomenon called *asymptotic freedom*.

In a atomic collision experiment with multiple nucleons for each projectile (as for instance lead-lead), shortly after the collision, a state of extreme density and temperature exists where quarks are thought to be deconfined. As the colour charges are moving around freely, a screening is exhibited in which the colours of the quarks are shielded from each other. The *quark-gluon plasma* called state starts to freeze out and hadrons are formed (at a temperature of around 150 MeV [5]). The freezing out is a hadronization of quarks and gluons and forms a narrow cone called *jet*. Many of the decay products, as they are very early created, may undergo scattering processes in the interacting hadron gas that is formed by the freeze out, and therefore show no properties that let us trace them directly to their parent hadron [6, p.2]. The accompanying reduction of energy is known as *jet quenching* and is one way of probing the quark-gluon plasma [7].

2.3 Resonances

Difficulties As mentioned in the previous section hadrons may decay via the strong interaction. As the coupling constant is large this is a dominant process and if a hadron is able to decay it does so very shortly after its creation. Hadrons that are created in hadron collision experiments and which can decay via the strong interaction are therefore decaying in short distance of the collision point. In fact the ϕ resonance has a lifetime of only $(1.55 \pm 0.01) \times 10^{-22}\,\mathrm{s}$[3], so that even relativistic ϕ mesons typically only travel on the order of hundreds of fm before decaying and the decay therefore occurs before reaching any detector. Although the inner tracking system (ITS) is able to localize the primary vertex (the spatial point at which the hadron decayed) with a resolution better than 100 µm [9] the actual particle can not be securely identified. Instead the decay products are measured as they are usually stable enough to be detected.

Invariant mass The *invariant mass* or often referred to as *rest mass* is a property of a particle that does not change under Lorentz transformations. It is defined as m_0 via the energy-momentum relation

$$m_0^2 c^2 = \left(\frac{E}{c}\right)^2 - |\,\vec{p}\,|^2.$$

Its importance arises as the measured momentum of a particle depends on the reference frame. As the mass can not always be determined with zero relative momentum to the observer, measuring its momentum for an arbitrary reference frame as well as its energy lets us determine its rest mass and consequently enables us to identify the particle.

2.4 Breit-Wigner Formula

Fitting Signal The resulting invariant mass distribution shows for resonances a peak at the position of their invariant mass. The height and width are also important as they give us information about the yield of the events (i.e. how many resonances have been created) and what the lifetime of the particle was. The signal peak is described by a continuous probability distribution given by the *Breit-Wigner-Formula*. In the future we will refer to it as the Breit-Wigner function. The probability density function is valid, just as the invariant mass, in all frames of reference and given by

$$P_f(E) = \frac{k}{2\pi} \frac{1}{(E - m_0)^2 + \Gamma^2/4} \tag{2.4.1}$$

with some factor k [10, p.354f.]. In figure 2.2 one can see the position of the peak to be at the invariant mass m_0 of the resonance and the width of the peak Γ at full width half maximum (FWHM). The width Γ directly translates to the lifetime τ via

$$\Gamma = \frac{\hbar}{\tau}. \tag{2.4.2}$$

Background In the previous paragraph we assumed for the Breit-Wigner function a signal that tends to zero away from the mass peak. When we look at invariant mass distributions this will not be the case and we have to describe the background, that means the part of the signal that is from uncorrelated particles (Sect. 2.5 will give a definition) that do not originate from the resonance that is analyzed. This can be done either with fitted functions or in a more physically meaningful way. Mistakes in the description of the background can obviously change the extracted parameters of the Breit-Wigner-Formula and therefore change the analyzed resonances invariant mass, its width and therefore as well its lifetime.

[3] Mass given by [8] and calculated via (2.4.2) into lifetime

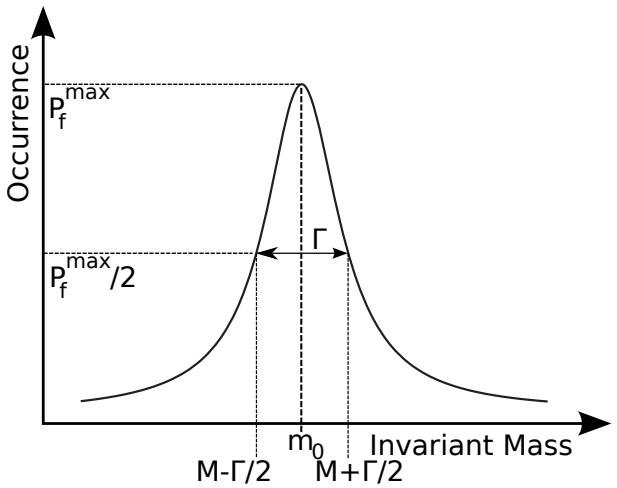

Figure 2.2: The Breit-Wigner probability density function. The width Γ at the FWHM is visible.

2.5 Particle Correlations

For the analysis conducted within this thesis it is crucial to be clear about the meaning of correlated and uncorrelated particles. The definition and basic idea follows [11] in which two particles are said to be *correlated* if and only if their momenta are correlated due to the resonance decay of interest. This means that both particles are decay products of the resonance decay. There surely are other „correlations“ that exist due to different conservation laws but for the time being are not denoted as such. They are based on conservation laws and are in general not to be neglected. For instance for the K^{*0} the conservation of strangeness implies the production of a particle with opposite strangeness quantum number. In turn the aforementioned definition implies that two particles are uncorrelated if at least one of them is not originating from the resonance decay of interest.

2.6 Background Estimation

Like-Sign Background When observing a neutral resonance decay into two particles the decay products must exhibit opposite charge (in the following referred to as unlike-sign) due to charge conservation. This means that when looking at two tracks with the same charge (in the following referred to as like-sign) one can securely state that they are not both originating from the resonance of interest. Consequently plotting only the unlike-sign pairs invariant mass distribution should exhibit a clear resonance peak and plotting the like-sign pair invariant mass distribution should not exhibit such a peak. We can therefore use the like-sign signal in order to estimate the background of the resonance decay.

As already defined in Sect. 2.3 the background consists of particles of the matching type, for instance kaons or pions, that though they do not originate from a resonance decay can still show a rise in the invariant mass distribution. Subtracting therefore the like-sign signal subtracts certainly uncorrelated background (as the resonance was assumed to be of neutral charge) but as well signal from particle pairs where only one partner originates from a non-resonant decay. Since it is impossible to exclude that the partners do not come from the resonance decay statistical measures need to be taken in order to get a clear picture of what is background and what already belongs to the resonance invariant mass peak. This thesis aims, among other things, to shed light on the question whether the application of a correction function as in 2.7 is beneficial to these statistical methods.

Event-Mixing Background Instead of simply looking at uncorrelated signal from the same event it might be useful to take into account detector inefficiencies, track bending effects of differently charged particles and other unforeseen complications. In order to achieve this one can use the event-mixing method. It uses for the invariant mass distribution for every pair only tracks from different events. This way one can be sure not to have selected correlated tracks as they are from different events and can not correlate in any way. For acquiring statistics this mixing can not only take place between two events but for an arbitrary number. When making use of for instance five events, every track from a previously selected event gets mixed with every track of these five other events. Assuming a constant number N of tracks per event this implies that for one specific track not $N-1$ pairs are added to the distribution that contain it (single event) but instead $5N$ events are added.

Due to the consequently considerably larger event mixing sample one has to normalize it before subtracting it from the unlike-sign single event mass distribution. Here again various methods are applied, one being the simple division by the number of mixed events (although this can just be a rude approximation as the track number in each event surely differs, sometimes by a large amount) another being based on the observance that without a resonance the two signals should exhibit after normalization the exact same shape. Therefore an integration over a range of bins far away from the resonance peak and the subsequent comparison of integrals should give a good normalization ratio (Compare [11, p.548]).

2.7 Correction Function

As we will see in more detail in 3.2 but mention it already now, the tracking system is placed within a magnetic field. Tracks that traverse it get bent depending on their charge in one of two directions. Related to this a variety of detection problems may arise with one of them being possible detector errors or dead areas.

In order to correct for these differences one can look at the signals from event-mixing. If the like- and unlike-sign signal are handled separately, the number of unlike-sign pairs and like-sign pairs for every bin can be compared easily. If no acceptance effects are observed the ratio between the two should be equal to one as in the event-mixing signal by construction there are no correlated signals.

A candidate for this correction that has been under close investigation as a part of this thesis is the aforementioned ratio

$$R = \frac{N^{\mathrm{EM}}_{\mathrm{unlike}}}{N^{\mathrm{EM}}_{\mathrm{like}}}. \tag{2.7.1}$$

The like-sign signal is as a background estimation predestined to use this correction function as it does not include any information about detector differences nor does its analyzed data include this information. Applying a physical meaningful correction could eventually increase the quality of the background fit.

An example of the correction function is given in figure 2.3. Here one can observe for the mass peak position of the ϕ a correction of about $11-12\,\%$ which is significant. The existence of a not-negligible correction in certain p_T bins motivates a closer analysis of its effects.

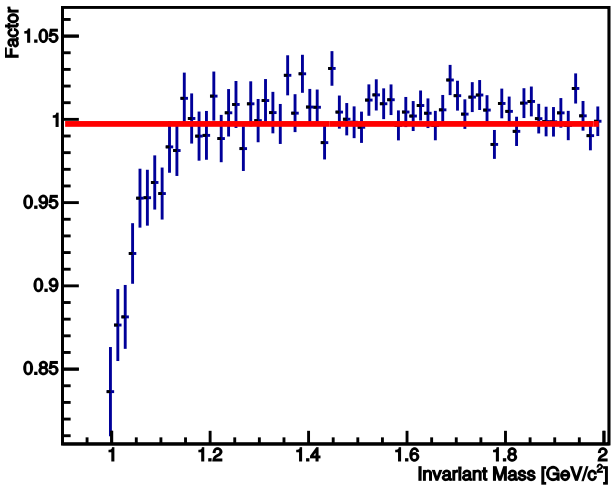

Figure 2.3: Correction function plotted for the invariant mass distribution of ϕ (1020) for p_T between 4 – 10 GeV/c. The red horizontal line denotes the average of the correction function over the whole mass distribution range.

CHAPTER 3

The ALICE Experiment at the Large Hadron Collider

A large ion collision experiment (ALICE) is an international collaboration of 37 countries with over 1500 members [12]. It is hosted at the European Organization for Nuclear Research (CERN) and is one of the largest experiments that are part of the Large Hadron Collider. Its goal is the creation and analysis of the quark-gluon plasma, a state of extreme density and temperature.

3.1 The Large Hadron Collider

The Large Hadron Collider (LHC) is a colliding-beam particle accelerator at CERN. Its main component is a 26.7 km circumventing underground synchrotron under the Swiss/French border. Accelerated particles are either protons or stripped lead atoms that are brought to collision at various points of the synchrotron ring. Large detector experiments are placed at the detector points that allow the analysis of the collision products.

In *run 1* the nominal beam energy for protons was for 2010 a total of 7 TeV [13] (used for this thesis, see Sect. 4.1, in 2012 it was 8 TeV) while after a two year stop in March 2015 *run 2* will produce 13 TeV proton-proton collisions [14]. A 8.33 T strong magnetic field is positioning the projectiles on their trajectory within the synchrotron ring where 2808 bunches with 1.15×10^{11} protons each circumvent the synchrotron 11 245 times per second. A system of linear accelerators and smaller synchrotrons is used to bring the protons up to speed before injecting them via sophisticated injection systems (kicker magnets) into the LHC main synchrotron.

The LHC can deliver a luminosity for pp collisions of 10×10^{34} cm^2/s which directly translates into the number of collisions per second. It can be calculated via

$$L \cong F \cdot \frac{N^2}{t \cdot S_{\text{eff}}}$$

where L denotes the Luminosity, F the geometric luminosity reduction factor that arises from the crossing angle (the larger the crossing angle of the two beams the smaller is the overlapping area of the two beams and hence less collisions occur), N the number of particles in a bunch, t the time spacing between the bunches (for run 1 this was 25 ns) and finally S_{eff} the effective section of the collision which depends on the cross-section of the beam and can be calculated via $S_{\text{eff}} = 4\pi \cdot \sigma_x \cdot \sigma_y$, where σ_x, σ_y is the width of the beam in the horizontal, vertical direction at the interaction point. For run 1, the geometric luminosity reduction factor was approximately 0.95.

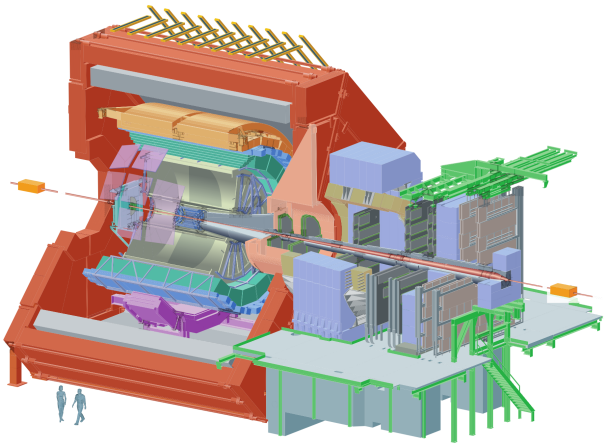

Figure 3.1: The ALICE experiments schematic layout. Taken from [15].

3.2 The ALICE Detectors

The detectors used in this thesis: Time Projection Chamber, Time-of-Flight detector and internal tracking system are presented. They are part of the central barrel and placed within a magnetic field of 0.5 T. A schematic layout of the whole ALICE experiment can be found in figure 3.1.

3.2.1 The Time Projection Chamber

The Time Projection Chamber (TPC) is used in this analysis especially for extracting information about the specific energy loss per unit length, momentum and to avoid fake tracks by looking at the path a track took inside the TPC. Corresponding to the track path important values as polar and azimuthal angle of the track as well as the collision position are determined. As later described further the ITS can improve these values as it is positioned closer to the collision point (see Sect. 3.2.3).

The TPC consists of a cylindrical chamber with Multi-Wire Proportional Chambers (MWPC) at each end. The cylindrical chamber is split into two halves by a central membrane. A high voltage is applied creating an electric field between the central membrane and each end. When a particle traverses the gas filled cylindrical chamber (the gas mixture used consists of $Ne(85.7\,\%), CO_2(9.5\,\%)$ and $N_2(4.8\,\%)$), it loses energy via interaction with the gas. The liberated electrons will travel along (called drifting) the electric field towards the MWPC where they are detected. The central membrane enables a maximum drift time of 94 µs where a short drift time is certainly beneficial to the amount of events that can be analyzed during a run time. Each of the end planes possesses 18 inner and 18 out chambers with a total of 159 pad rows. The spatial positions x and y can be determined by the channel position which registers the electron. As the drift velocity of the electrons in the gas chamber is constant, one can further determine the spatial z-position of the point it was liberated at by measuring the time it took to reach the channel. Figure 3.2 displays the field cage of the TPC at ALICE.

The TPC installed at ALICE measures a radius of 2.78 m whereof an active volume is covered by the radius between $0.85 - 2.47$ m (see figure 3.2). The length of the TPC measures 5.1 m and has a total of $90\,\mathrm{m}^3$ which enables tracking of charged particles in a 2π azimuthal angle and a $|\eta| < 0.9$ polar angle, compare [17]. The polar angle is commonly given as value of pseudorapidity η where

$$\eta := -\ln\left(\tan\left(\frac{\theta}{2}\right)\right)$$

with $\theta = \sphericalangle(\vec{p}, \vec{z})$ for the particles momentum $\vec{p}$.

An electron reaching the MWPC creates an avalanche with a gain of 7000 - 8000 as stated in [16] which induces a signal on a given pad-row. If a sufficiently high charge is induced, in 5 pads

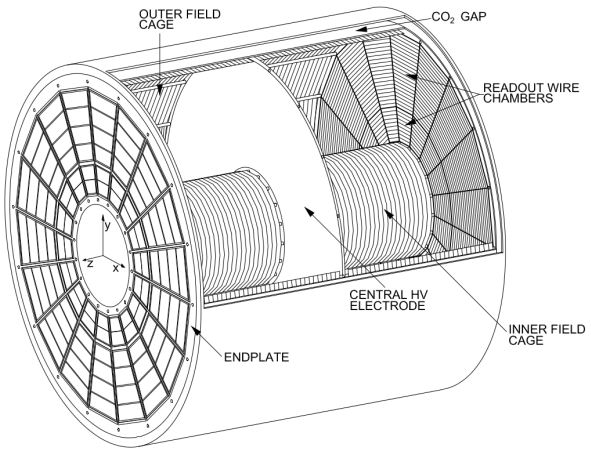

Figure 3.2: The TPC field cage. The end plates are MWPC. Taken from [16].

in the direction of the wire and over a certain amount of time (5 bins) it is called a „cluster“ [18]. A maximum of 159 clusters is possible for a single track. For particles with low momentum that do not manage to leave the TPC less clusters are expected. In order to avoid fake tracks it is therefore recommendable to filter for the ratio of clusters traversed/reconstructed (see Sect. 4.1).

The TPC is, as already mentioned, used for determining a particles trajectory, measure its momentum and its average specific energy loss per unit path length $\langle \mathrm{d}E/\mathrm{d}x \rangle$. The resolution of the determination of momentum is mentioned in 6.2.4. The energy loss of a particle is a statistical process described by the Landau distribution. To suppress fluctuations of the energy loss in the tail, the mean energy loss of the track, misleadingly denoted $\langle \mathrm{d}E/\mathrm{d}x \rangle$, is calculated as the mean of the 60 % smallest cluster charge values. It reaches a resolution of about 5 % [16]. Based on the information the TPC provides one can conduct particle identification on a track-by-track basis as described in 3.3. Especially at low p_T the specific energy loss per unit length can be used to differentiate between the different types of particles as is visualized in figure 3.6.

3.2.2 The Time-Of-Flight Detector

The Time-Of-Flight (TOF) detector determines, as the name suggests, the time a particle takes to travel from the collision point to the detector location. It consists of 18 azimuthal sectors that are positioned outside of the ITS, TPC and TRD systems at a distance of $370 - 390$ cm to the beam. Manufactured in a projective geometry along the beam direction (usually called $\vec{z}$) in order to minimize time deviation measurements for spatial offset tracks it delivers a time resolution of at least 50 ps [17]. The azimuthal angle between $260 - 320°$ for a polar angle of $\eta \approx 0$ does not exhibit any TOF sectors in order to save material for the underlying photo spectrometer. In polar angle direction the TOF detector covers an angle of $|\eta| \leq 0.9$.

Each azimuthal sector consists of 91 multi-gap resistive plate chambers (MRPCs) where each MRPC possesses five gaps. The MRPCs are double stacked and an example of a three gap is exhibited in figure 3.3. The gaps are filled with gas and a high voltage is applied only to the outer electrodes. A particle traversing a gap leaves a trail of ionisation that is in the electric field multiplied and creates an avalanche. The signal induced is picked up the by the cathode and anode pickup electrodes and simply is formed by the sum of the charge movements in each gap. The signal from the MRPC is then amplified and discriminated (compare to [19]) to extract the information of a traversing particle. Upon signal the current time is subtracted by the interaction time which in ALICE is determined for instance by a dedicated Cherenkov detector [20] to gain the time-of-flight.

The TOF allows a 3σ separation of pions and kaons up until 2.5 GeV/c and a separation of protons and kaons up until 4 GeV/c [15]. In the setup of 2011 which was as well used for the

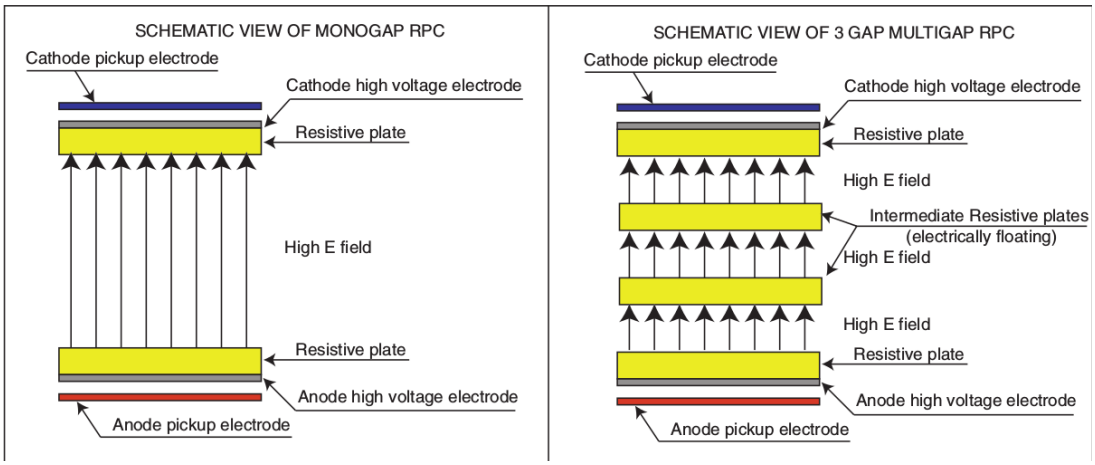

Figure 3.3: MRPC scheme of a monogap resistive plate chamber and a MRPC with three gaps. Figure taken from [21].

data that this thesis is based on about 9.6 % of all channels of the TOF where inactive [17]. An example of the TOF plotted versus the momentum can be found in figure 3.5. The different bands are corresponding to particle types and are clearly visible in the figure. Following [20] the tracks located outside of the bands are due to a wrongly assigned TOF signal.

3.2.3 The Inner Tracking System

The inner tracking system consists of six cylindrical layers that are mounted in a distance of 3.9 – 43 cm to the beam pipe. It is used foremost to extend the tracks measured by the TPC closer towards the collision vertex but improve as well the resolution of momentum, radial and azimuthal angle determination. Furthermore the two most inner layers are contributing to trigger decisions. In case a track is located in a dead area of the TPC (or low momenta of $p < 200\,\mathrm{GeV/c}$ that do not reach it), the ITS can act as a standalone tracker as well [17].

The six layers are consisting of two silicon pixel detector (SPD), two silicon drift detector (SDD) and two double-sided silicon strip detector (SSD) layers. The SPD can handle track densities up until 50 tracks per square centimetre. Every 100 ns a signal contributes to trigger decisions that among others contains information about the track multiplicity of the event (compare [17] and [22]). The dector consists, as the name suggests, of two dimensional matrices of reversed bias silicon detector diodes. The SSD consists of 1698 modules which each has 1536 silicon strip detectors. They are mounted at a distance of about 38 cm to the beam axis and cover an area of $2.2\,\mathrm{cm}^2$ for the inner and $2.8\,\mathrm{cm}^2$ for the outer layer, respectively [23]. Finally the SDD is, as the name suggests, consisting of silicon drift detectors and supplies together with the two previous layers information about the specific energy loss of a particle in the non-relativistic $1/\beta^2$ region. All layers supply two dimensional information of tracks traversing.

The setup established for run 1 showed 80 % of the SPD and about 90 – 95 % of the SDD and SSD modules to be active [17].

3.3 Particle Identification

As figure 3.4 shows particle identification (PID) is necessary to conduct invariant mass distribution analysis since otherwise no peak is visible. This is due to the statistical blurring out of the resonance peaks while combining all possible pair combinations of the tracks. The particle identification for this thesis makes use of the in 3.2 mentioned TPC, ITS and TOF detectors. Comparing the expected TOF with the actual TOF for a specific particle mass and momentum and the knowledge of its trajectory lets us easily determine a tracks particle type. The mass of

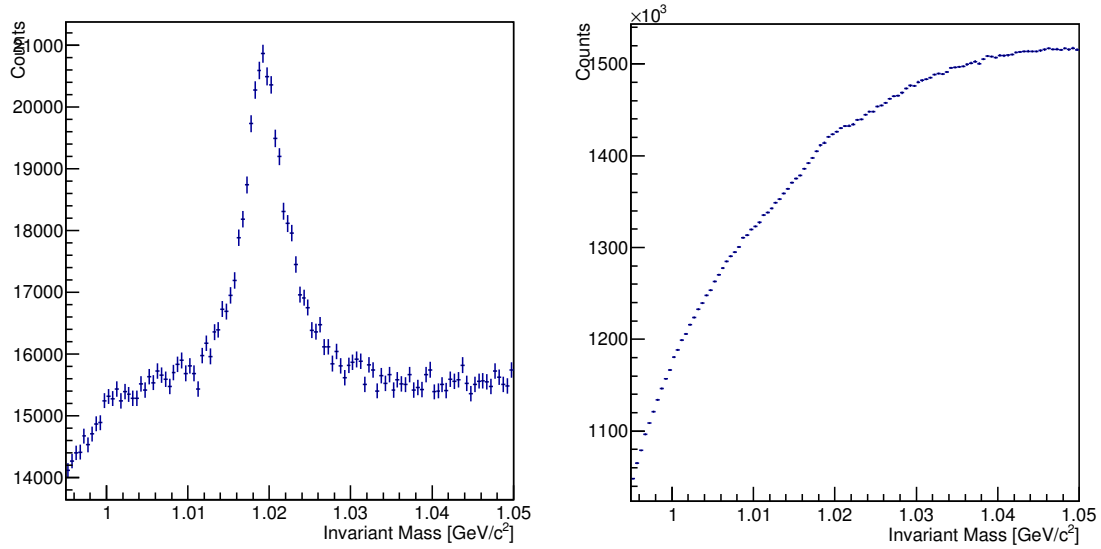

Figure 3.4: Both plots show the invariant mass area around the $\phi(1020)$ mass peak. For the left plot PID adjusted to kaons has been conducted. The right plot shows the invariant mass distribution without PID.

the track is determined therefore through velocity and momentum:

$$m^2 = |\,\vec{p}\,|^2 \cdot \left(\frac{1}{\beta^2} - 1\right).$$

Here use has been made of the integrated path length L that has been measured and the time of flight t. β is then determined by looking at the ratio $\frac{L}{t}$. An example of the β distribution in dependence of momentum can be found in figure 3.5.

For intermediate transverse momentum (p_T) in the range that we observe (up until 2 GeV/c) a 3σ separation using the TOF detector of pions, kaons and protons is possible[19]. Especially for low p_T though, no TOF information exists due to the fact that the particle does not reach the TOF detector, which sits outside of ITS, TPC and TRD. In order to increase the amount of identified tracks that can be used for invariant mass calculations and therefore improve the statistical meaning of the results (larger numbers imply less statistical fluctuations and hence errors), the TPC detector as well as the ITS detector are used to identify these low p_T pions and kaons. This is achieved by comparing the specific energy loss per unit path length (from now on denoted as specific energy loss or simply $\langle \mathrm{d}E/\mathrm{d}x \rangle$) with the expected specific energy loss (as a function of velocity β) for a certain particle type as this only depends on the particles charge and restmass [24, p.1]. An example of specific energy loss for different types of particles can be found in figure 3.6.

Bethe-Bloch function A particle traversing matter loses energy through hard and soft collisions with atoms and molecules. The Bethe-Bloch function describes this energy loss in dependency of the material it traverses (number density of electrons, mean excitation energy of its atoms) and of the momentum, mass and charge of the particle [26, p.29f.]. Considering for particles only elementary charge and plotting it in dependency of $\beta\gamma = \frac{p}{m}$ where γ is the Lorentz factor gives a shape like in figure 3.7. It exhibits a minimum at approximately $p = 3m_0$ where m_0 is the rest mass of the projectile particle.

After correcting for the so-called *density effect*, which is a screening effect of surrounding atoms as the particle traverses the material, the Bethe-Bloch formula (compare [26, 27]) has the form

$$\frac{\mathrm{d}E}{\mathrm{d}x}(\beta\gamma) = \frac{4\pi N e^4}{mc^4}\frac{1}{\beta^2} z^2 \left(\ln\left(\frac{2mc^2}{I}\right)\beta^2\gamma^2 - \beta^2 - \frac{\delta(\beta)}{2}\right) \tag{3.3.1}$$

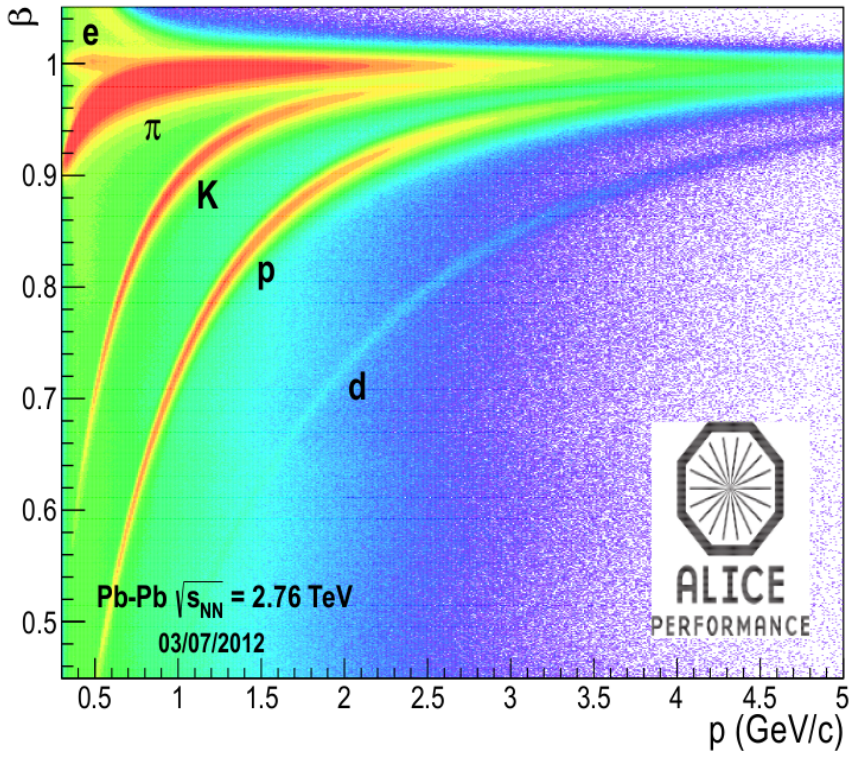

Figure 3.5: Velocity $\beta = L/t$ versus momentum plot. Bands for different types of particles are exhibited. Figure taken from [20].

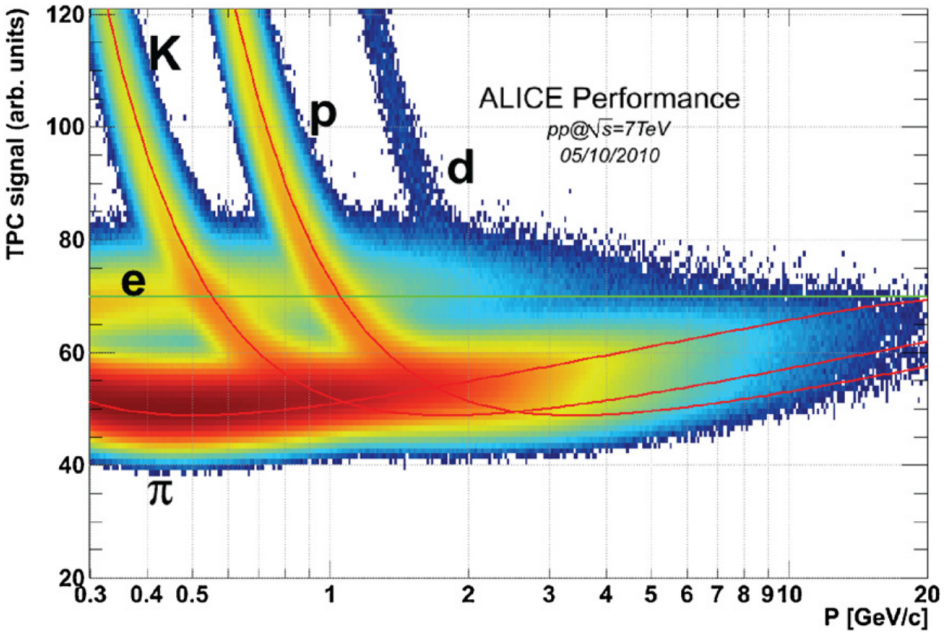

Figure 3.6: Specific energy plotted against momentum. In the high specific energy loss regions different branches are clearly visible. They are from left to right: K, p, d. The μ/π branch is not distinguishable in this plot. Figure taken from [25].

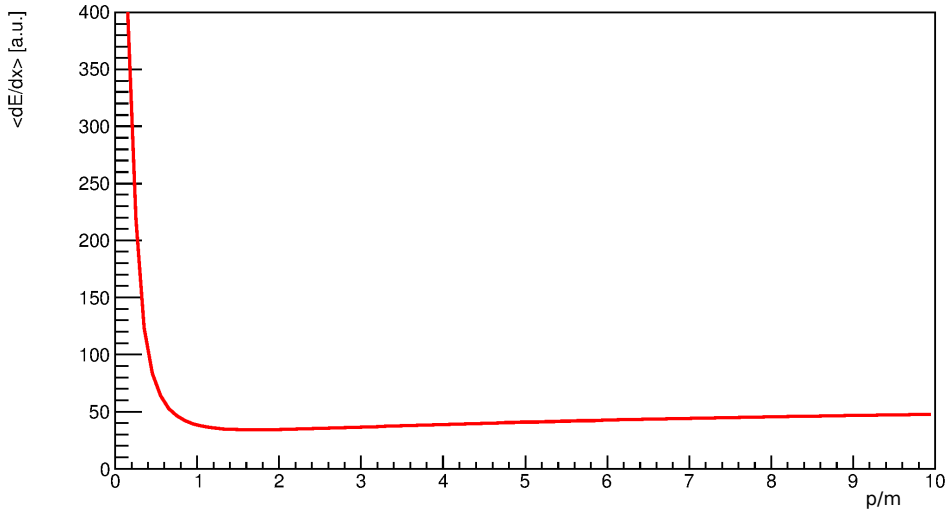

Figure 3.7: Shape of Bethe-Bloch function. It exhibits among other features the global minimum at about $p = 3m_0$ of the particle in question as well as the relativistic rise in higher p_T regions.

where $\delta(\beta)$ is the density effect correction, I the mean excitation energy of the material atom, mc^2 the rest energy of the electron, z the particles charge and N the number density of electrons.

One can unfortunately not simply use the Bethe-Bloch equation to describe the particle behaviour in our detectors. Although its actual energy loss (which would depend on the matter traversed) is described by it, we measure instead the *deposited* energy of a particle traversing the TPC. Furthermore we do this in the manner of a truncated mean as elaborated in Sect. 3.2.1. Additionally the density effect is not simply describable by a single parameter [26, p.336] and so different parametrizations exist and are in use to describe the $\langle \mathrm{d}E/\mathrm{d}x \rangle$ of a specific particle type. In this thesis use has been made of the form

$$\frac{\mathrm{d}E}{\mathrm{d}x}(\beta\gamma) = \frac{P_1}{\beta^{P_4}} \left\{ P_2 - \beta^{P_4} - \ln\left[P_3 + \left(\frac{1}{\beta\gamma} \right)^{P_5} \right] \right\} \tag{3.3.2}$$

that uses five free parameters (see [26, (10.5)]). It is sometimes called the *ALEPH parametrization*. For the underlying data, which form the basis of the fitting of the parametrization and therefore the determination of the parameters, the TOF detector has been used and a strict mass restriction of 0.1% accuracy to the expected mass of a kaon, pion and proton has been applied. The three particles have been independently plotted and additional cuts on the total track data has been added for the very low momentum region. Here it was important to have a similar density to the other regions in order not to „overfit“ the low momentum area: As a fit is obtained by minimizing the distances from data points to the function a high density area would naturally yield more distances (though they might be small) and a fitting here is therefore by the minimizer considered to be more crucial. Hence when the goal is to describe a certain shape (as it is the case for average energy loss) different densities might lead to a deviation of the shape as the higher density regions became „overfitted“. This is especially necessary when applying cuts without any further selection. The cuts consisted of multiple rectangles in which visual identification on the specific energy loss versus momentum plot was possible due to no overlapping branches (compare caption of figure 3.6).

Identification In the low p_T region it is sensible to identify particles on a track by track basis where the particle type is decided by shortest distance to the expected value of the Bethe-Bloch function for specific particle types [24, p.3]. For this analysis therefore only pions, kaons and protons need to be defined as a response function and it is possible to determine for every track

the closest distance to either the pion, kaon or proton track. As extensively treated in 3.2.1 the cluster response is best described by a Landau distribution and the mean is determined by truncating the Landau tail (compare [24, 28]). It is then possible to determine the standard deviation σ. An example fit for pions (green) and kaons (blue) is found in figure 3.8. Here, apart from the fit, the truncation is visible as well as other gaussian peaks from different particles (around 25 $\langle \mathrm{d}E/\mathrm{d}x \rangle$ distance from the pion peak). The standard deviation has been determined

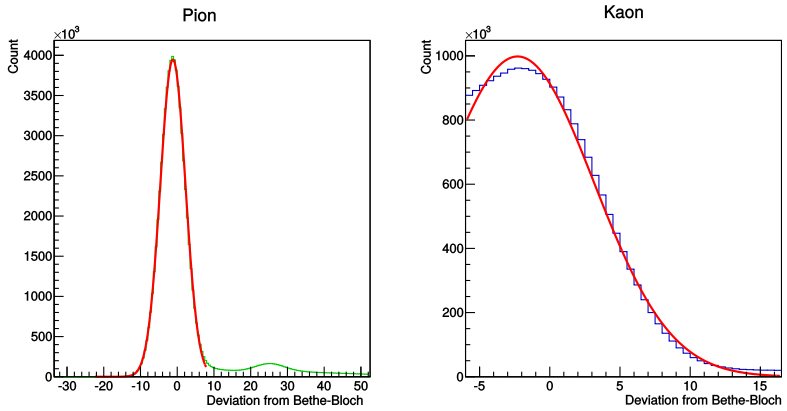

Figure 3.8: Gaussian fit of distance to calculated specific energy loss. The truncation in both cases is visible.

for two momentum ranges (0 GeV/c $\leq p \leq$ 0.4 GeV/c and 0.4 GeV/c $\leq p \leq$ 1 GeV/c) and shows clearly the tendency mentioned in [29] of worsening resolution for low $\langle\, \mathrm{d}E/\,\mathrm{d}x \rangle$ tracks. This is as well obvious from figure 3.8.

For the particle identification in this thesis with the TPC and ITS detector, the measured specific energy loss is only allowed to deviate 3σ from the expected value which is calculated with the previously mentioned fitted ALEPH parametrization of the Bethe-Bloch function. For an optimal fit this would include 99.7 % of all particles of the desired particle type. As the TPC and ITS detector are here only used for $p < 1$ GeV/c an overlap of the parametrization for different masses is minimal. In order to account for the nevertheless existing overlap, as an additional requirement for being identified as a particle, the track was required not to be within a 3σ range of any other particles calculated specific energy loss value.

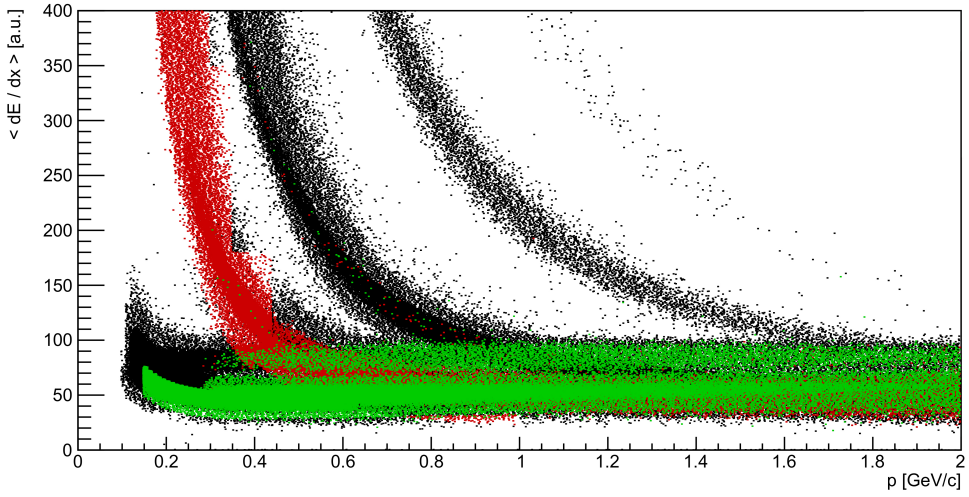

Figure 3.9: Specific energy loss plotted versus momentum. Kaons are marked in red, pions in green. Non-identified particles are black.

An example of identified particles with the ITS/TPC and TOF detector can be found in figure 3.9. The figure shows particles that are identified as kaons in red, pions in green and particles that are not identified as any of those two in black. In the figure one can see various electrons that are misidentified as pions or kaons. As the distance from the Bethe-Bloch function is larger than the applied 3σ cuts one can conclude that they have been within the 0.1 % precision of the TOF mass determination. The amount of particles misidentified are nevertheless small in comparison to the identified particle numbers. The figure shows the result of just 12 000 000 analyzed events which contained almost 93 million tracks. About 10 million tracks have been identified as kaons and 27 million tracks as pions. Overall this method is still a large improvement concerning identification in low momenta in comparison with exclusively identifying particles with the TOF detector but surely could be further improved.

CHAPTER 4

Analysis Methods

4.1 Analyzed Data and Track Selection

The data used for this analysis was produced by the ALICE experiment and originates from Period LHC10c and was the third reconstruction which includes almost 41 million 7 TeV events from proton-proton collisions. A transformation of the data has been conducted by the particle physics division at Lund University which consisted of a reduction of properties for each track and/or event in order to decrease the required storage space. The selection of tracks was performed on-the-fly therefore no additional transformation and hence output of the data was required.

As described in 3.2.1 clusters play an important role in tracking a particle with the TPC detector. Cluster-specific information is available within the data and can be used in order to avoid fake tracks by looking at the ratio of clusters that can be geometrically traversed (n_{cl}) and clusters that actually have been traversed (n_{eff}). See for detailed definitions [18, Sect. 2.4].

For this analysis a ratio of at least 0.83 of n_{eff} and n_{cl} has been required in order to reject fake tracks. This was as well suggested in [30]. Furthermore cuts for pseudorapidity of $|\eta| < 0.8$ as well as for a specific energy loss per unit length of at least 20 % of a minimal ionizing particle have been applied in order to be well within TPC acceptance ranges and to avoid detector inefficiencies, respectively. Last but not least a transverse momentum of at least 150 MeV/c has been required for a track in order to reduce further the amount of fake or incompletely traced particles.

4.2 Event Mixing

For event mixing as described in 2.6, every track of an event is combined with a number of tracks from strictly different events. For this analysis a number of ten other events has been used for the mixing process which reduces statistical uncertainties and other analyses often use 5-10 events, for instance in [28, 31]. The events in the pair that is mixed should show a certain similarity as the method aims at reproducing the same physical conditions without correlated particles (in the definition of 2.5). For this reason the events needed to undergo a selection process.

The mentioned physical similarity needs to be ensured. In detail a different collision hardness would create different initial situations for different particles. The particles would likely vary too much in order to describe the same collision. Hardness is best described by the track multiplicity which will be selected upon for this analysis. Furthermore in order to account for detector inefficiency the z-position of collision needs to be close, as events with similar hardness but largely deviating z-vertex could produce tracks that reach different blind areas of the detector, hence show not a similar collision for the analysis. Compared are here therefore events in terms

of z-position of collision vertex and multiplicity. A centrality requirement is not necessary as the analyzed data only consists of proton-proton collisions. The tolerance margin for accepting an event-mixing pair is $|\Delta z_{\text{vtx}}| < 2\,\text{cm}|$ and $|\Delta\text{trackmult}| < 5$. An illustration of the distribution of z-vertex and track multiplicity is shown in figures 4.1 and 4.2. It becomes obvious that the track multiplicity is not a very strict selection rule in contrast to the z-vertex selection which is more rigorous.

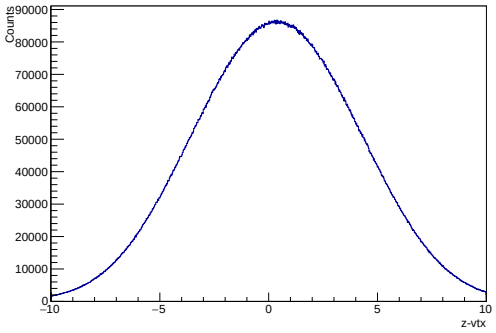

Figure 4.1: Distribution z-vertex position.

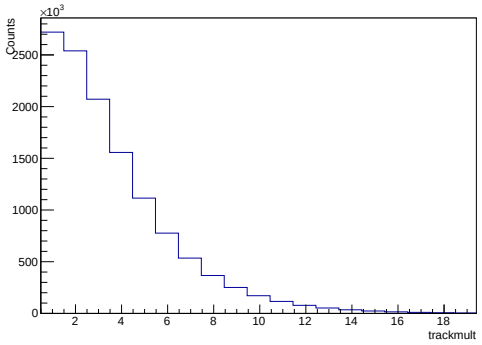

Figure 4.2: Distribution track multiplicity.

Due to the nature of event mixing the outcoming signal is about ten times larger than the unlike-sign signal that contains the invariant mass peak. A normalization is therefore required before subtracting the background. The background is estimated by f_{12}^{em} and therefore scaled by a factor λ such that

$$f_{12} - \lambda f_{12}^{\text{em}}$$

shall describe only the resonance signal. It is obvious that if no resonance signal exists λ will be equal to the number of events that are mixed (for instance 10). The normalization is conducted via integration over a specific invariant mass range for f_{12} and f_{12}^{em}. The scaling factor is then simply the ratio between the two integrals. The invariant mass range for K^{*0} was $1.4 - 1.8\,\text{GeV/c}$ and for ϕ $1.04 - 1.08\,\text{GeV/c}$ in order to be away from the mass peak in an area of approximately constant background.

4.3 Signal Fitting

Comparing to the conclusions of [11] yields the insight that the plotted distributions do not consist solely of pairs where both components are from a resonance decay (always referring to the *chosen* resonance) and background pairs where both particles are not from the chosen resonance decay. Although this would have been a wishful property we therefore can not completely subtract the resonance peak without leaving a certain residual background. Instead a description of the residual background should be found on top of which the Breit-Wigner function will be fitted.

In order to fit the Breit-Wigner function (2.4.1) to the invariant mass peak of the resonance the analysis is therefore required to account for this residual background. This is done here by approximating it with a third order polynomial. The third degree polynomial has been chosen because the residual background exhibits a more complex shape than a parabola. Instead we can observe most of the times two inclining or declining areas that are not connected and therefore two degree polynomials would be insufficient. The fitting has been performed with the `MINUIT` minimizer provided within the `ROOT` framework. It was given enough iterations to converge and tested for all p_T bins separately.

4.4 Weigthing of Events

The results (see Chapt. 5) include two treatments of event mixing: One uses simply the idea and method described in 2.6 and 4.2 and the other one accounts for different combinatorics (and hence probabilities) of achieving (or selecting) like-sign or unlike-sign pairs in both single event analysis as well as event mixing. For instance: When mixing two events that only contain each a positively charged pion the probability of finding a like-sign pion pair within a single event is zero but applying event mixing gives rise to a like-sign signal.

The weighting is conducted once by the ratio $n_{\mathrm{se}}/n_{\mathrm{em}}$ where n_{se} denotes the combinatorial possibilities of achieving a certain outcome and n_{em} the number of possibilities for the mixed event. In order to cross-check the same analysis has also been conducted with inversed weights where nominator and denominator are exchanged.

In detail the weighting has been conducted as follows. Let (A, B) denote a pair of events and A_+, A_- the number of positive, negative tracks in event A. The number of possibilities to achieve a certain signal (like-sign or unlike-sign, both components positive or negative) is then given by the following numbers:

$$
\begin{aligned}
N_{++} &= \frac{A_+(A_+ - 1) + B_+(B_+ - 1)}{2} \\
N_{--} &= \frac{A_-(A_- - 1) + B_-(B_- - 1)}{2} \\
N^{\mathrm{em}}_{++} &= A_+ B_+ \\
N^{\mathrm{em}}_{--} &= A_- B_- \\
N_{+-/-+} &= A_+ A_- + B_+ B_- \\
N_{++/--} &= N_{++} + N_{--} \\
N^{\mathrm{em}}_{+-/-+} &= N^{\mathrm{em}}_{+-} + N^{\mathrm{em}}_{-+} \\
N^{\mathrm{em}}_{++/--} &= N^{\mathrm{em}}_{++} + N^{\mathrm{em}}_{--}.
\end{aligned}
$$

4.5 Signal to Residual-Background Ratio

As described already in 4.3 a certain residual background is generally unavoidable. The Breit-Wigner function (2.4.1) describes the signal of the resonance decay and can not account for a residual background that can have nearly arbitrary shape. Hence (2.4.1) needs to be fitted on top of another function which in our case is a polynomial of order three as more than an ascending and descending signal needs to be described and a lower order polynomial could not describe that.

The event-mixing method requires as mentioned in 4.2 a normalization in order to describe the background. This nevertheless only scales its signal and does not change the shape. It is therefore possible to achieve even without scaling a good fit of the data with a comparably large absolute („absolute“, as it will be negative for a too large background description) residual background. It is therefore a good idea to look at the ratio of signal and background since a large combinatorial background will result in a small ratio even if the signal peak height on top of the background is the same height as for a non-existent residual background. Results comparing this quantity can be found in figures 5.5 and 5.11 for the ϕ and K^{*0} meson, respectively.

The procedure to determine the signal to residual-background ratio (or simplified signal to background ratio (SB ratio) where the reader should keep in mind, that the background referred to here is not the background below the resonance peak) follows [32] description of „bin counting“. Instead of taking though a Gaussian to fit the mass peak and approximate the mean and width (which is a rough estimate due to the longer tails of a resonance peak, since this follows the

Cauchy-distribution, see 2.4) we take the already fitted Breit-Wigner function (2.4.1) and its FWHM.

For each side of the determined peak of the Breit-Wigner function the background is determined as a connected $7F$ wide area, where F is the FWHM, which lays at least $6F$ away from the mass peak. The resonance signal area, which surely lays on a residual background as well, is determined by a $4F$ environment around the peak.

4.6 Relative Yield

For this thesis, due to a very limited amount of time, no Monte-Carlo simulation of the yield was conducted. As a data-driven substitute the yields are given relative to the one obtained by the uncorrected like-sign method. This shall give a clearer picture of whether a method increases or decreases the yield. The yields are calculated by integrating over the area of the resonance peak. As this thesis assumes a residual background described by a third order polynomial the integral of the fitted function of 4.2 is subtracted by the (in its fitting included) obtained polynomial.

CHAPTER 5

Results

In the following section the terms *low*, *intermediate* and *high* p_T refer to the left, middle and right sides of the figures x-axis for transverse momentum. The term „high p_T“ will here indicate a momentum value approximately between $3.6 - 10\,\text{GeV/c}$. „Low p_T“ shall in the following be around $0 - 1.6\,\text{GeV/c}$ and consequently „intermediate p_T“ is positioned between the two.

The figures in this section are cut at $7.7\,\text{GeV/c}$ in order to enable a more detailed view of the important regions but the shown error bars extend to $10\,\text{GeV/c}$ and are symmetric. The horizontal solid black lines denote the upper and lower error margin of the average as determined following the recipe from the Particle Data Group in [8].

In the following sections we compare the three analysis methods: like-sign estimation[1], event-mixing estimation[1] and corrected like-sign estimation[2] referring to five quantities. They are the calculated mass of the resonance[3], its width[3], the fitting performance of a Breit-Wigner function on top of a polynomial background of order three[4], the signal to residual-background ratio[5] and the relative yield of the methods[6]. All properties and methods are listed for the mesons ϕ and K^{*0}.

5.1 ϕ(1020) resonance

An example of the fit of all three analysis methods for the ϕ meson is given in figure 5.1. The bottom row shows the extracted signal after applying any of the three methods. The top middle plot shows the in Sect. 2.7 mentioned correction function. It is obvious from the top left and top middle plots that in this example only a very small correction is applied (around 1 %). The complete set of fits for the three methods and for all p_T bins can be found in appendix A.

Mass The mass of the resonance, extracted from the Breit-Wigner (2.4.1) parameter as described in 2.3, is plotted in figure 5.2 for different p_T bins. Due to large differences in available statistics for each bin the bin size is not linear as can be seen from the plot.

Overall a very good agreement with the determined average in [8] is visible. It is especially noteworthy that the fits are positioned for three bins within the given boundaries (which are rather small since the ϕ meson is a well determined resonance). A superior method among the three is not clearly visible as most of the error margins overlap. At low p_T (within $0 - 1.6\,\text{GeV/c}$) however, the method of uncorrected like-sign shows a larger distance to the average, especially in comparison to the event-mixing method.

[1] see Sect. 2.6 [2] see Sect. 2.7 [3] see Sect. 2.3 [4] see Sect. 4.2 [5] see Sect. 4.5 [6] see Sect. 4.6

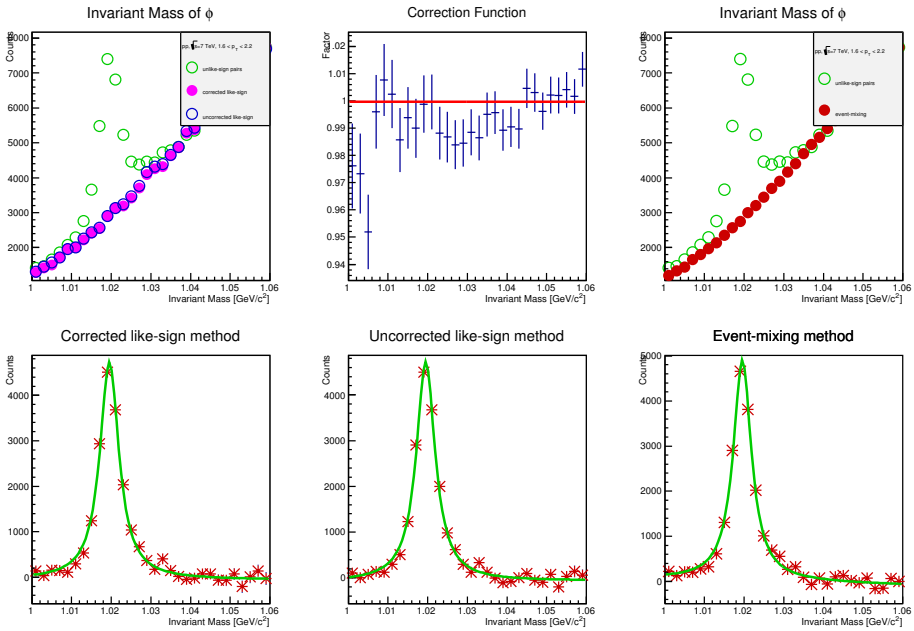

Figure 5.1: Example fit for $\phi(1020)$ with p_T between $1.6 - 2.2\,\mathrm{GeV/c}$. Shown are all three analysis methods.

Width Judging from the proximity of the data points to the expected average, figure 5.3 shows some deviation from the determined average which increases with increasing transverse momentum and is likely due to detector resolution effects (see Sect. 6.2.4). Overall the like-sign method does worse without correction function (still within error margins). From the error bars it is visible, that in most p_T bins the differences are marginal between the corrected and uncorrected like-sign method. The event-mixing method shows less deviations from the average at low and intermediate p_T and deviates stronger in the others although it should be stressed, that in all p_T bins error bars overlap and therefore a clear statement can not be made.

Fit The goodness of a fit can be determined via the χ^2/ndf quantity which is plotted for the three methods in figure 5.4. With the exception of the intermediate p_T range, the corrected like-sign method delivers the best fit results which is for $p_T > 3.4\,\mathrm{GeV/c}$ even below a ratio of one. The event-mixing method reaches throughout the scale worse results than the other methods. However the overall fitting seems to be excellent as no method exhibits a ratio larger than 1.65.

Signal to Residual-Background Ratio The signal to residual-background ratio informs about the signal strength that has been separated by a method in comparison to the residual background. It is achieved by the analysis described in 4.5 and the result for the ϕ meson can be found in figure 5.5.

It can be seen that the event-mixing method shows very mixed results. Although it achieves at high p_T a large ratio it ends up with negative ratios in the low and intermediate p_T range. This is certainly a high absolute value as well. Nevertheless this implies that either nominator or denominator of the ratio have become negative. Comparing the two like-sign methods reveals for the corrected one a clearly better performance. This is indicated by an increased ratio over the whole p_T range with an exception at the lowest p_T bin.

Relative Yield Since no Monte Carlo data was generated for this thesis the yield of the resonance was plotted for different p_T bins in figure 5.6 relative to the uncorrected like-sign method. A general rising trend of the event-mixing method is observable that reaches at high momenta approximately the same yield as the uncorrected-like sign (ratio one). The corrected

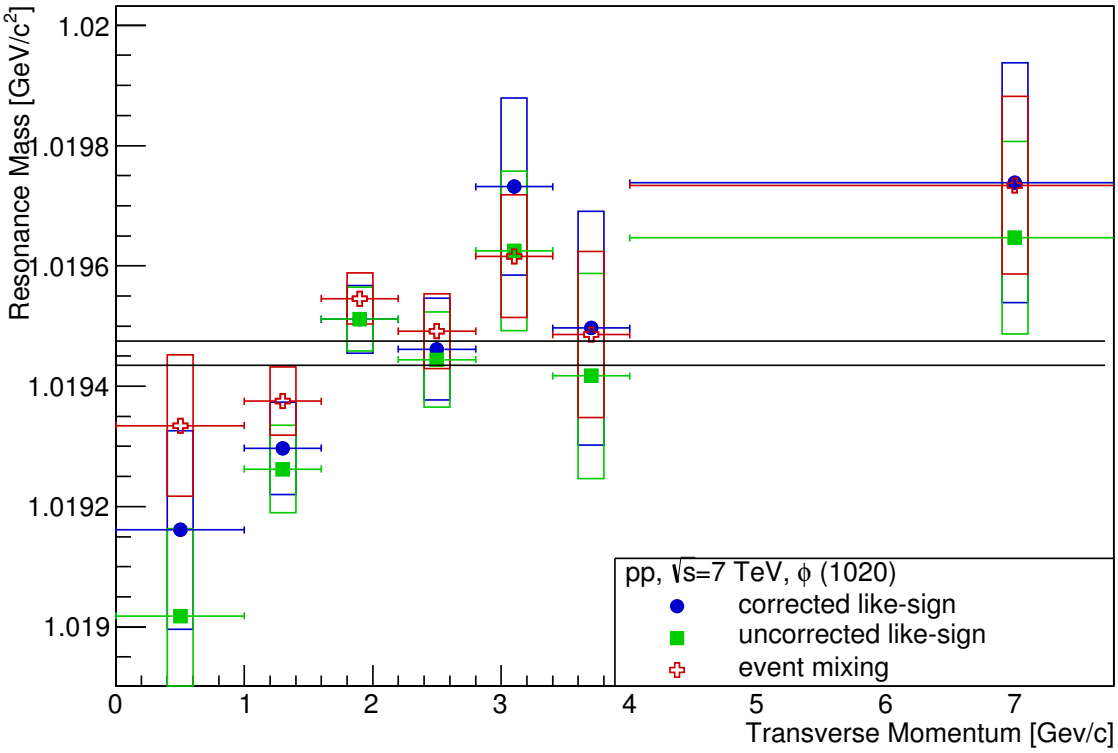

Figure 5.2: $\phi(1020)$ restmass for different p_T bins. Errors are only statistical.

like-sign method does not deviate that much but seems to fluctuate in approximately a 5 % margin.

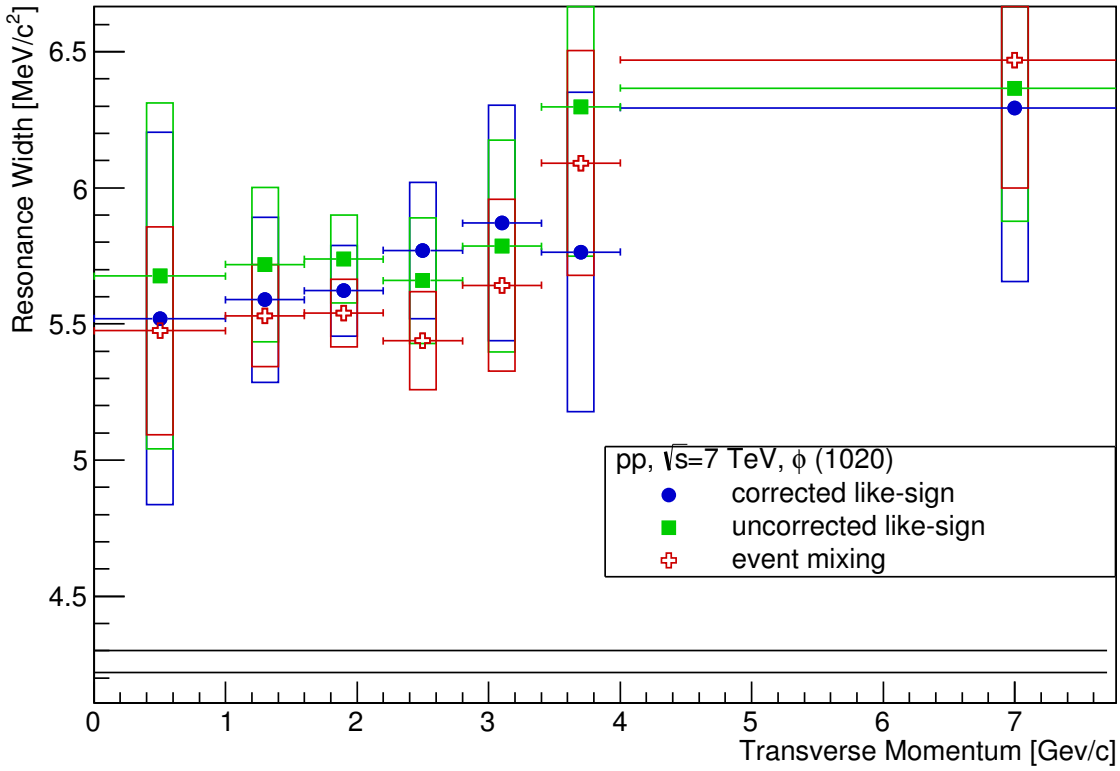

Figure 5.3: $\phi(1020)$ width of Breit-Wigner peak for different p_T bins. Errors are only statistical.

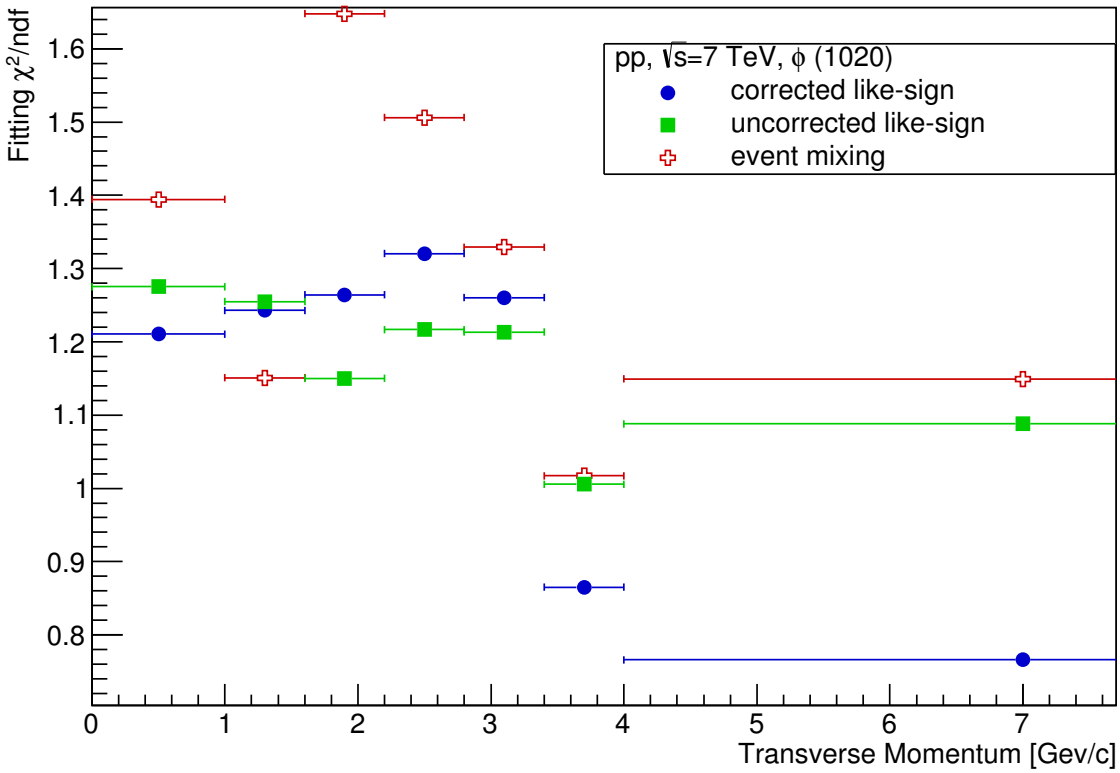

Figure 5.4: $\phi(1020)$ fitting quality of Breit-Wigner peak and additional polynomial background for different p_T bins. Lower implies a better fit. Errors only indicate the bin sizes.

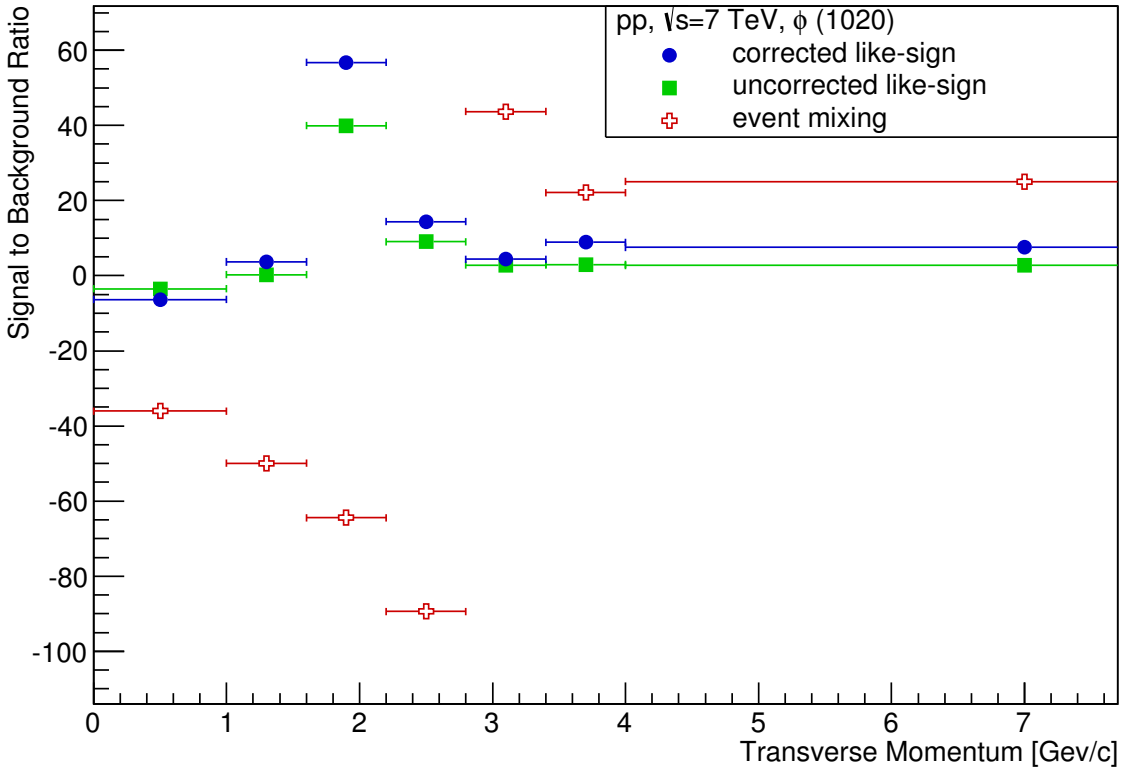

Figure 5.5: $\phi(1020)$ signal to residual-background ratio for different p_T bins. Higher implies a better signal extraction. Errors only indicate the bin sizes.

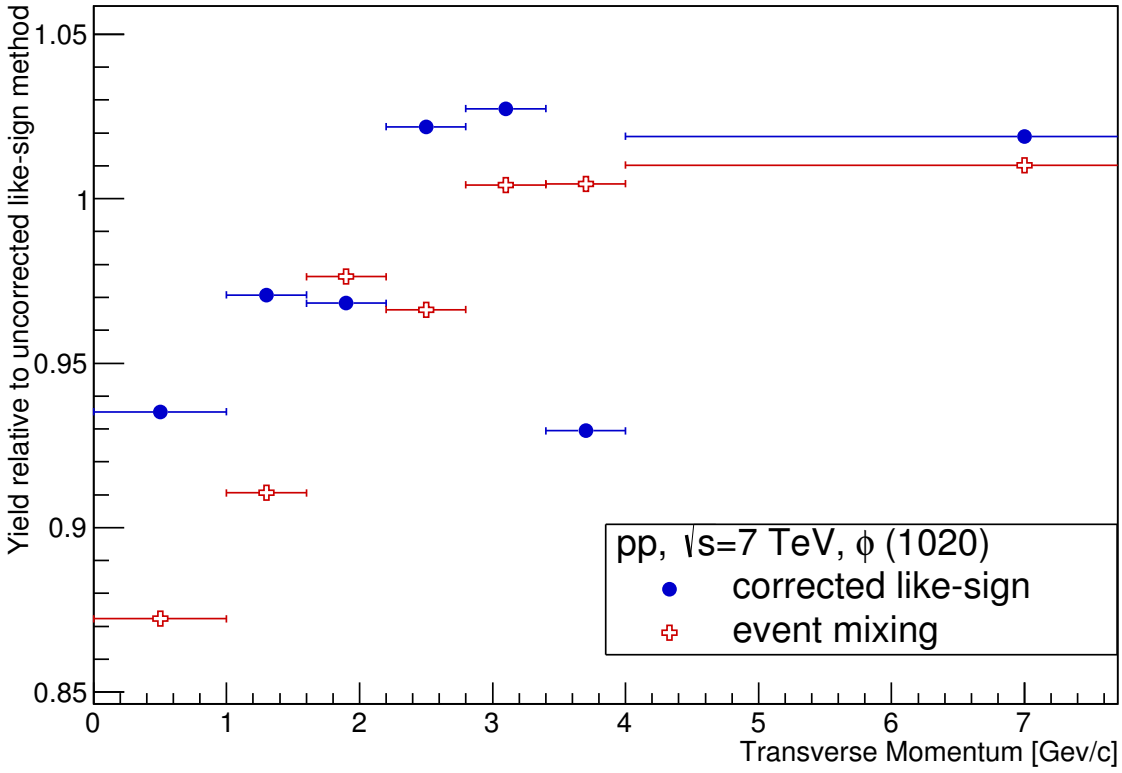

Figure 5.6: $\phi(1020)$ relative yield of corrected like-sign and event-mixing method to uncorrected like-sign. Errors only indicate the bin sizes.

5.2 $K^{*0}(892)$ resonance

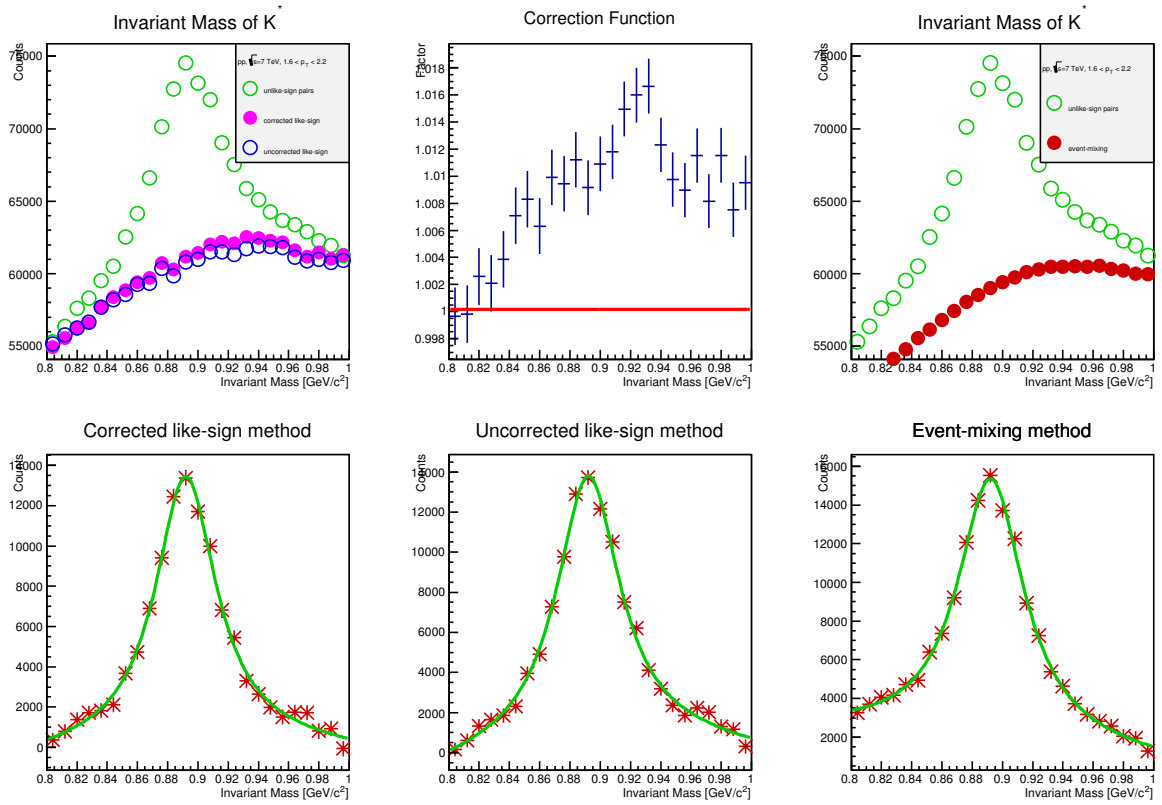

Figure 5.7: Example fit for $K^{*0}(892)$ with p_T between 1.6 – 2.2 GeV/c. Shown are all three analysis methods.

As in 5.1 we compare the three methods according to five quantities. An example for a fit of the three methods is given in figure 5.7. It is visible that the correction function corrects the like-sign signal upwards. Although it corrects it only by about 1 – 2 % a wide correction over most of the resonance peaks width is applied. This difference is clearly visible in the top left plot.

Mass The mass determination of the three methods for the K^{*0} meson is plotted for various p_T bins in figure 5.8. For hight p_T a good agreement with the average expected data can be concluded. At low and intermediate p_T though all methods underestimate the mass. In all of the p_T bins a distinguishing between the different methods is hardly possible as the statistical errors indicate an almost exact agreement between them. Only in the lowest bin a separation of the error bars happens.

Width Figure 5.9 shows the width of the Breit-Wigner function. At high and intermediate p_T a good agreement with the average mass is visible with the event-mixing method being better performing in some and worse in other bins. An overall tendency in movement of the data points as it was the case for the width of the ϕ meson is not visible.

Fit The ratio of χ^2 and degrees of freedom is plotted in figure 5.10. A generally good fit for all methods is visible as most data points lie under a ratio of 1.4. All three methods deviating in their fitting quality from bin to bin and no strictly better performing method can be singled out. This is an indication that for all three methods the fit within the fitting range is very good and differences are probable to originate in numerical and statistical uncertainties.

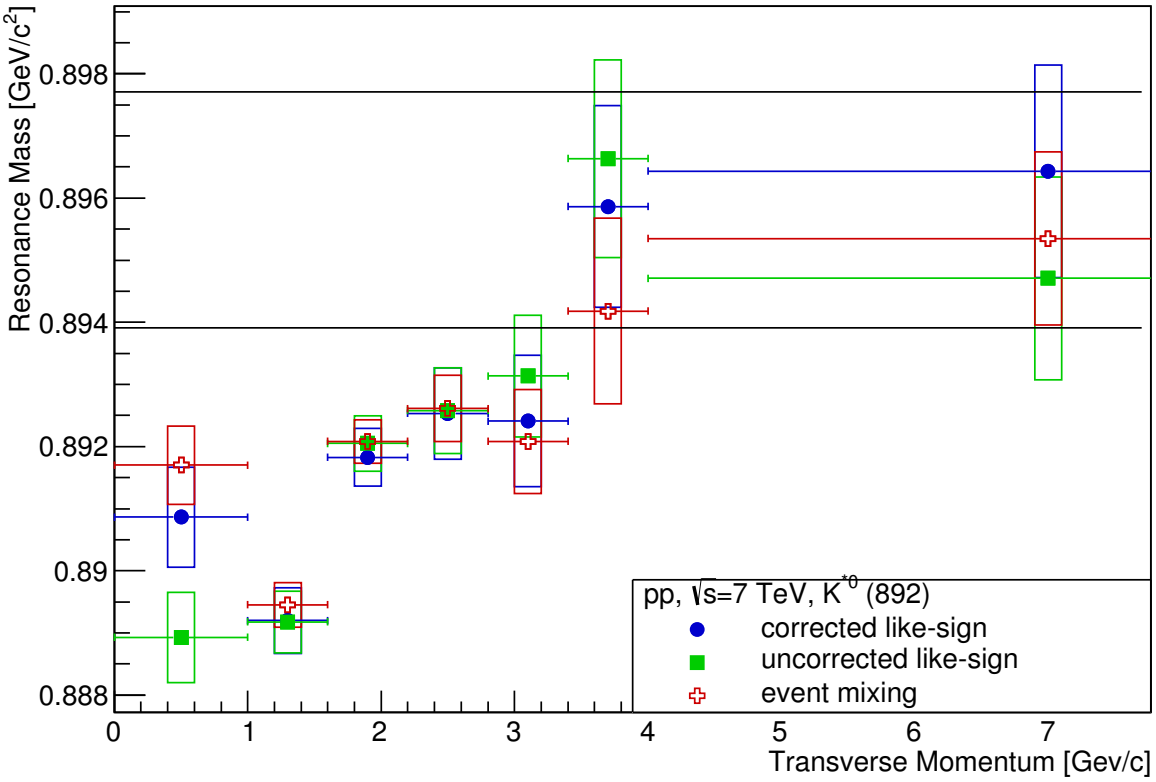

Figure 5.8: $K^{*0}(892)$ mass for different p_T bins. Errors are only statistical.

Signal to Residual-Background Ratio The strength of the signal in comparison to the residual background can be found in figure 5.11. First and foremost it is obvious that in the second p_T bin the event-mixing method yields a negative ratio which indicates a background approximation which lies over the unlike-sign invariant mass distribution itself. As we consider ratios this means that this overlying estimation only applies to the residual background or the signal peak itself as the minus signs otherwise would cancel each other.

Furthermore it is obvious that the corrected like-sign method extracts about the same amount of signal as the uncorrected one. At low p_T it does slightly better while being pretty much equal at high p_T.

Relative Yield The relative yield of the K^{*0} was plotted for different p_T bins in figure 5.6 relative to the uncorrected like-sign method. With one exception the yield of the event-mixing method is throughout the p_T range higher than the corrected as well as the uncorrected like-sign. The corrected like-sign method fluctuates (as already for the ϕ meson) in approximately a 5 % margin.

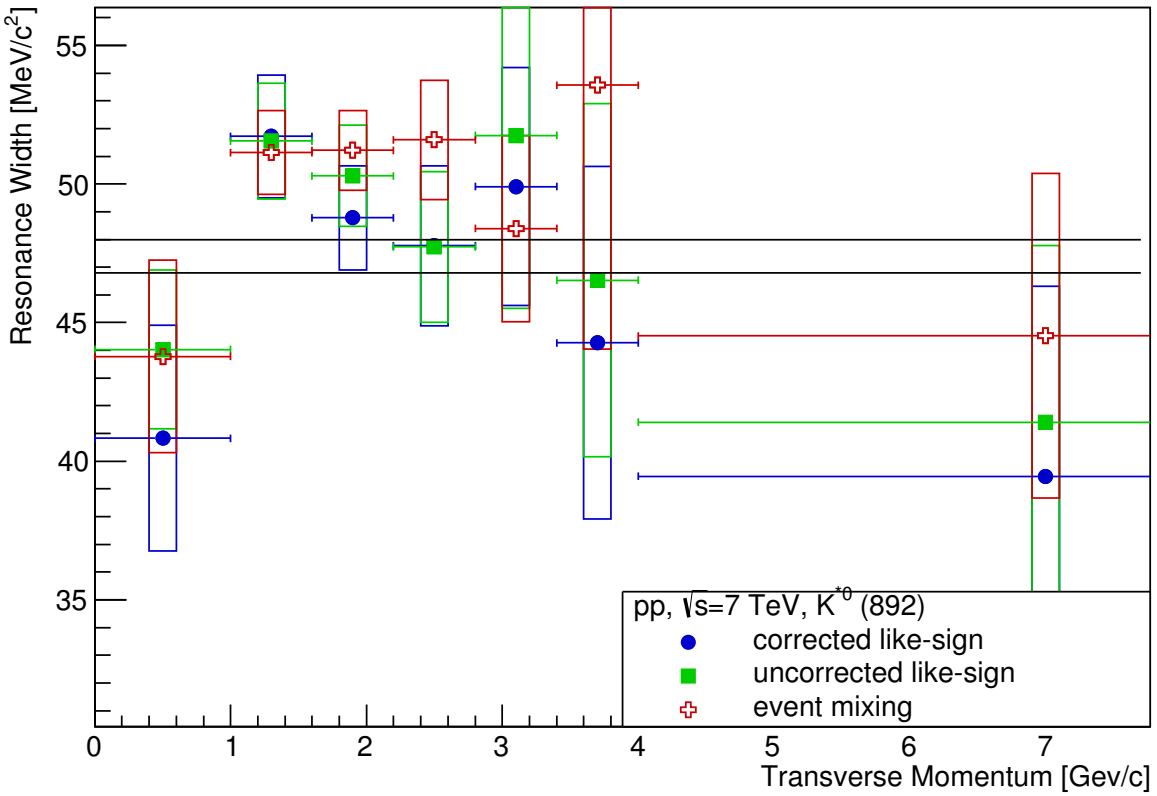

Figure 5.9: $K^{*0}(892)$ width for different p_T bins. Errors are only statistical.

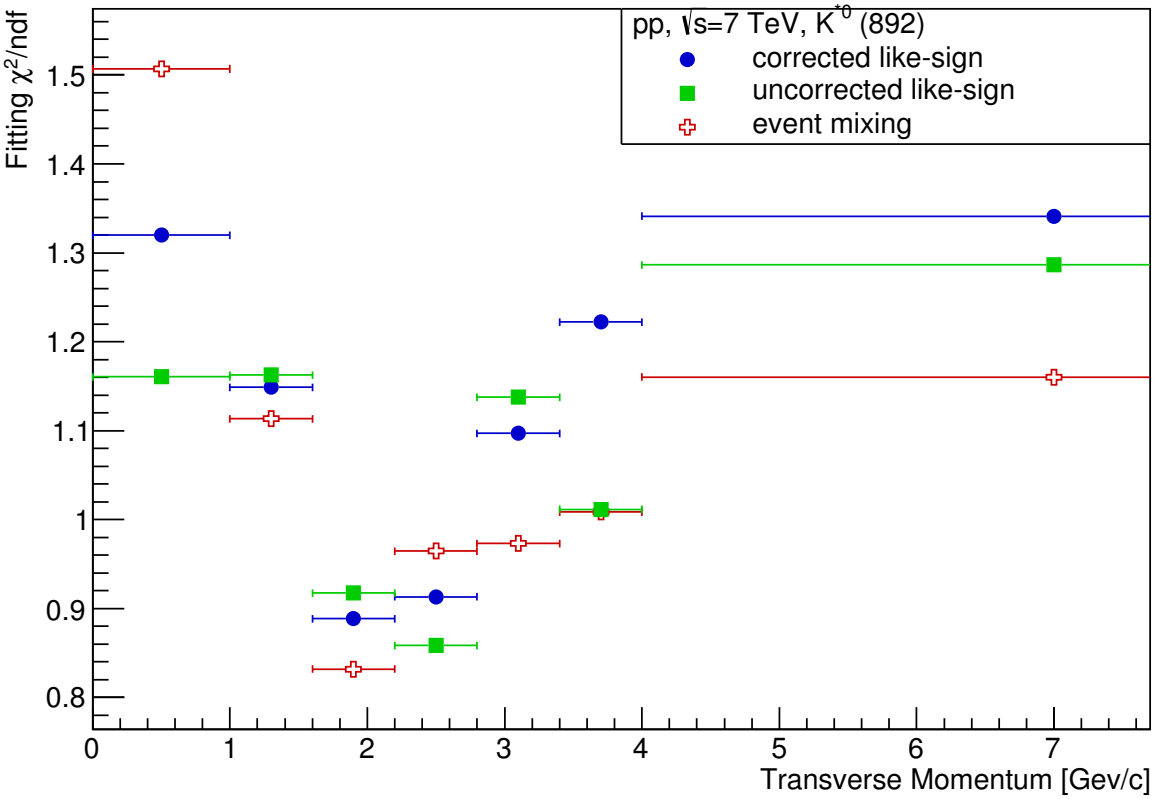

Figure 5.10: $K^{*0}(892)$ fitting quality of Breit-Wigner peak and additional polynomial background for different p_T bins. Lower implies a better fit. Errors only indicate the bin sizes.

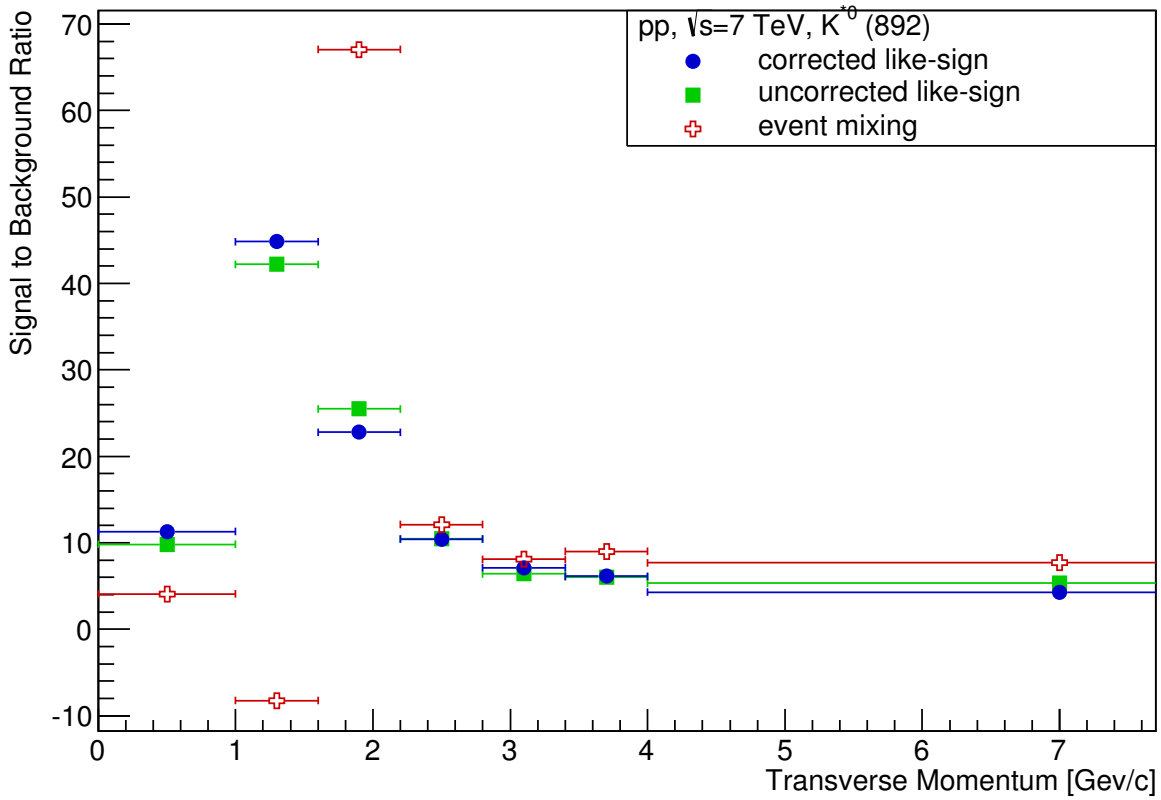

Figure 5.11: $K^{*0}(892)$ signal to residual-background ratio for different p_T bins. Higher implies a better fit. Errors only indicate the bin sizes. Observe: The event-mixing datum of p_T bin 1.0 – 1.6 GeV/c is plotted with a negative ratio.

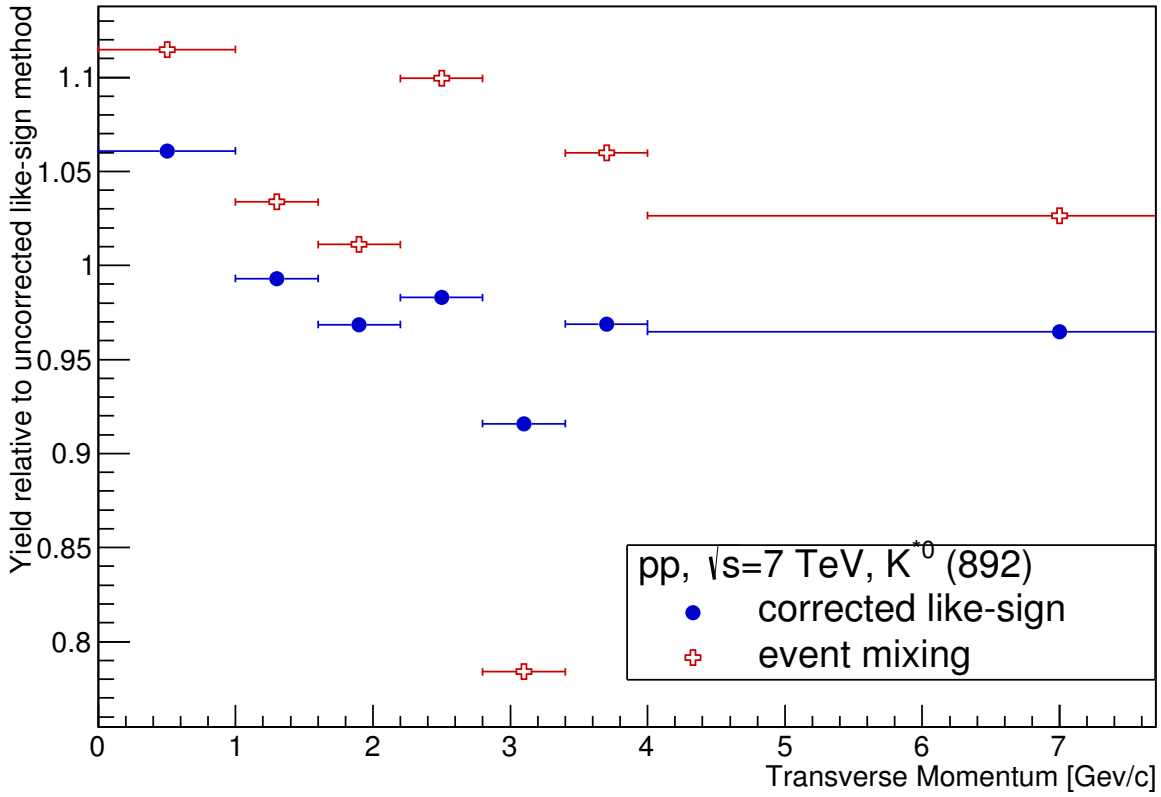

Figure 5.12: $K^{*0}(892)$ relative yield of corrected like-sign and event-mixing method to uncorrected like-sign. Errors only indicate the bin sizes.

5.3 The Correction Function

As introduced in 2.7 we used a correction function in order to correct the like-sign signal for acceptance differences caused by track bending for differently charged tracks. It is plotted in figure B.1 for the ϕ meson for different p_T bins and in figure B.2 for the K^{*0} in various p_T bins. Both figures can be found in the appendix due to their large scale. The vertical solid black line indicates the mass peak position as determined by [8] and the horizontal red solid line the average across the whole invariant mass distribution.

From the plots for the ϕ meson it is visible that in low momenta the correction applied is only minimal and around half a percent. A drastic increase of this correction, a downscaling, seems though to happen above a transverse momentum of 2 GeV/c. In the fourth p_T bin we already reach $8 - 9\,\%$ deviation from 1. While the transverse momentum increases, the amount of tracks becomes less and the error bars increase. Nevertheless at high p_T we observe around $10 - 11\,\%$ deviation.

The K^{*0} case is more difficult to describe. In low momenta we have again only a minimal correction effect of around half a percent. Directly at the expected mass peak no larger deviation of $1\,\%$ can be observed although large statistical errors make major fluctuations at high p_T possible. It is though striking from the plots that a peak exists in the correction function that is located in a slightly higher momentum area than the expected mass. Compare as well figure 5.7.

5.4 Binning Effect

In order to exclude the simple effect of binning as a source of the methods deviation, the same analysis run has been performed, with binning size changed by a factor of four. The plots produced are presented in appendix E and show almost the exact same results.

As fittings are sensitive to the effect of changing binning length this is a very reinforcing fact and indicates an authoritative analysis. Nevertheless for the rebinned results for the K^{*0} one can see that the lowest p_T bin due to its lower amount of tracks failed the fitting of the non-corrected like-sign method. Hence the results in this p_T bin deviate as can be easily seen in figure E.10. Other than that the previously described essences of the plots are nicely observable and contained within the Summary in Sect. 6.1.

5.5 Weighting Events

Upon applying the in Sect. 4.4 mentioned weights to the mixing of events the in appendix D gathered results are produced. Comparing it with the in this Chapter exhibited results barely a difference is recognizable. Although the corrected like-sign method (as it depends as well on the implementation of event-mixing) may have improved slightly in D.2 for the ϕ meson. Anyhow due to the error margins this cannot be securely stated and might very well be a result of statistical fluctuations. A similar picture can be drawn comparing our previous results with an application of inverted weights to the method of mixing events. No major deviation is observable. Although in figure D.8 for the highest p_T bin an improvement is visible this is not the case for the other p_T bins. At the same time the relative yield in the highest p_T bin increased substantially.

For the K^{*0} meson with inverted weights can a change be observed in the second p_T bin of figure D.19 where the signal to residual-background ratio became very large. Anyhow such a change is in general not observable for other p_T bins or comparative quantities. This applies for weighted and inversely weighted event-mixing methods.

5.6 Inverse Correction

As the in 2.7 described fraction of unlike-sign pair numbers and like-sign pair numbers is set rather arbitrarily one might pose the question if the effect of the correction function is dependent on the role of nominator and denominator. As a ratio less than one has the effect of downscaling the signal inverting this ratio should have the opposite effect.

In order to test this, a new analysis run with an inverted correction function has been conducted. Attachment C contains the figures which compare the performance of the inverse correction of the like-sign signal with the normal corrected like-sign method and for reference the uncorrected one and event-mixing method.

From the plots we can see that for the ϕ meson throughout all p_T bins the inverse correction does perform worse than the normal correction. This is especially observable in figure C.4 and figure C.3 at high p_T. Although it seems to correct nicely the highest p_T bin in figure C.1 the aforementioned facts indicate that this is a rather coincidental hit which does not indicate an increase in background description.

For the K^{*0} an improvement can be seen for high transverse momenta for the inversely applied correction in figure C.6. But especially the intermediate p_T region in figure C.7 and the low signal to residual-background ratio at high p_T in figure C.8 do not allow a conclusion of improvement.

CHAPTER 6

Discussion and Conclusion

In this section first a summary will be given of the results in Sect. 5. Hereafter a problem oriented discussion 6.2 treats possible reasons and mentions errors that might be found in the analysis method, followed by conclusions 6.3 that can be drawn from this thesis.

6.1 Summary

Following Sect. 5.1 and 5.2 we can summarize the three methods: event-mixing as well as like-sign with and without correction for the five researched quantities as follows.

Mass A good agreement with the averaged data from [8] can be observed for the K^{*0} meson: for high p_T all methods are, considering of course error margins, within the given boundaries. The fit for the ϕ meson does not look as good, which is partly due to the fact that the boundaries are very narrow around the given average, but still exhibits a very close proximity, as one can see from comparing the distances on the plot y-axis. A general „superior“ method can not be observed although it is interesting to remark that the event-mixing method does achieve for both mesons better proximity. Note though that a certain overlap with the error margins of the other two methods exist.

Width The width of the fitted mass distribution peak exhibits more differences for the two mesons. While for the ϕ a trend of increasing distance to the average with increasing transverse momentum is visible this phenomenon is not shown in the K^{*0} plot. Statistical errors cover for both mesons most of the deviations between the methods.

Fit The fitting quality shows a partly different picture. Comparing again the corrected and uncorrected like-sign method shows that in almost all bins for the two mesons the corrected method shows a lower value which translates to a better fit. Looking specifically at the event-mixing method shows a clear difference between the two mesons as it does considerably worse for the ϕ meson, reaching here almost in every bin the highest ratio. This does not show for the K^{*0} though. It needs to be kept in mind here that the quality of the fit does only describe the actual fitting area which is described in 4.2. Furthermore it should be mentioned that the statistical information available is about ten times higher which can amount as well to an expectation of a worse fitting as the error bars are smaller. Considering this, the aforementioned difference for the two mesons is though of special interest.

Signal to Residual-Background Ratio For the K^{*0} we see no real difference between the corrected and uncorrected like-sign method, only in the low p_T bins where the corrected like-sign method achieves a slightly better result. For the ϕ meson we observe again a clearly better performance of the corrected method in some p_T bins. For both mesons the event-mixing method achieves better results at high p_T and exhibits for low and intermediate p_T (especially for the K^{*0} meson) negative values which indicate a negative sign for either nominator or denominator. This will be specifically treated in 6.2.1.

Relative Yield The yield has been plotted relative to the yield of the uncorrected like-sign method and shows for the event-mixing a tendency towards 1 for high p_T and therefore implies the same yield as the uncorrected like-sign method describes. It starts though for the K^{*0} with a higher yield at low p_T and for the ϕ with a lower one. The corrected like-sign method deviates around the yield value of the uncorrected method by about 5 % throughout the transverse momentum range.

Weighting of event-mixing It can be concluded that the applied weights do not show a general improvement. Although in some p_T bins a gain can be achieved this is not a general trend. A worsening of the parameters i.e. growing distance from the expected value occurs just as well. Reversing the weights shows similar results which implies that the chosen weights in general should not be used as no advantage is gained.

6.2 Discussion

6.2.1 Event Mixing

Focusing first on the performance of the event-mixing method the analysis conducted shows that it does not sufficiently describe the background of the invariant mass distribution of a resonance decay. Already figure 5.7 exhibits for a single p_T bin a clear deviation from the other two methods. The extracted parameters from the Breit-Wigner function do not show this deviation as the statistical error overshadows it. Nevertheless especially when looking at figure 5.4 and 5.5 it becomes clear that the data is fitted worse than the other two methods and that a certain anomaly appears in describing the residual background.

It needs to be kept in mind that χ^2/ndf only describes the fitting quality in the fitting range which is given in Sect. 4.2 and which is probably the reason for the fit-goodness performance of the event-mixing method for the K^{*0} in figure 5.10. Already in this range, though, the event-mixing method performs less well for the ϕ meson. Considering a larger scale as plotted in figure 6.1 clearly shows the difference: away from the mass peak the two like-sign methods show an approximately constant residual background while the event-mixing method fails completely to describe the background in higher transverse momentum regions.

Here it is essential to note, that the normalization region plays an important role in actually extracting the parameters from the Breit-Wigner function. Scaling the background for instance can lead to an enlargement of the tails and hence to a widening of the peak - which leads via (2.4.2) to a shortening of the determined lifetime. The shape of the estimated background though does not change by scaling it. Therefore the bad description of the residual background away from the mass peak is unrelated to a choice of normalization background but is intrinsic to the event-mixing. Another example of this bad description can be found as well at [33, Figure 5] where the normalization has been performed via scaling inversely by approximately the event-mixing factor.

In order to discuss the phenomenon of a badly performing event-mixing method more thoroughly first one needs to recall the definition of *correlation* again (see Sect. 2.5). The peak

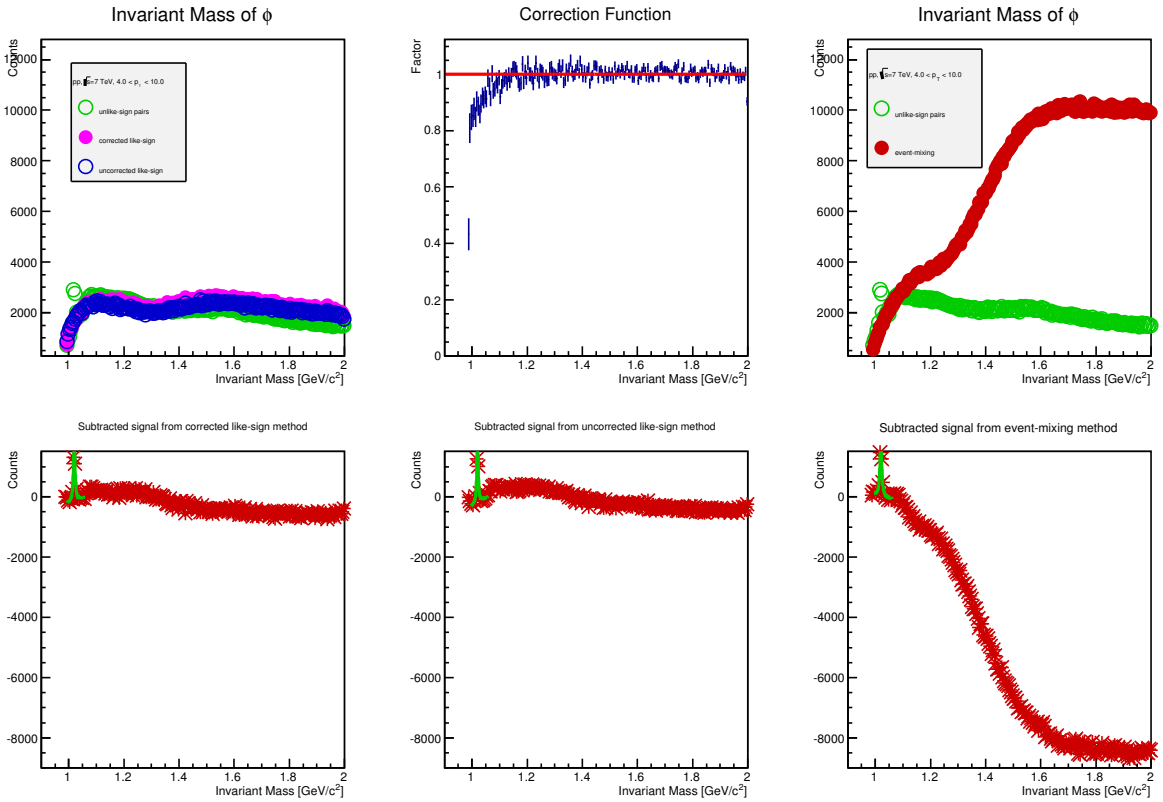

Figure 6.1: Example fit for $\phi(1020)$ with p_T between $4-10\,\mathrm{GeV/c}$. Shown are all three analysis.

in the unlike-sign invariant mass distribution originates from the amount of correlated particle tracks. As described in Sect. 2.3 the invariant mass of a pair is dependent on the momenta of the two particles and hence their spatial positioning. Due to the anisotropic nature of the, in the pp-collision created, particles and hence the existence of a „preferred direction“ in the event (it will be called here *jet-axis*) a bias of the azimuthal angle within an event may be observed among the tracks. Decay products from a resonance decay exhibit a similar spatial positioning of their momentum vectors as they are correlated due to energy-momentum conservation.

When now applying event mixing and accounting for the in 4.2 mentioned hardness and acceptance differences the events still differ by their jet-axis. Mixing therefore the tracks from different events calculates the invariant mass of pairs where the partners are in fact uncorrelated (in the sense of our definition in Sect. 2.5) but the jet-axis of their corresponding events is still present. Mixing with enough events therefore randomizes the jet-axis of the track pair (more precisely the azimuthal direction of their combined four-vector). Figure 6.2 shows the unlike-sign pair invariant mass distribution of K^+K^- (left), the same distribution with randomized azimuthal angle of one track (middle) and the unlike-sign pair invariant mass distribution from event-mixing (right).

The remarkable similarity in shape between the randomized azimuthal angle distribution and the event-mixing distribution indicates the large impact that the varying jet-axes of the mixed events have on the distribution outcome.

6.2.2 Correction Function

Comparing our analysis of the correction function 5.3 to the observations we could make comparing the methods (summary in section 6.1) we see first and foremost two things. The K^{*0} correction exhibits a peak at a slightly higher mass than the mean of the K^{*0} resonance. This implies a signal change that affects especially the width of the peak (larger or shorter tails) and consequently the fitting quality of the Bethe-Bloch function as the distribution that it describes is

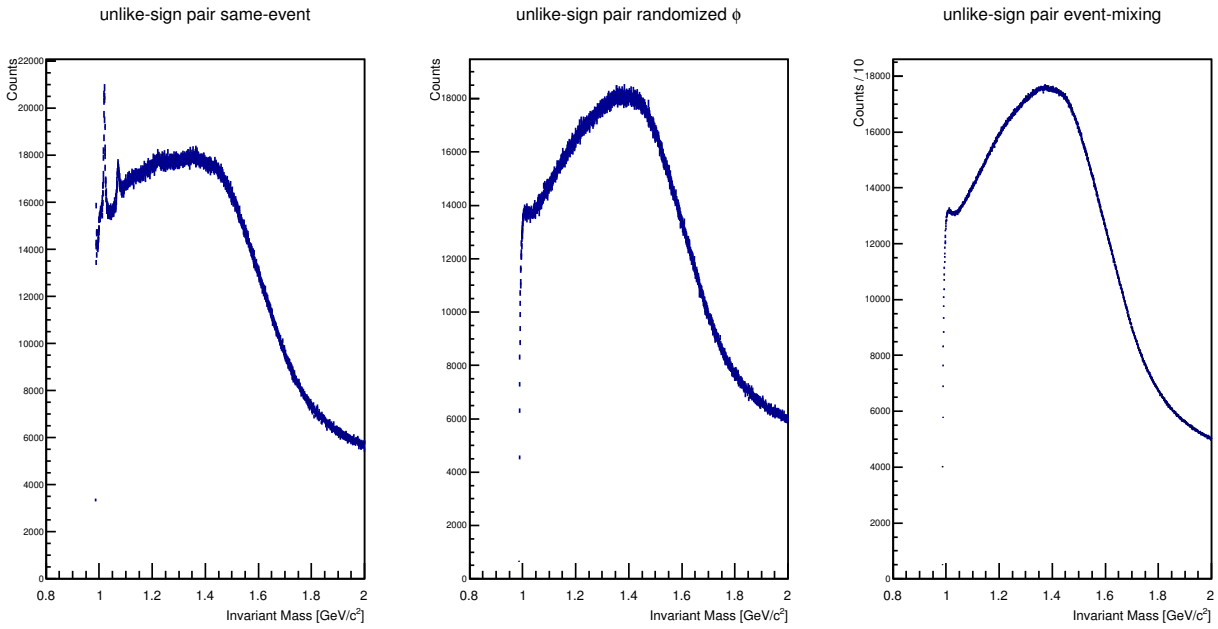

Figure 6.2: K^+K^- invariant mass distribution with randomized azimuthal angle (middle). As comparison the unlike-sign distribution without randomization is given (left) and the event-mixing unlike-sign distribution (right).

a Cauchy-distribution (see 2.4) and a change of distribution changes its fitting to it.

Furthermore the summary given contains a rich description of a ,,better performance“ of the corrected like-sign method for instance for the fitting and signal to residual-background ratio for the ϕ meson. As is visible from figure B.1 the correction applied at high p_T is fundamentally more significant than at low p_T. Especially in this range the corrected method performs better which strengthens the idea of a successful correction. In particular figure 5.4 shows at $p_T \geq 3.4\,\mathrm{GeV/c}$ a fitting goodness of under 1 which indicates an overfitting and hence implies that the residual background does not need to be described by a polynomial of order three. As this is true only for the corrected like-sign method this poses another indication of a well described background.

It seems that at the same time no large effect is caused on the extraction of parameters from the Breit-Wigner function by applying the correction function to the like-sign signal. Most of the deviations are within error margins and can therefore be considered to be statistical fluctuations. Only in the goodness of fit and signal to residual-background ratio there seems to exist a benefit that improves the two criteria successfully in comparison to the uncorrected like-sign signal.

If one looks closer at the fitting quality of the event-mixing method for the ϕ and the K^{*0} meson one can observe in the latter a better performance. It seems as well, that the width determination is handled better by the event-mixing for the K^{*0} than for the ϕ. A good explanation for the latter is found in the next Sect. 6.2.4. Furthermore one can argue that the ϕ possesses hidden strangeness (quark constituents $s\bar{s}$) while the K^{*0} has open strangeness ($\bar{s}$). As strangeness is conserved within the strong interaction this leads to the production of a particle with $S = -1$, a relation between the two is therefore existent. Since the like-sign method can not account for this relation the event-mixing method might describe it to a better extent which would need to undergo further investigation.

6.2.3 Correction Function Event-Mixing Dependency

As can be seen in (2.7.1) the correction function as applied for this thesis is the mere ratio of unlike- and like-sign pairs that are paired together across multiple events. As a statistical significant amount of data is processed which are uncorrelated in respect to their charge, i.e. charge conservation does not have to hold it would have been expected for a perfect system that

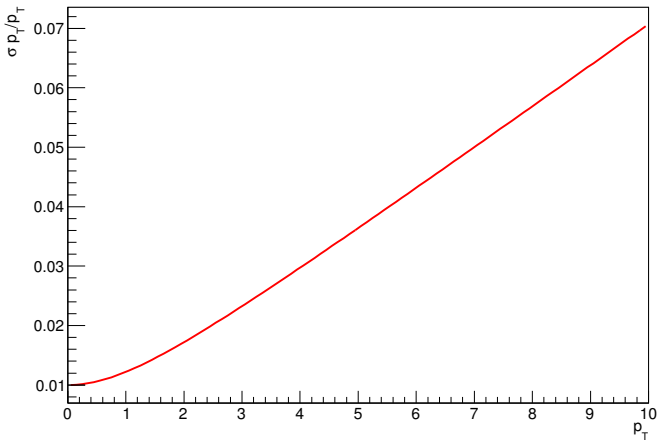

Figure 6.3: Resolution of transverse momentum measurement for the TPC.

the correction function is the constant 1-function and therefore would not apply any correction. Surprisingly this is not the case as could have already been seen i.e. in figure 2.3.

A possible explanation for this was that acceptance differences for differently charged and therefore bent tracks within the detector system are causing these systematic deviations from 1. As described in 4.2 the pair components from event-mixing are selected for z-vertex in order to minimize acceptance issues. Hence when not selecting for z-vertex a deviation in correction function is to be expected. Comparing figure B.1 with figure B.3 as well as figure B.2 with figure B.4 shows clearly that no real difference can be observed. As the selection of event pairs is a very computational expensive action this raises support for the corrected like-sign method as it can yield better background description than the event-mixing method while using a faster calculation method.

6.2.4 ϕ Peak Width Deviation

For the extracted width parameter of the ϕ meson (plotted in figure 5.3) a general trend throughout all three methods can be observed: The deviation from the determined average increases with increasing transverse momentum. Comparing this trend to figure 7.1 in [34] as well as to [35] indicates that a correlation with the transverse momenta resolution as measured by the TPC is likely. Following the latter reference the resolution is given by

$$\left(\frac{\sigma p_T}{p_T}\right)^2 = (0.01)^2 + (0.007 \cdot p_T)^2$$

which is plotted in figure 6.3. The shape suggests that the deviations, that increase with p_T, are a result of transverse momentum uncertainties for high momenta which are measured with the TPC. Reviewing [36] one can observe an increase in uncertainty for $p_T < 1\,\text{GeV/c}$ which is very well in agreement with our observed error bars in above mentioned plot.

6.3 Conclusion

This thesis has presented a study of different invariant-based yield methods. The results indicate for about two of four comparative quantities (not including yield) a beneficial role of the correction function applied to the like-sign method. This especially seems to account for the background description as the fitting goodness and signal to residual-background ratio were improved. The parameters from the Breit-Wigner function though do not show mentionable

deviations. From the author's view these results come not totally by surprise as the correction function is using data generated by the event-mixing method which aims for describing the background.

> ,,The intuitive idea supporting this method [event-mixing] is that the distributions of pairs from mixed events contain everything of the reaction and the experimental device except the correlation of interest, while calculated background distributions using fit, interpolation, phase space, or Monte Carlo prescriptions may miss this information.“ [11]

While the event-mixing method uses all this information, in the applied correction function it is discarded while simply concentrating on the charge sign of the track pairs. At first sight this seems rather unreasonable and should show a clearly better performance for the event-mixing method. In fact the opposite was the case and the act of neglecting this information seems to be beneficial. The event-mixing method seems to assume an azimuthal angle symmetry for the events that are mixed which is not naturally given for invariant mass distribution analysis. The results indicate that this angular randomization of the event-plane leads to the bad results of the event-mixing method. Furthermore it is obvious that in the applied form the event-mixing did not describe the background properly. The analysis of the K^{*0} though suggests that event-mixing could account for other quantum number conservation laws as for instance strangeness or describe final state interaction for the K^{*0} better than the like-sign method. However this needs to be further analyzed.

6.4 Outlook

In order to extend the results presented here regarding the study of two mesons at 7 TeV center of mass energy further analysis can be conducted using proton-lead collisions instead of proton-proton ones. Additionally the role of event-mixing in azimuthal angle symmetric analyses needs to be further investigated. This can include as well the possibility of a manual azimuthal rotation on an event-by-event basis for non-symmetric analyses. The role of event-mixing concerning the description of quantum number conservation laws needs to be further examined as well and especially compared to the performance of like-sign methods without event-mixing.

An extended analysis with a larger amount of events would certainly be beneficial, as statistical errors make results at higher p_T harder to compare. Additional data collection in LHC Run 2 this year can surely increase the amount of events for analysis.

Index

Abbreviations and Acronyms

m_0	invariant mass
p_T	transverse momentum
ALICE	A large ion collision experiment
CERN	European Organization for Nuclear Research
dEdx	Shortform of $\langle \mathrm{d}E/\mathrm{d}x \rangle$, which denotes the average specific energy loss per unit length of a particle
FWHM	Full width half maximum
ITS	Inner Tracking System
LHC	Large Hadron Collider
MRPC	Multi-Gap Resistive Plate Chamber
MWPC	Multi-Wire Proportional Chamber
PID	Particle Identification
pp	Abbreviation for proton-proton collision
QCD	Quantum Chromodynamics
QED	Quantum Electrodynamics
QFT	Quantum Field Theory
SDD	Silicon Drift Detector
SPD	Silicon Pixel Detector
SSD	Silicon Strip Detector
TOF	Time-Of-Flight
TPC	Time Projection Chamber

References

[1] John Dalton. “On the Absorption of Gases”. In: *Memoirs of the Literary and Philosophical Society of Manchester* 1.2 (1805), pp. 271–286.

[2] Joseph John Thomson. “Cathode Rays”. In: *The Electrician* XXXIX (May 21, 1897), pp. 104–109.

[3] MissMJ. *Standard Model of Elementary Particles.svg - Wikipedia, the free encyclopedia*. URL: https://en.wikipedia.org/wiki/File:Standard_Model_of_Elementary_Particles.svg (visited on 12/09/2014).

[4] Michael Edward Peskin and Daniel V Schroeder. *An Introduction to Quantum Field Theory*. Reading, Massachusetts: Addison-Wesley, 1995. ISBN: 0-201-50397-2.

[5] Y. Aoki et al. “The QCD transition temperature: results with physical masses in the continuum limit”. In: *Physics Letters B* 643.1 (Nov. 2006), pp. 46–54. ISSN: 03702693. DOI: 10.1016/j.physletb.2006.10.021. arXiv: hep-lat/0609068. URL: http://arxiv.org/abs/hep-lat/0609068 (visited on 11/28/2014).

[6] C. Markert, G. Torrieri, and J. Rafelski. “Strange hadron resonances: Freeze-out probes in heavy-ion collisions”. In: *arXiv preprint hep-ph/0206260* (2002). URL: http://arxiv.org/abs/hep-ph/0206260 (visited on 11/28/2014).

[7] Helmut Satz. “The Quark-Gluon Plasma”. In: *Nuclear Physics A* 862-863 (July 2011), pp. 4–12. ISSN: 03759474. DOI: 10.1016/j.nuclphysa.2011.05.014. arXiv: 1101.3937. URL: http://arxiv.org/abs/1101.3937 (visited on 01/08/2015).

[8] J. Beringer et al. “Review of Particle Physics”. In: *Physical Review D* 86.1 (July 20, 2012), p. 010001. DOI: 10.1103/PhysRevD.86.010001. URL: http://link.aps.org/doi/10.1103/PhysRevD.86.010001 (visited on 11/26/2014).

[9] Vito Manzari and Giorgio Stefanini. *Pixels make for perfect particle tracking in ALICE - CERN Courier*. URL: http://cerncourier.com/cws/article/cern/34937 (visited on 11/25/2014).

[10] Brian Martin and Graham Shaw. *Particle physics*. 3rd ed. John Wiley & Sons, 2008. ISBN: 978-0-470-03294-7. (Visited on 05/23/2013).

[11] D. L’hote. “About resonance signal extraction from multiparticle data: combinatorics and event mixing methods”. In: *Nuclear Instruments and Methods in Physics Research Section A: Accelerators, Spectrometers, Detectors and Associated Equipment* 337.2 (1994), pp. 544–556. URL: http://www.sciencedirect.com/science/article/pii/0168900294911266 (visited on 07/31/2014).

[12] ALICE Collaboration. *37 countries, 151 institutes, 1550 members — ALICE Collaboration*. URL: http://aliceinfo.cern.ch/General/index.html (visited on 11/28/2014).

[13] Federico Ronchetti. “Topical talk: All you wanted to know about data taking operations and you were afraid to ask”. CERN Junior’s day November 2014, Nov. 28, 2014.

[14] CERN press office. *CERN's Large Hadron Collider gears up for run 2*. URL: http://press.web.cern.ch/press-releases/2014/12/cerns-large-hadron-collider-gears-run-2 (visited on 12/15/2014).

[15] ALICE Collaboration et al. "The ALICE experiment at the CERN LHC". In: *Journal of Instrumentation* 3.8 (Aug. 1, 2008), S08002. ISSN: 1748-0221. DOI: 10.1088/1748-0221/3/08/S08002. URL: http://iopscience.iop.org/1748-0221/3/08/S08002 (visited on 12/18/2014).

[16] J. Alme et al. "The ALICE TPC, a large 3-dimensional tracking device with fast readout for ultra-high multiplicity events". In: *Nuclear Instruments and Methods in Physics Research Section A: Accelerators, Spectrometers, Detectors and Associated Equipment* 622.1 (Oct. 2010), pp. 316–367. ISSN: 01689002. DOI: 10.1016/j.nima.2010.04.042. arXiv: 1001.1950. URL: http://arxiv.org/abs/1001.1950 (visited on 12/17/2014).

[17] ALICE Collaboration. "Production of pions, kaons and protons in pp collisions at sqrt(s)= 900 GeV with ALICE at the LHC". In: *The European Physical Journal C* 71.6 (June 2011). ISSN: 1434-6044, 1434-6052. DOI: 10.1140/epjc/s10052-011-1655-9. arXiv: 1101.4110. URL: http://arxiv.org/abs/1101.4110 (visited on 12/17/2014).

[18] Alexander Kalweit. "Production of light flavor hadrons and anti-nuclei at the LHC". In: (2012). URL: http://tuprints.ulb.tu-darmstadt.de/3063/ (visited on 12/09/2014).

[19] ALICE Collaboration. *The ALICE Time of Flight Detector*. URL: http://aliceinfo.cern.ch/Public/en/Chapter2/Chap2_TOF.html (visited on 12/02/2014).

[20] A. Alici. "Status and performance of the ALICE MRPC-based Time-Of-Flight detector". In: *Journal of Instrumentation* 7.10 (Oct. 1, 2012), P10024. ISSN: 1748-0221. DOI: 10.1088/1748-0221/7/10/P10024. URL: http://iopscience.iop.org/1748-0221/7/10/P10024 (visited on 01/07/2015).

[21] A. N. Akindinov et al. "Space charge limited avalanche growth in multigap resistive plate chambers". In: *The European Physical Journal C - Particles and Fields* 34.1 (July 1, 2004), s325–s331. ISSN: 1434-6044, 1434-6052. DOI: 10.1140/epjcd/s2004-04-031-9. URL: http://link.springer.com/article/10.1140/epjcd/s2004-04-031-9 (visited on 12/18/2014).

[22] The ALICE Collaboration. *ALICE Silicon Pixel Detector*. ALICEinfo. URL: http://aliceinfo.cern.ch/SPD/ (visited on 12/18/2014).

[23] ALICE Collaboration and Giacomo Contin. "The ALICE Silicon Strip Detector performance during the first LHC data taking". In: *arXiv:1101.2776 [hep-ex, physics:physics]* (Jan. 14, 2011). arXiv: 1101.2776. URL: http://arxiv.org/abs/1101.2776 (visited on 12/18/2014).

[24] Alexander Kalweit. "Particle Identification in the ALICE Experiment". In: *arXiv:1107.1514 [hep-ex, physics:nucl-ex]* (July 7, 2011). arXiv: 1107.1514. URL: http://arxiv.org/abs/1107.1514 (visited on 12/02/2014).

[25] M. C. S. Williams. "Particle identification using time of flight". In: *Journal of Physics G: Nuclear and Particle Physics* 39.12 (Dec. 1, 2012), p. 123001. ISSN: 0954-3899. DOI: 10.1088/0954-3899/39/12/123001. URL: http://iopscience.iop.org.ludwig.lub.lu.se/0954-3899/39/12/123001 (visited on 01/07/2015).

[26] W Blum, Werner Riegler, and L Rolandi. *Particle detection with drift chambers*. Berlin; New York: Springer, 2008. ISBN: 9783540766841 3540766847. URL: http://public.eblib.com/choice/publicfullrecord.aspx?p=416987 (visited on 09/30/2014).

[27] Enrico Fermi. “The Ionization Loss of Energy in Gases and in Condensed Materials”. In: *Physical Review* 57.6 (Mar. 15, 1940), pp. 485–493. DOI: 10.1103/PhysRev.57.485. URL: http://link.aps.org/doi/10.1103/PhysRev.57.485 (visited on 12/03/2014).

[28] Alice Collaboration et al. “ALICE: Physics Performance Report, Volume II”. In: *Journal of Physics G: Nuclear and Particle Physics* 32.10 (Sept. 1, 2006), pp. 1295–2040. ISSN: 0954-3899, 1361-6471. DOI: 10.1088/0954-3899/32/10/001. URL: http://stacks.iop.org/0954-3899/32/i=10/a=001?key=crossref.12b61c3fa85ced3d52f01ba18e5efe3e (visited on 10/30/2014).

[29] Peter Christiansen et al. “Particle identification at high-pT with TPC-dE/dx in the relativistic rise”. In: *ALICE Analysis Note* (Aug. 16, 2013).

[30] ALICE Collaboration. “Definitions of TPC related track properties”. In: *ALICE Internal Note* (Feb. 9, 2011).

[31] A. G. Knospe, Alice Collaboration, et al. “Hadronic resonance production in Pb—Pb collisions at the ALICE experiment”. In: *Journal of Physics: Conference Series*. Vol. 420. IOP Publishing, 2013, p. 012018. URL: http://iopscience.iop.org/1742-6596/420/1/012018 (visited on 11/28/2014).

[32] Antonin Maire and the ALICE Collaboration. “Multi-strange baryon measurements at LHC energies, with the ALICE experiment”. In: *Journal of Physics: Conference Series* 270 (Jan. 1, 2011), p. 012020. ISSN: 1742-6596. DOI: 10.1088/1742-6596/270/1/012020. URL: http://stacks.iop.org/1742-6596/270/i=1/a=012020?key=crossref.ec5110d0d9d7bf4e970fe3a97b2d255c (visited on 11/25/2014).

[33] INFN Trieste. *Results with Event Mixing Technique*. URL: http://webint.ts.infn.it/en/research/exp/alice/resonances/proton-proton-7-tev-data/results-with-event-mixing-technique.html (visited on 09/30/2014).

[34] ALICE Collaboration. *Technical Design Report for the Upgrade of the ALICE Time Projection Chamber*.

[35] ALICE Collaboration. “Transverse momentum spectra of charged particles in proton–proton collisions at 900 GeV with ALICE at the LHC”. In: *Physics Letters B* 693.2 (Sept. 2010), pp. 53–68. ISSN: 03702693. DOI: 10.1016/j.physletb.2010.08.026. URL: http://linkinghub.elsevier.com/retrieve/pii/S0370269310009731.

[36] Christian Lippmann. “Performance of the ALICE Time Projection Chamber”. TIPP 2011 - 2nd International Conference on Technology and Instrumentation in Particle Physics. Chicago, June 11, 2011. URL: https://indico.cern.ch/event/102998/session/16/contribution/290/material/slides/0.pdf (visited on 12/17/2014).

Appendices

APPENDIX A

Complete Fitting Plots

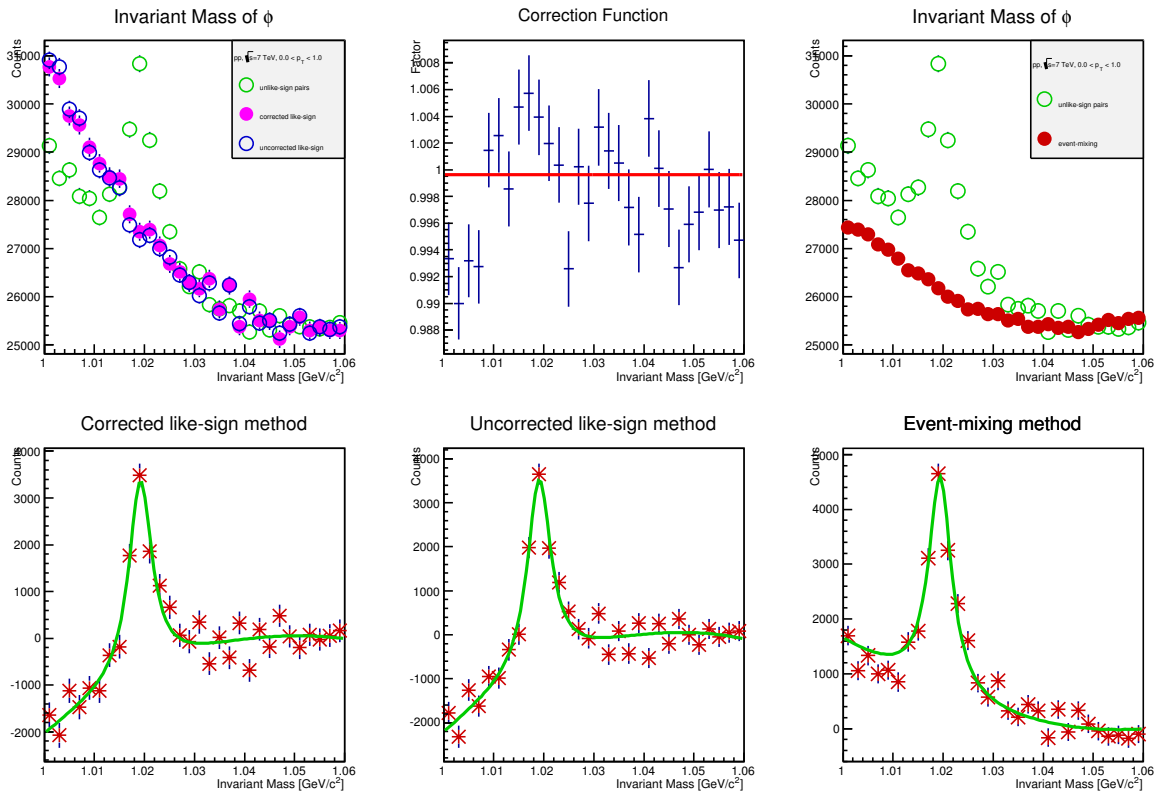

Figure A.1: $\phi(1020)$ fit for p_T between $0 - 1$ GeV/c

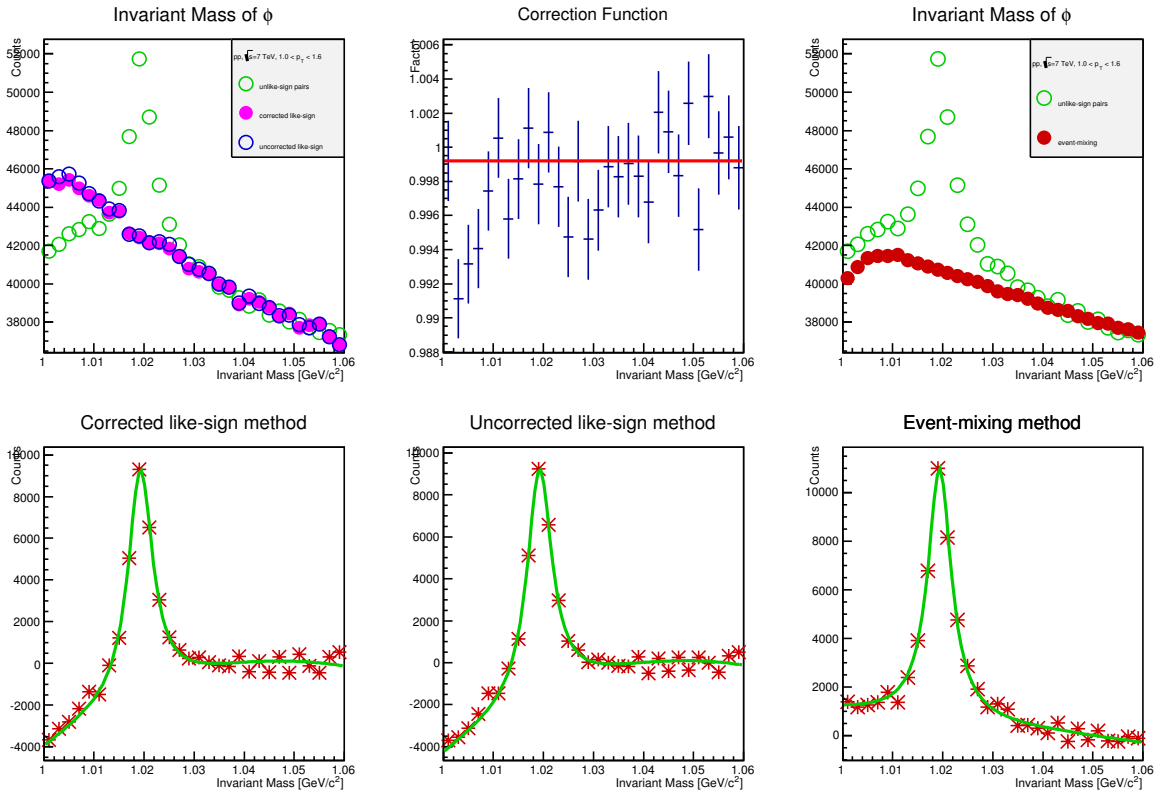

Figure A.2: $\phi(1020)$ fit for p_T between 1 – 1.6 GeV/c

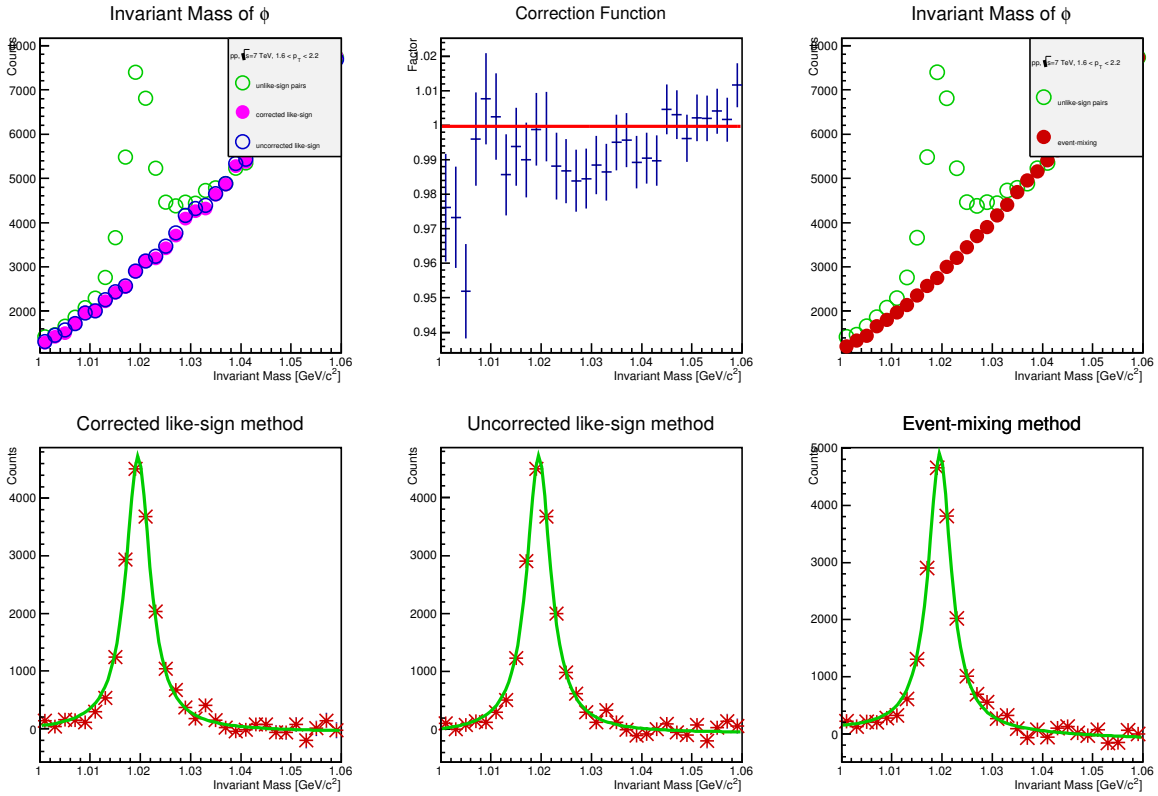

Figure A.3: $\phi(1020)$ fit for p_T between 1.6 – 2.2 GeV/c

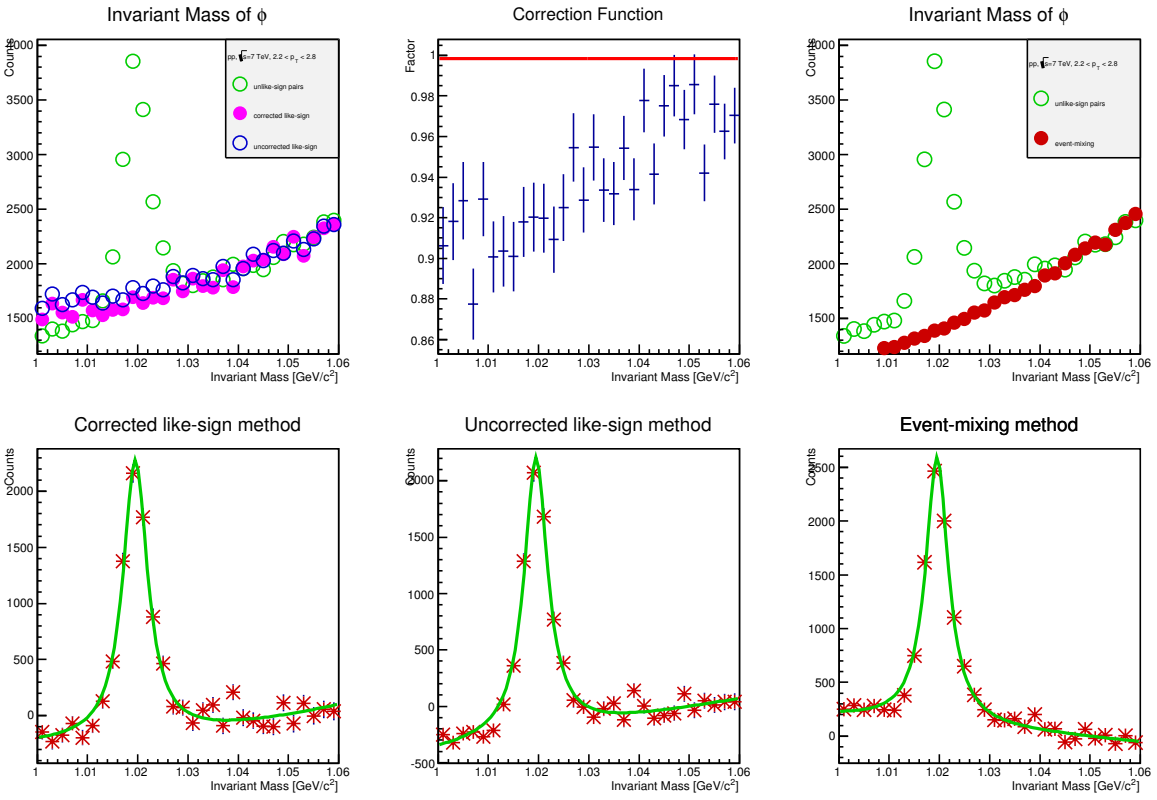

Figure A.4: $\phi(1020)$ fit for p_T between 2.2 – 2.8 GeV/c

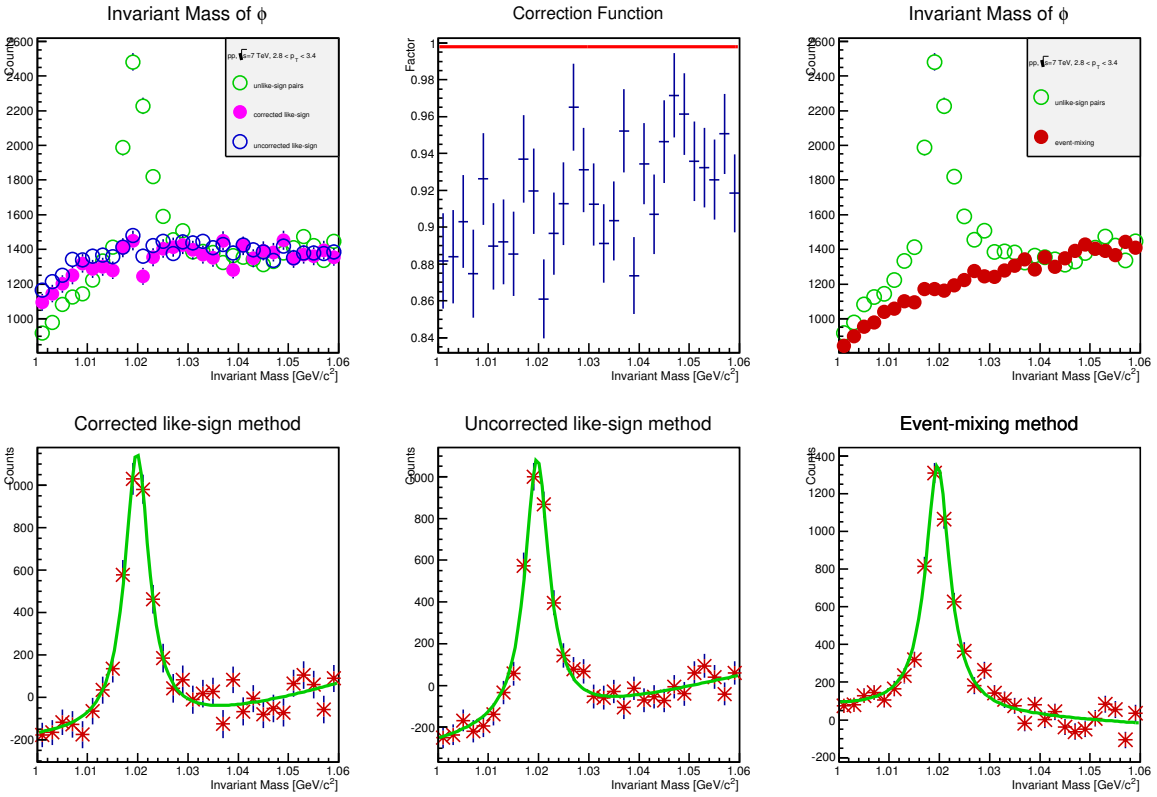

Figure A.5: $\phi(1020)$ fit for p_T between 2.8 – 3.4 GeV/c

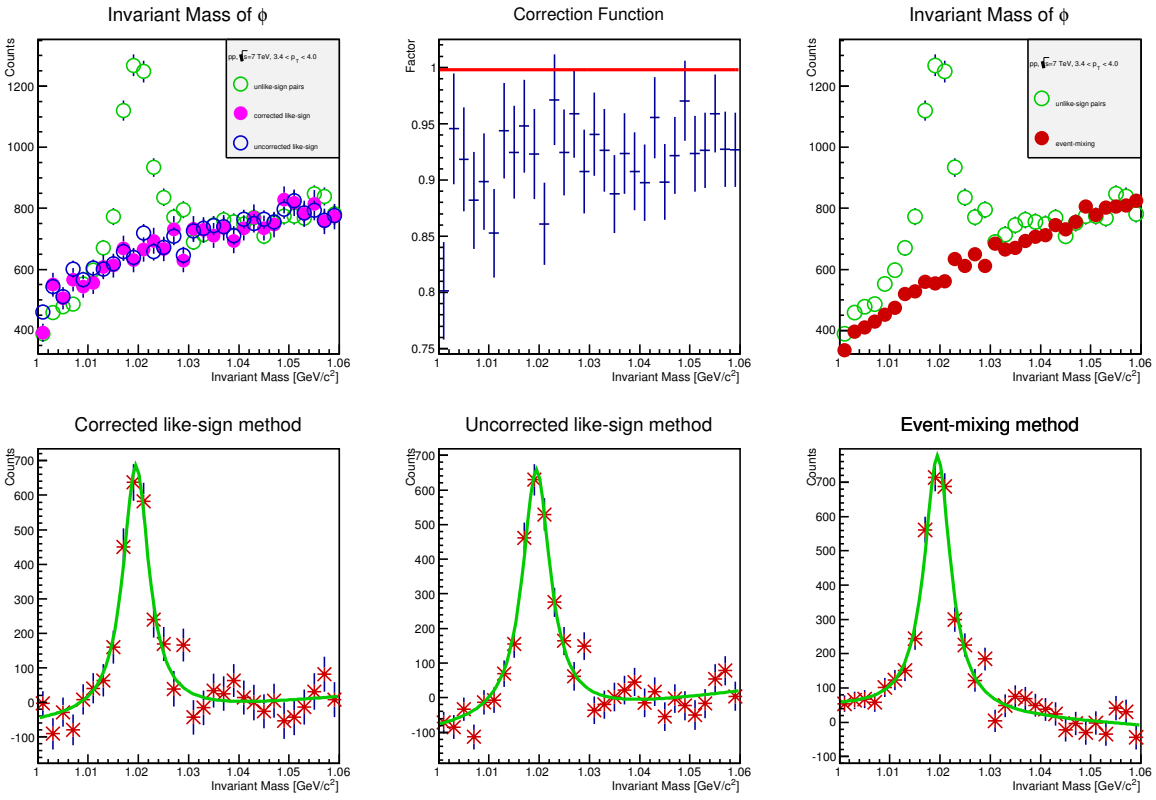

Figure A.6: $\phi(1020)$ fit for p_T between 3.4 – 4.0 GeV/c

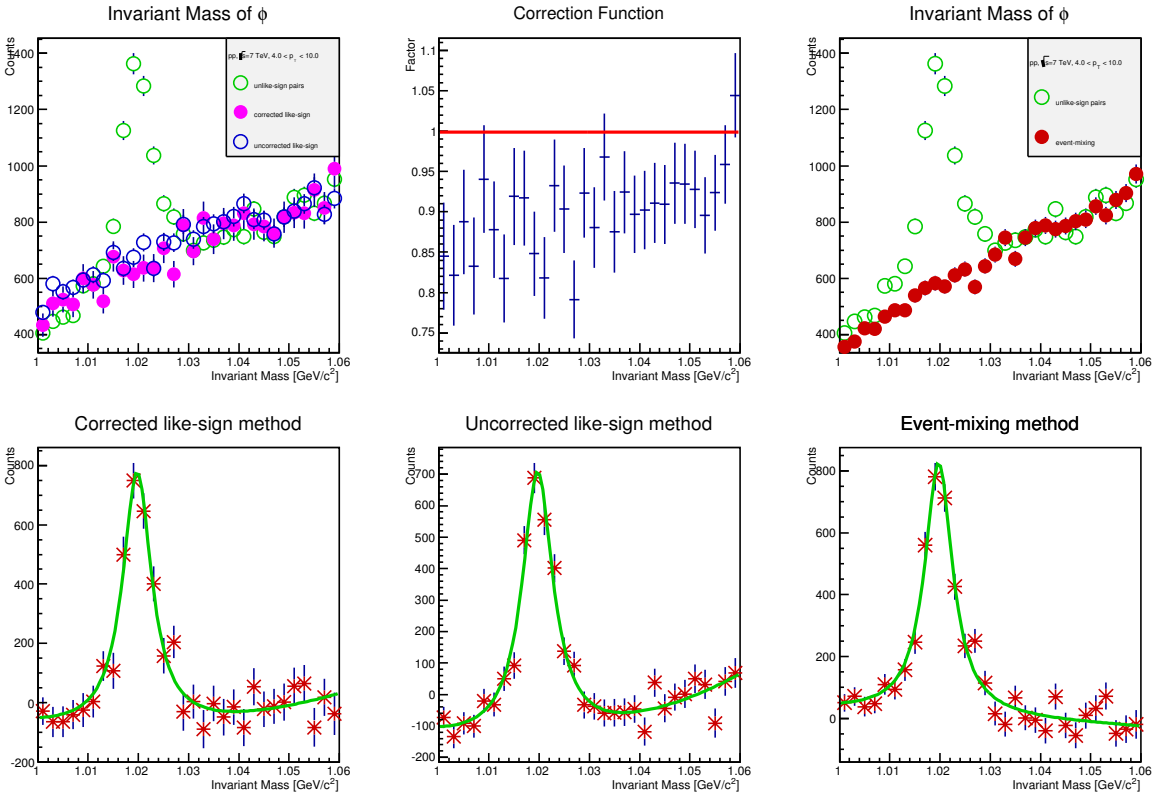

Figure A.7: $\phi(1020)$ fit for p_T between 4.0 – 10.0 GeV/c

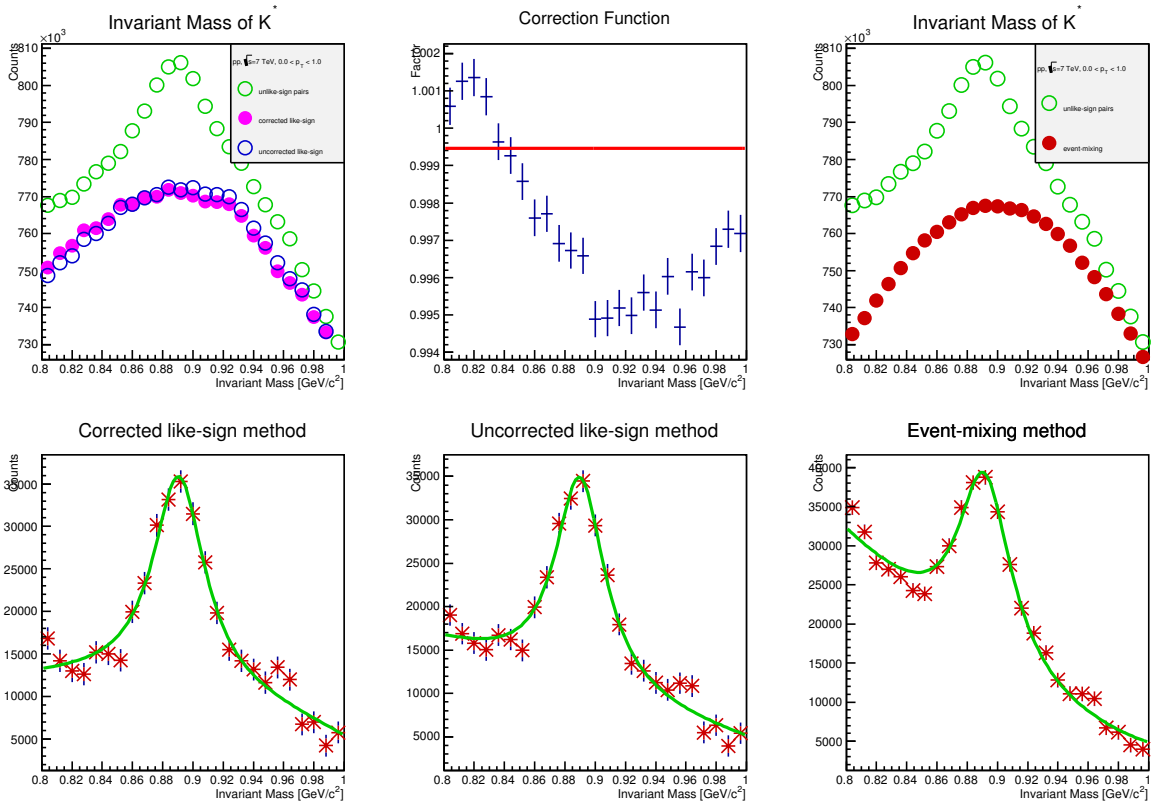

Figure A.8: $K^{*0}(892)$ fit for p_T between 0 – 1 GeV/c

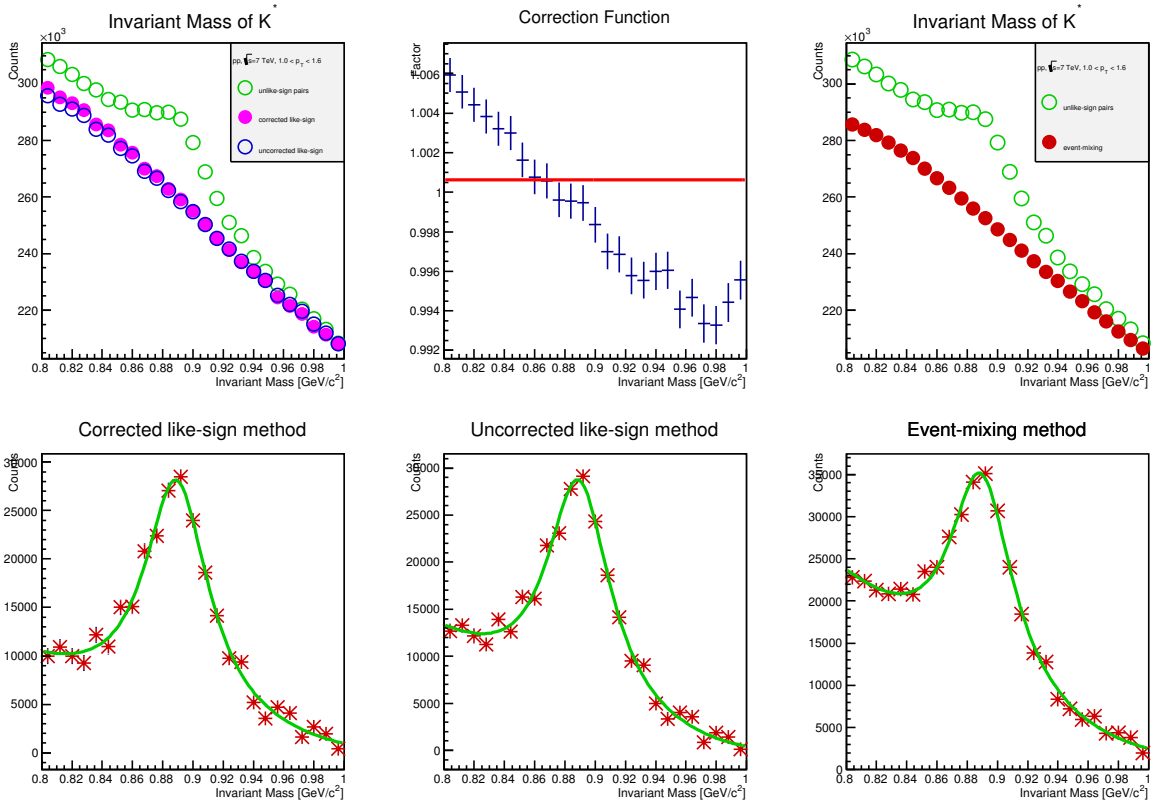

Figure A.9: $K^{*0}(892)$ fit for p_T between 1 – 1.6 GeV/c

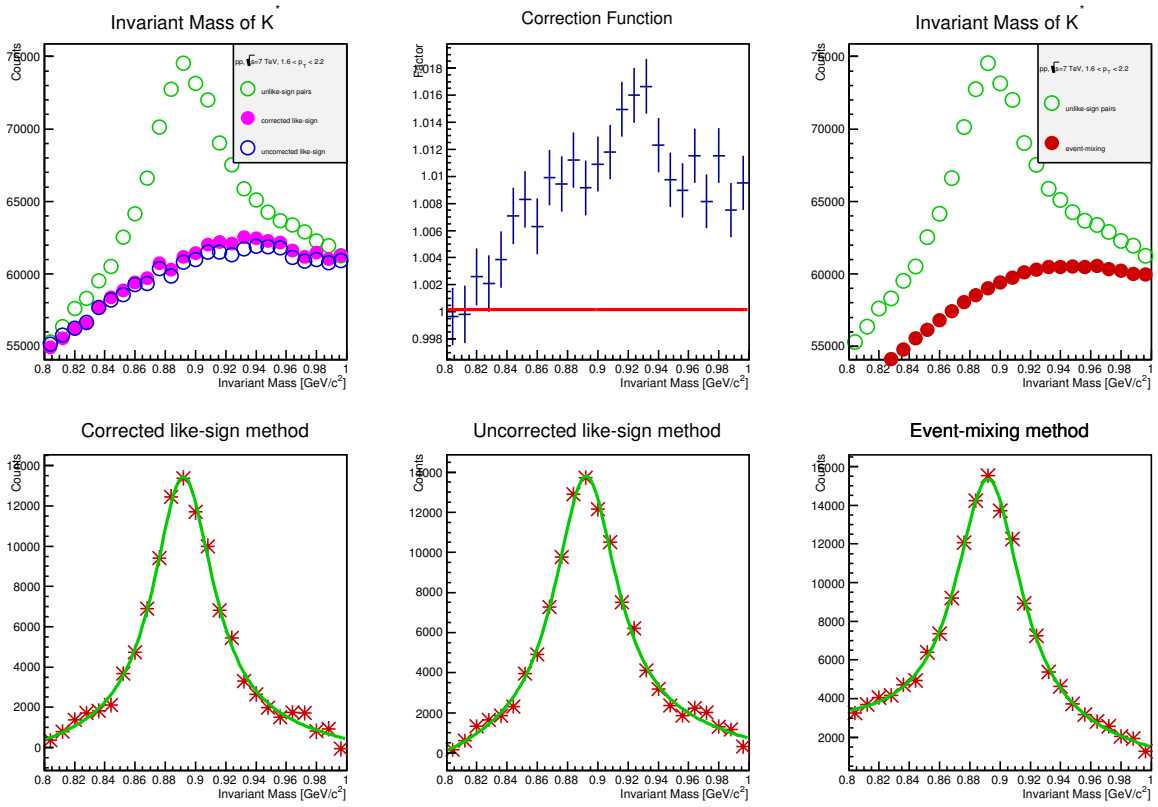

Figure A.10: $K^{*0}(892)$ fit for p_T between 1.6 – 2.2 GeV/c

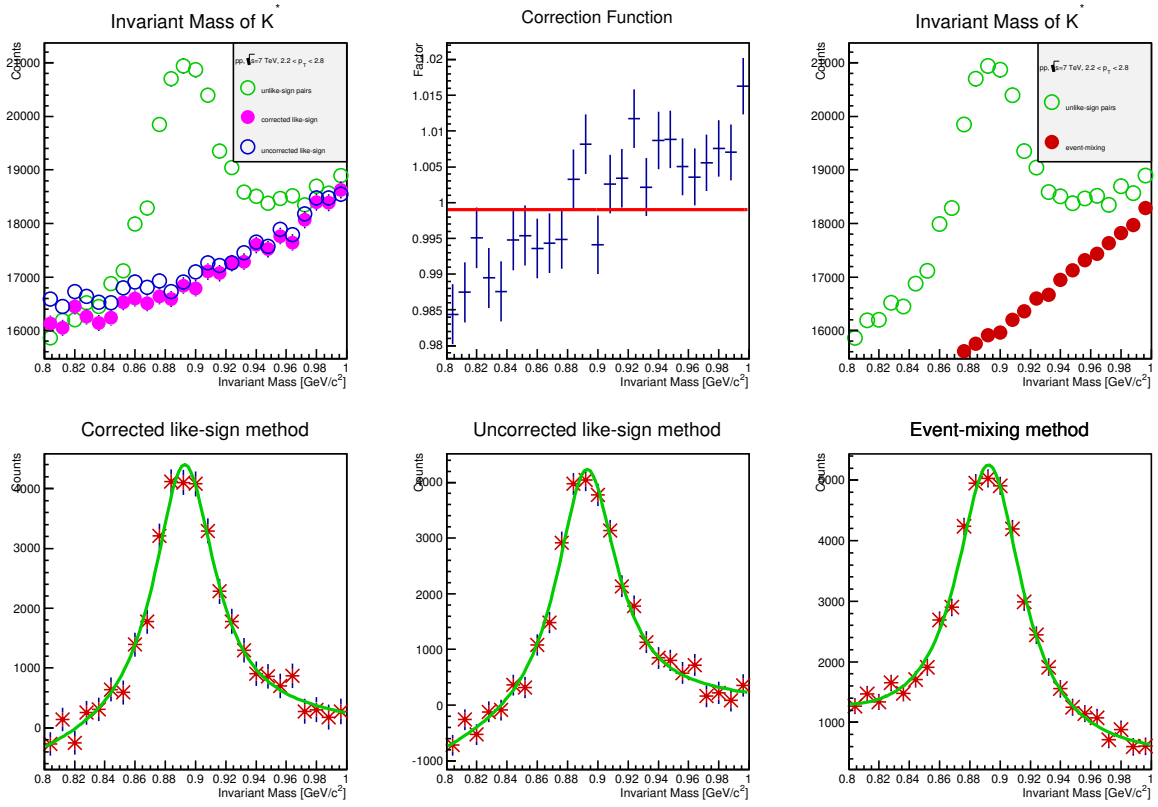

Figure A.11: $K^{*0}(892)$ fit for p_T between 2.2 – 2.8 GeV/c

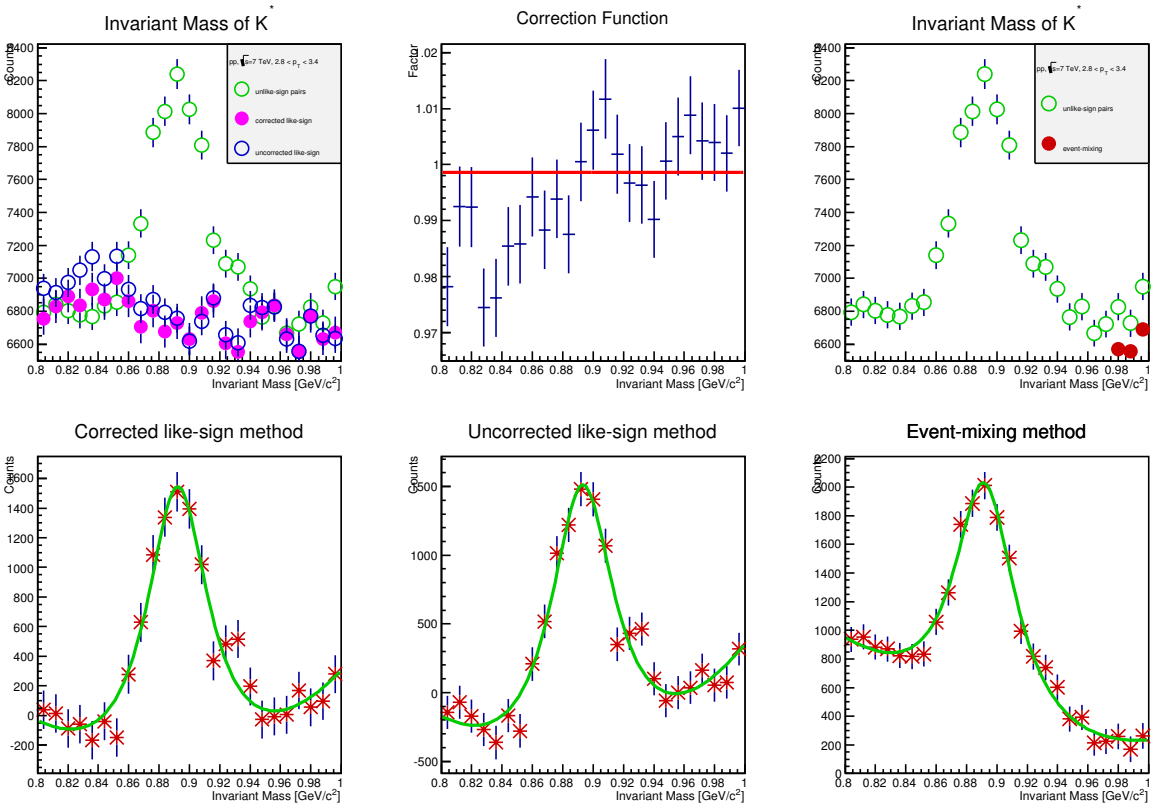

Figure A.12: $K^{*0}(892)$ fit for p_T between 2.8 – 3.4 GeV/c

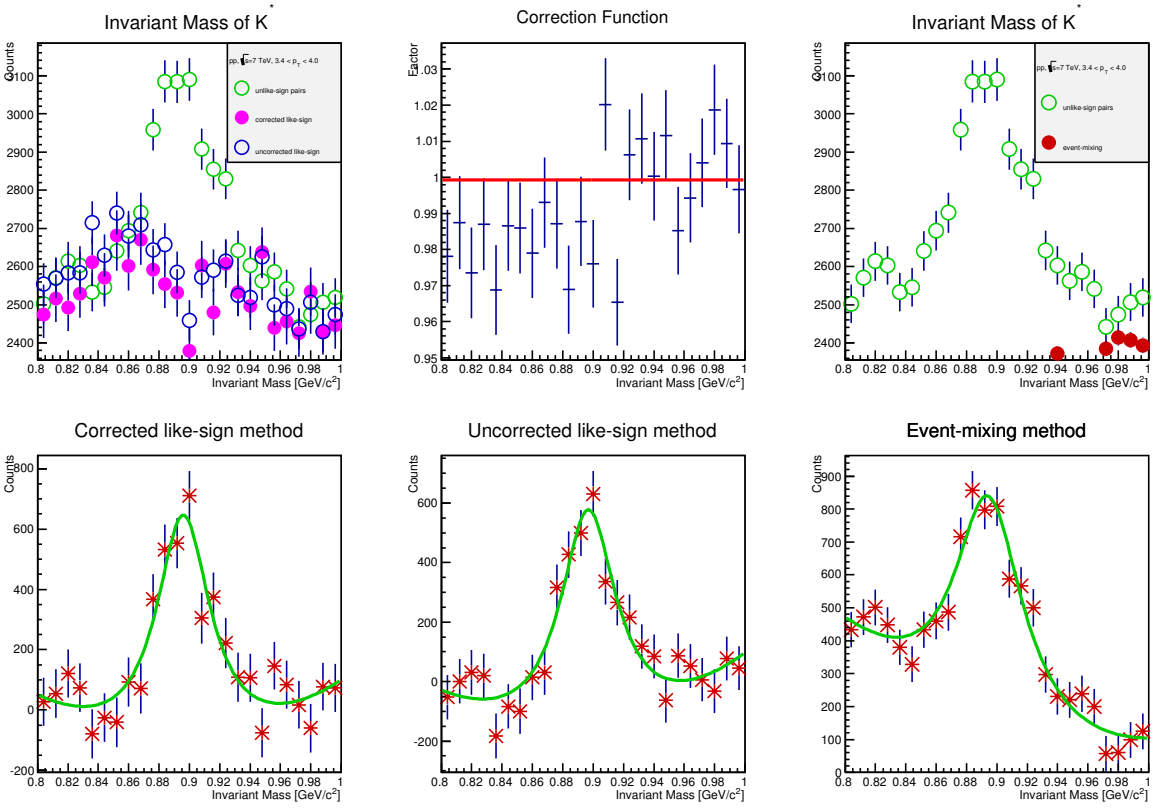

Figure A.13: $K^{*0}(892)$ fit for p_T between 3.4 – 4.0 GeV/c

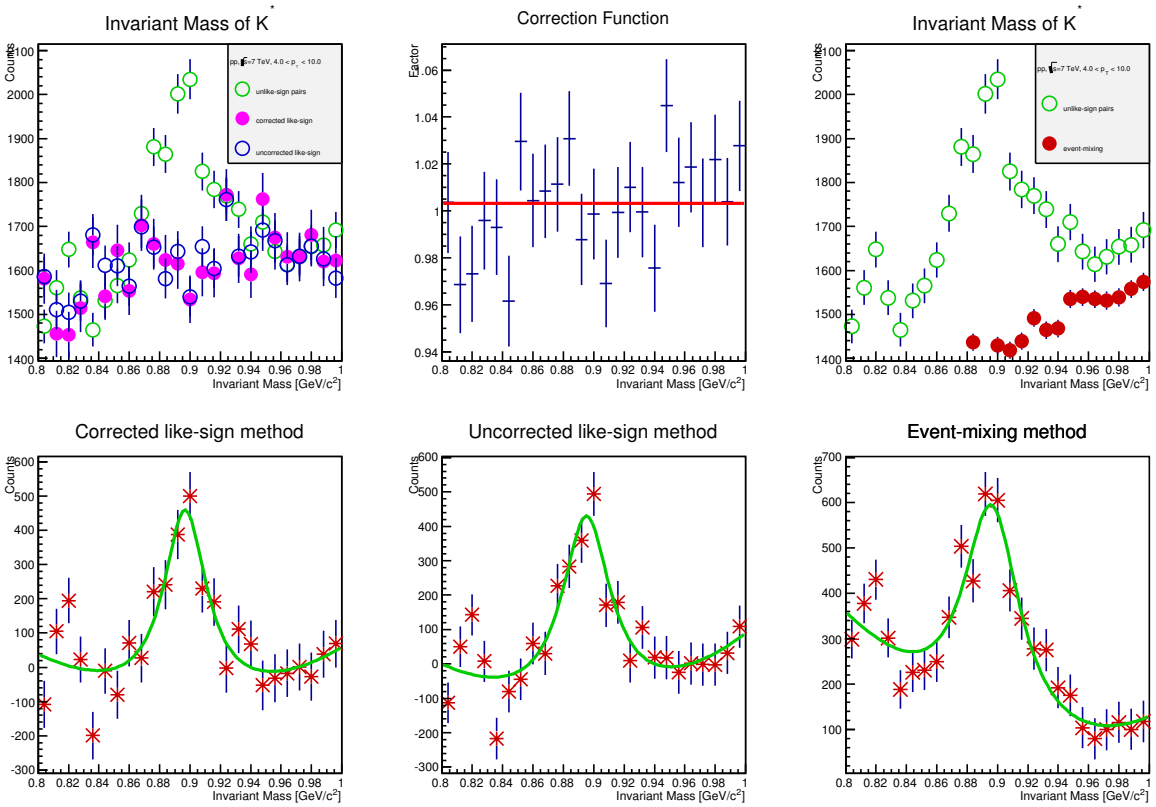

Figure A.14: $K^{*0}(892)$ fit for p_T between 4.0 – 10.0 GeV/c

APPENDIX B

Correction Function

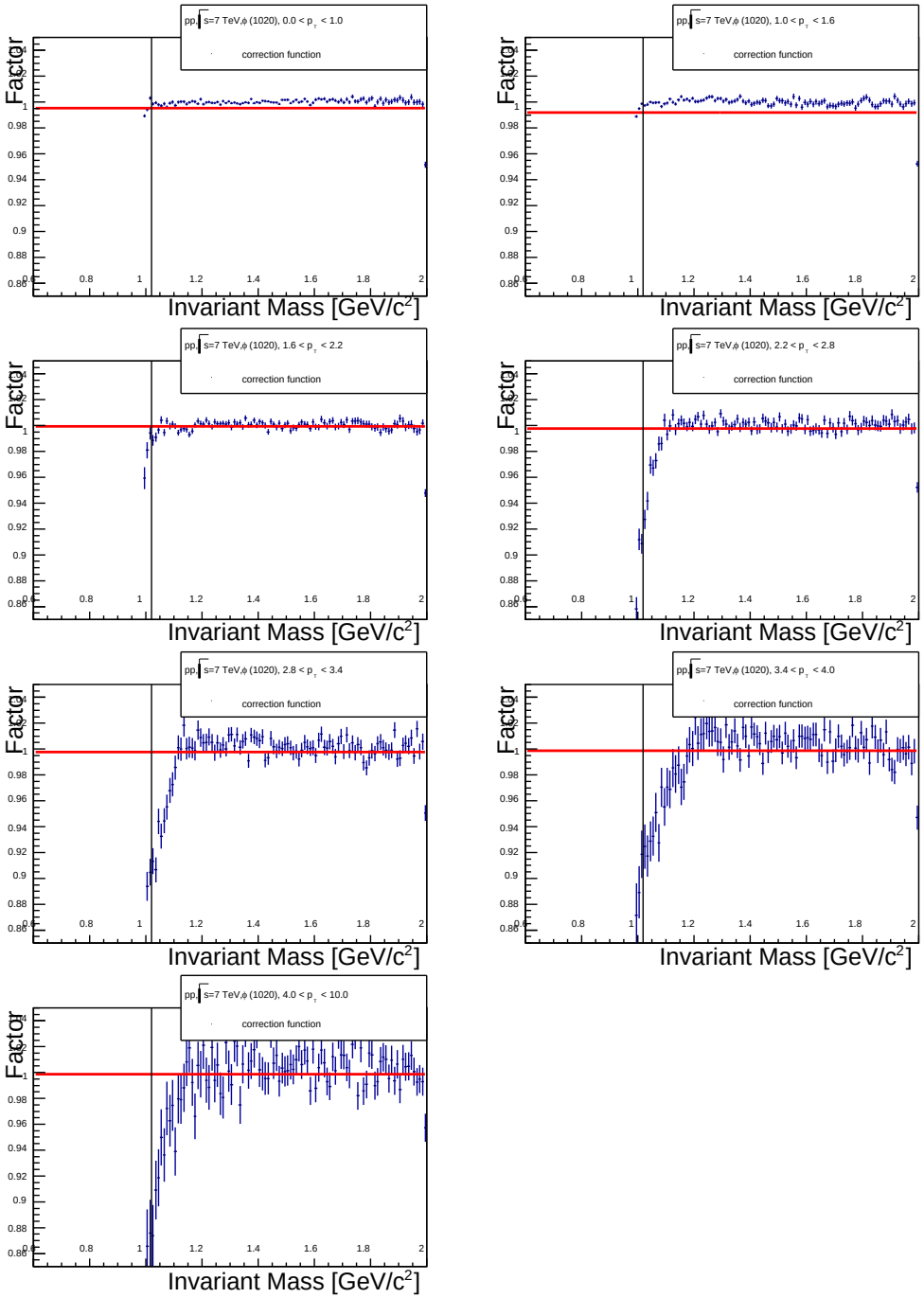

Figure B.1: $\phi(1020)$ correction function.

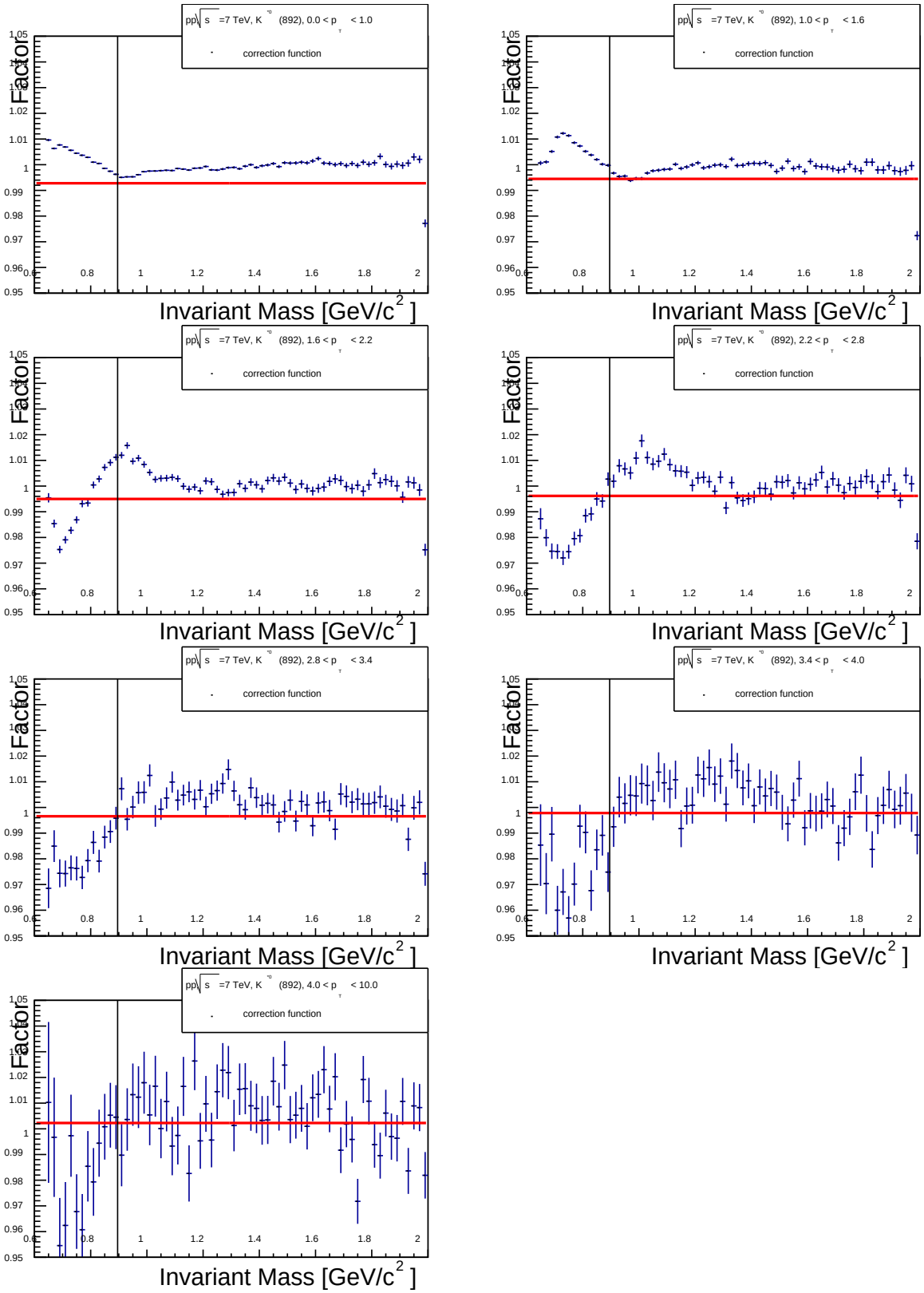

Figure B.2: $K^{*0}(892)$ correction function.

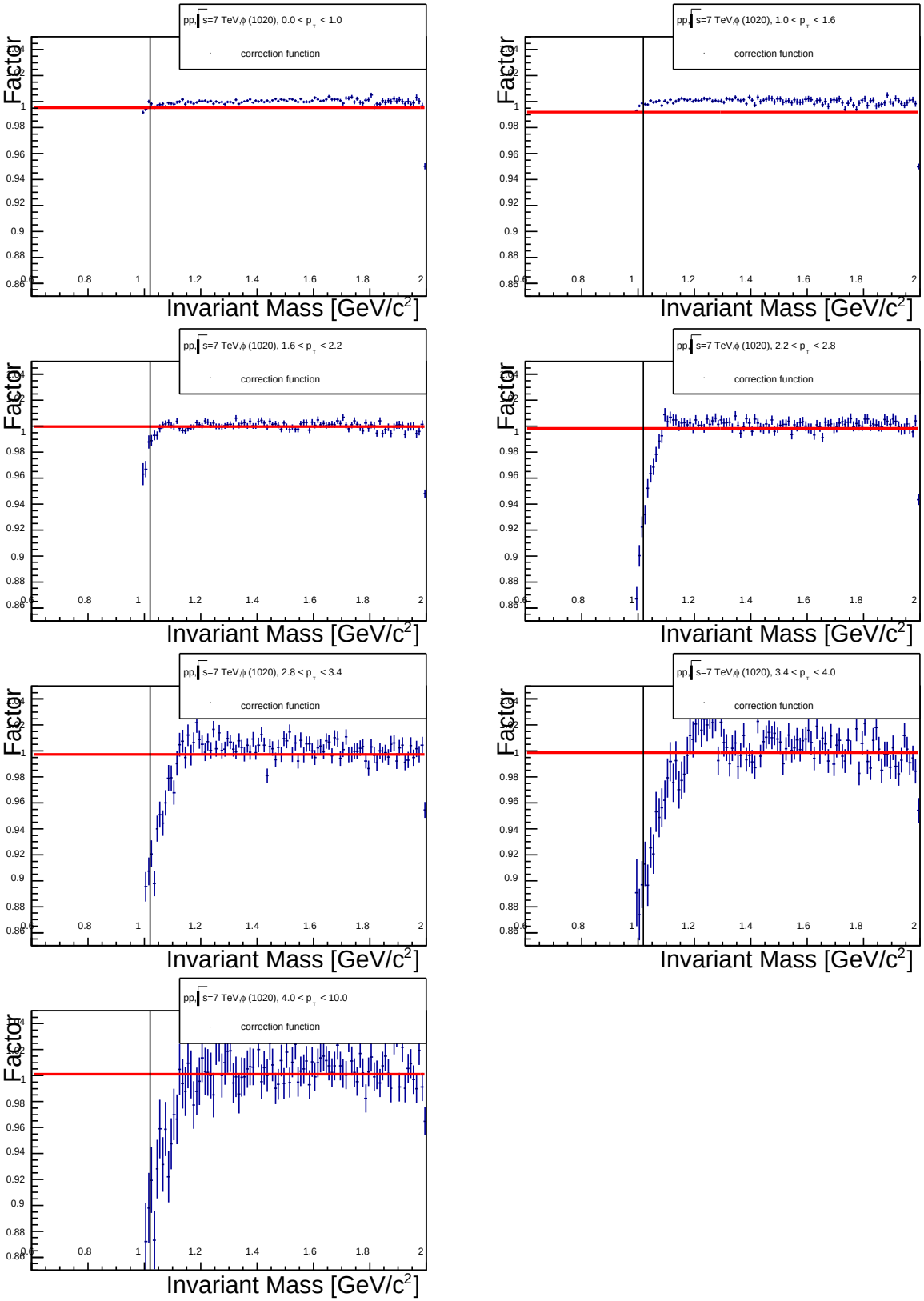

Figure B.3: $\phi(1020)$ correction function. The pair components are not selected i.e. not following the description in Sect. 4.2.

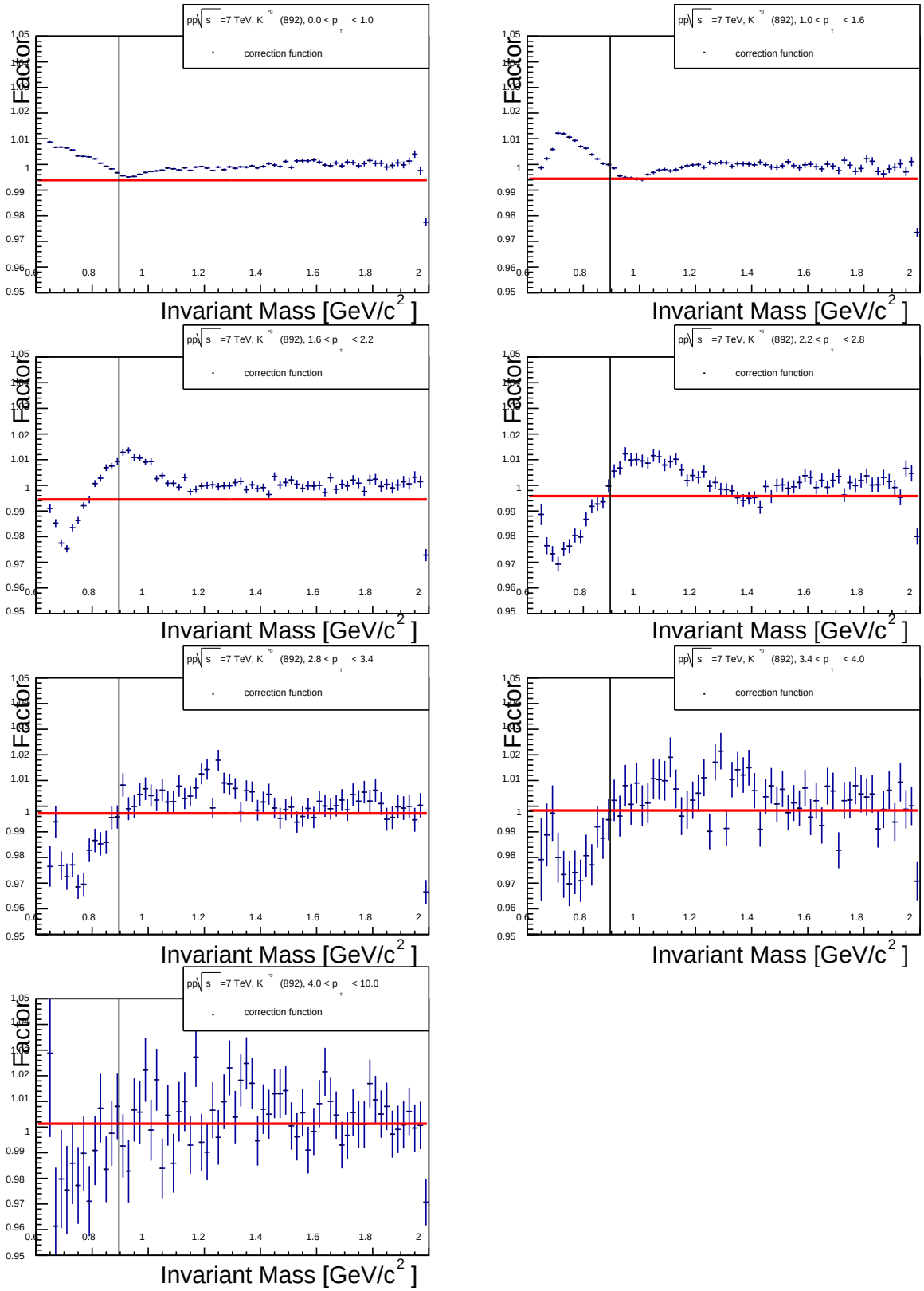

Figure B.4: $K^{*0}(892)$ correction function. The pair components are not selected i.e. not following the description in Sect. 4.2.

APPENDIX C

Inversely Applied Correction

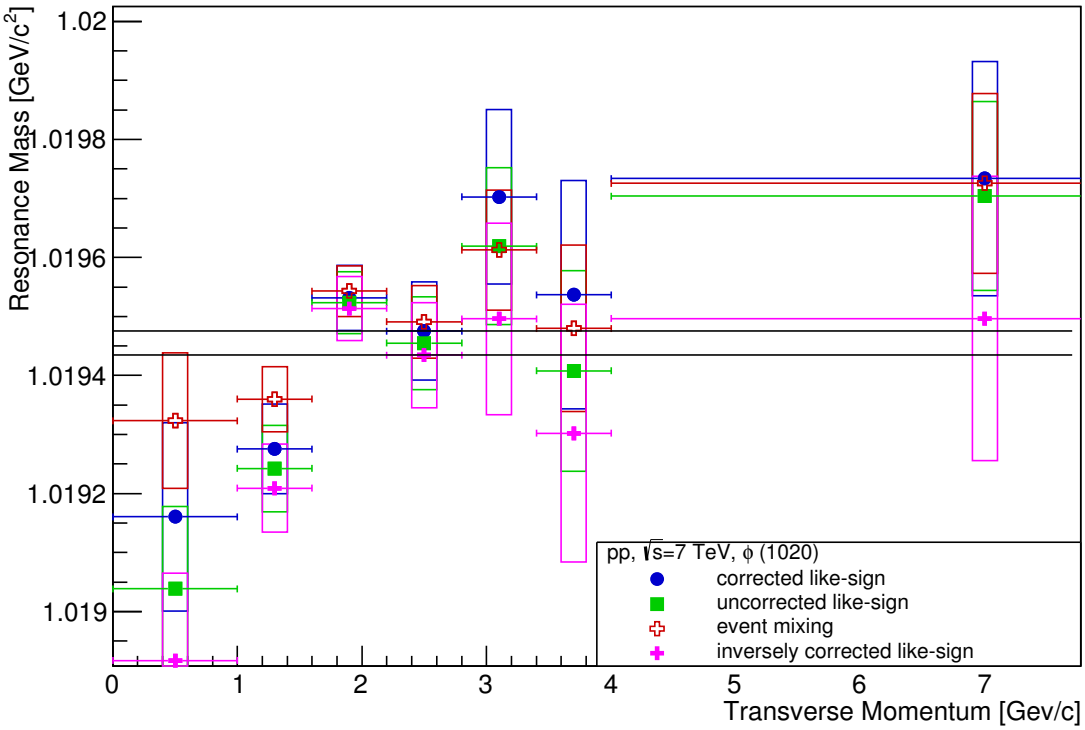

Figure C.1: $\phi(1020)$ mass determined by Breit-Wigner peak for different p_T bins. Errors are only statistical.

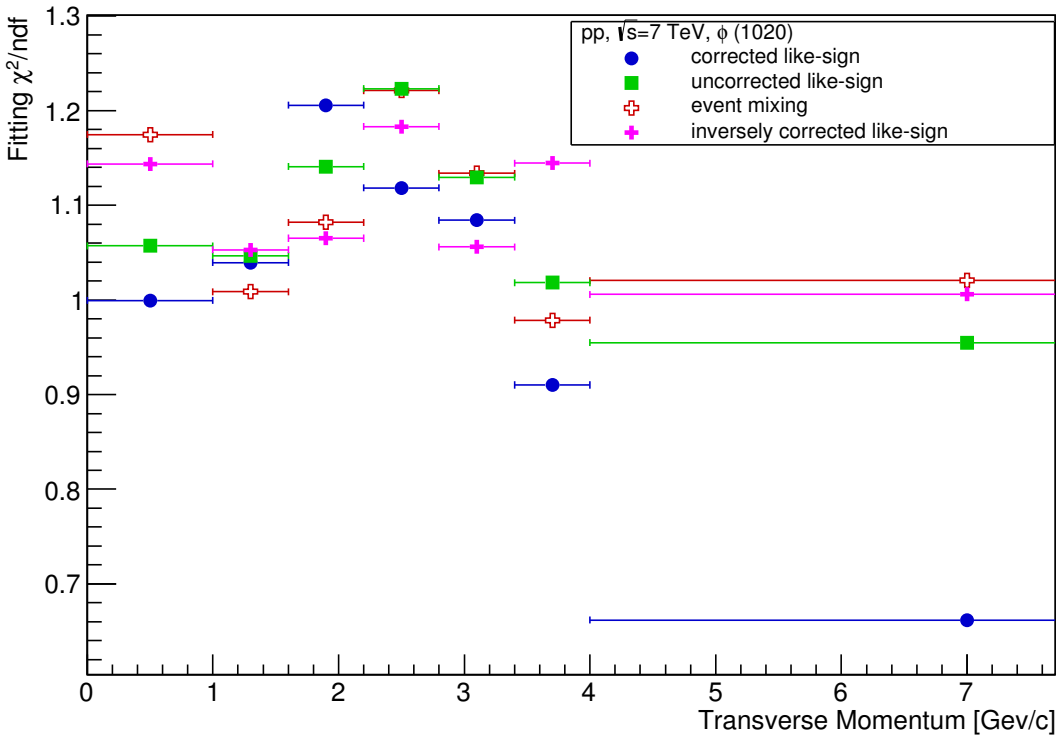

Figure C.3: $\phi(1020)$ fitting quality of Breit-Wigner peak and additional polynomial background for different p_T bins. Lower implies a better fit. Errors only indicate the bin sizes.

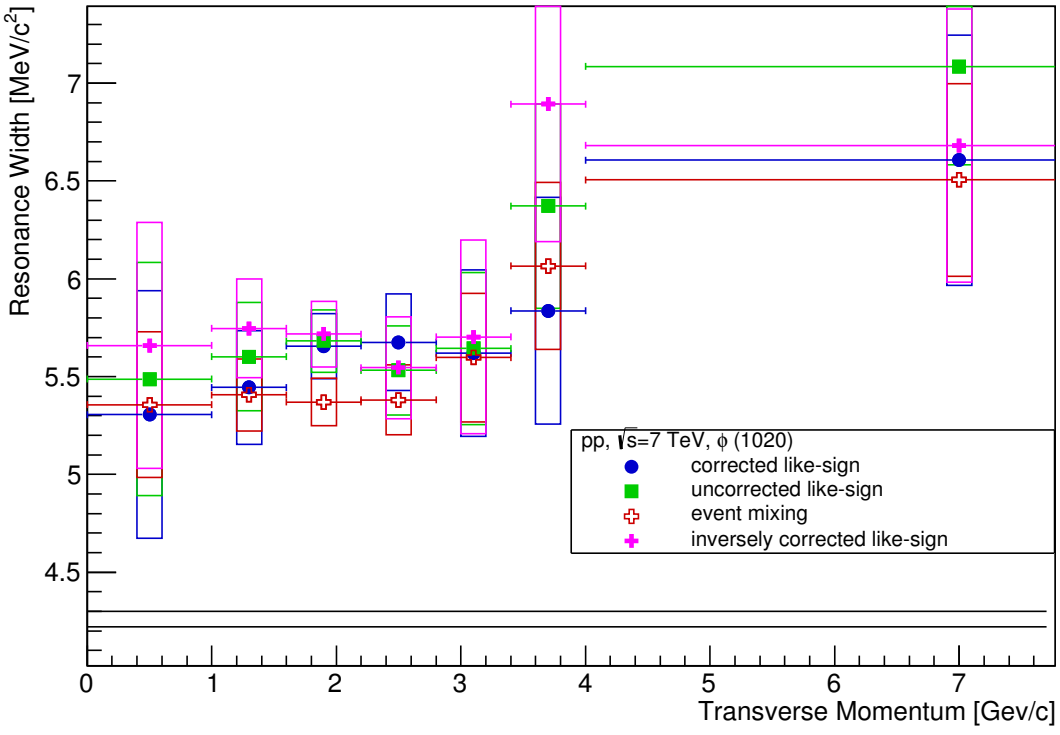

Figure C.2: $\phi(1020)$ width of Breit-Wigner peak for different p_T bins. Errors are only statistical.

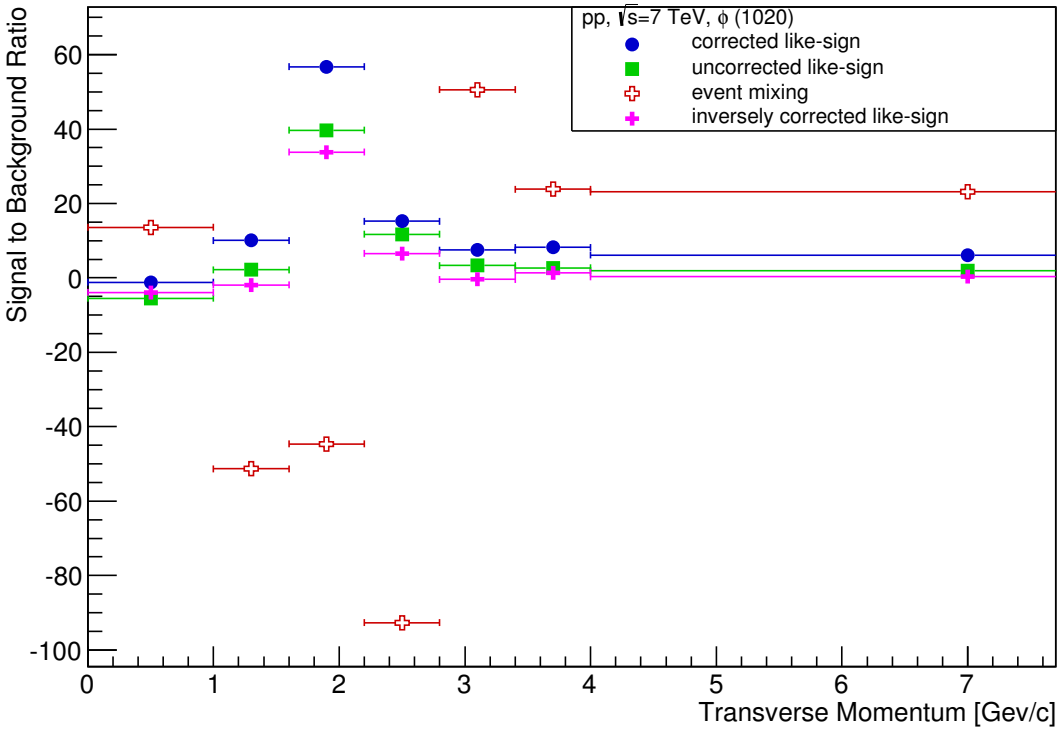

Figure C.4: $\phi(1020)$ signal to residual-background ratio for different p_T bins. Higher implies a better signal extraction. Errors only indicate the bin sizes.

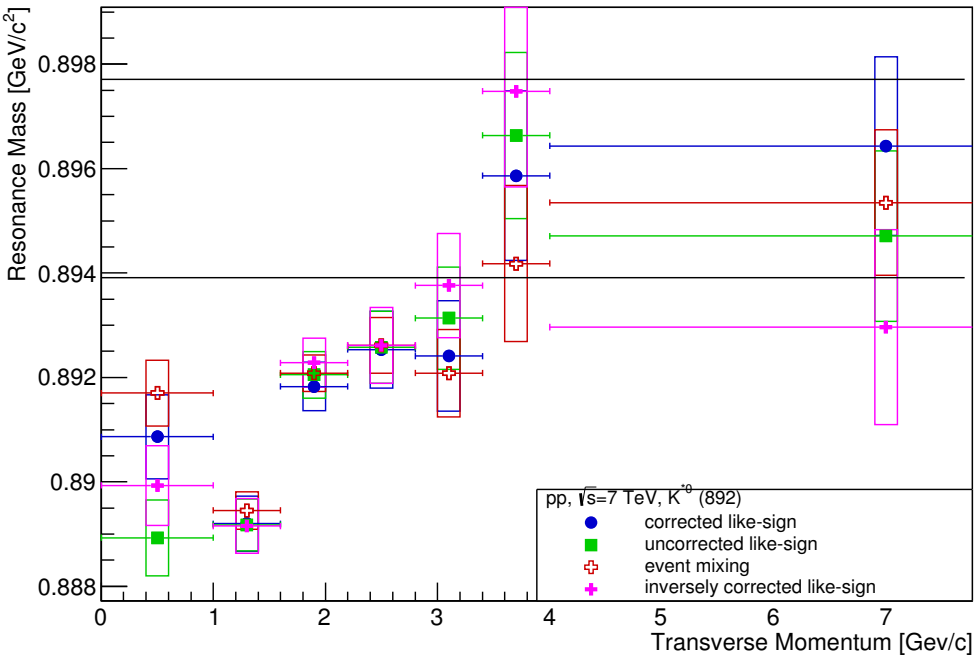

Figure C.5: $K^{*0}(892)$ mass for different p_T bins. Errors are only statistical.

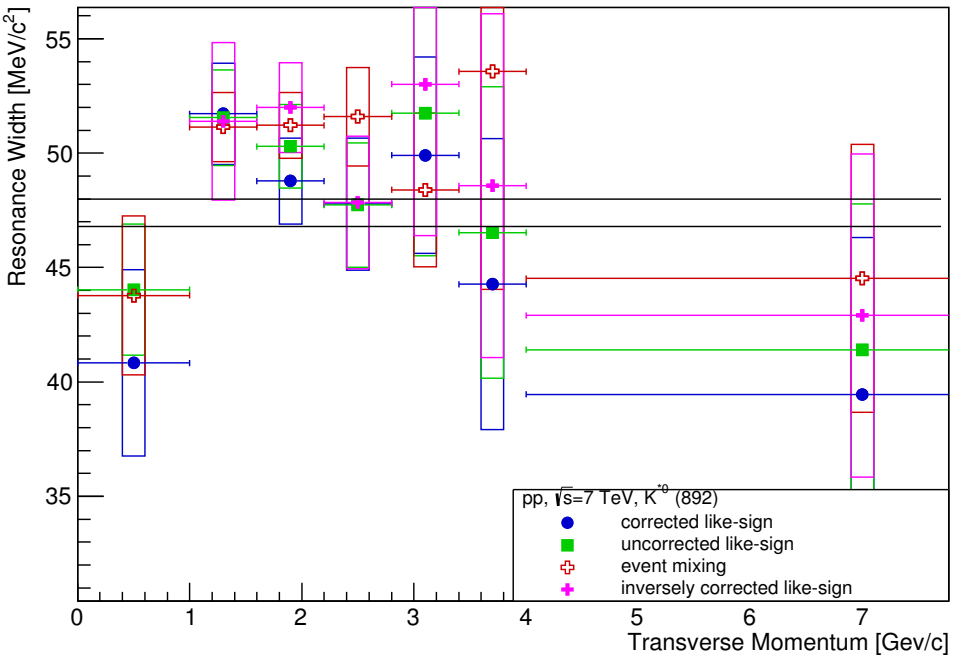

Figure C.6: $K^{*0}(892)$ width for different p_T bins. Errors are only statistical.

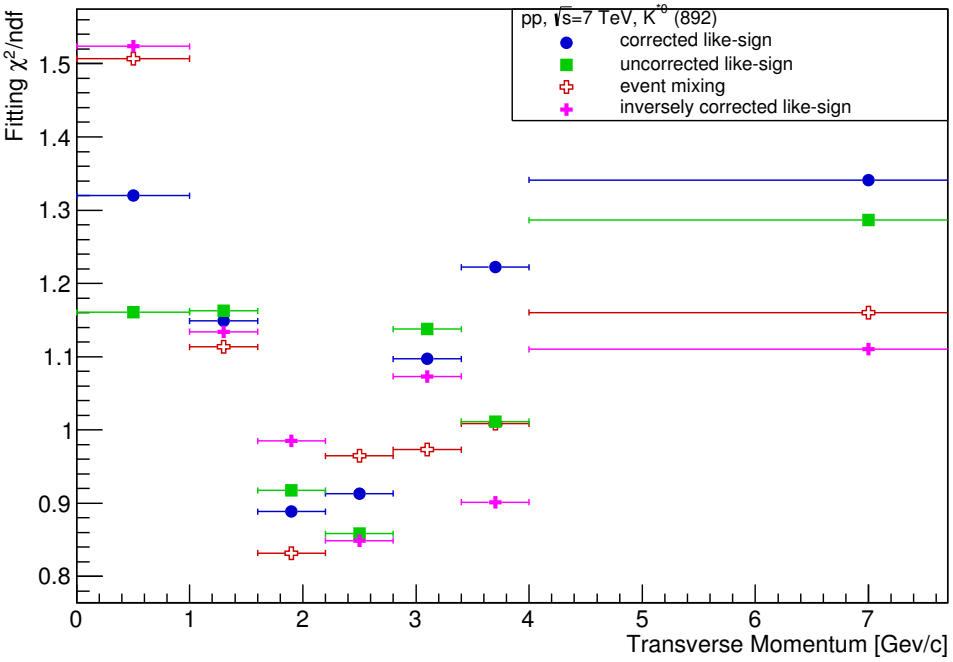

Figure C.7: $K^{*0}(892)$ fitting quality of Breit-Wigner peak and additional polynomial background for different p_T bins. Lower implies a better fit. Errors only indicate the bin sizes.

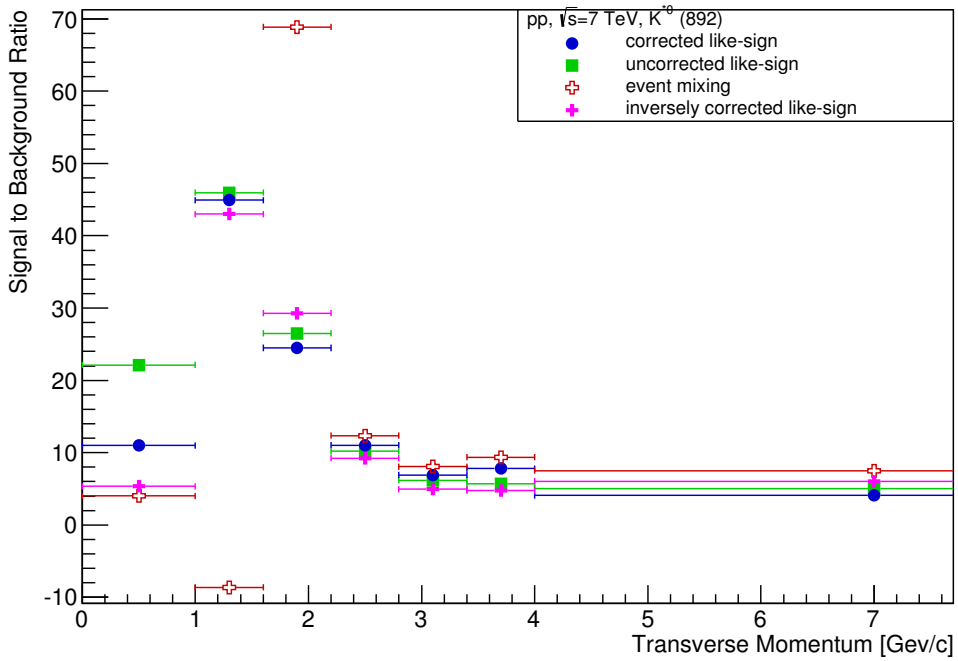

Figure C.8: $K^{*0}(892)$ signal to residual-background ratio for different p_T bins. Higher implies a better fit. Errors only indicate the bin sizes.

APPENDIX D

Weighted event-mixing

D.1 ϕ(1020) resonance, weighted

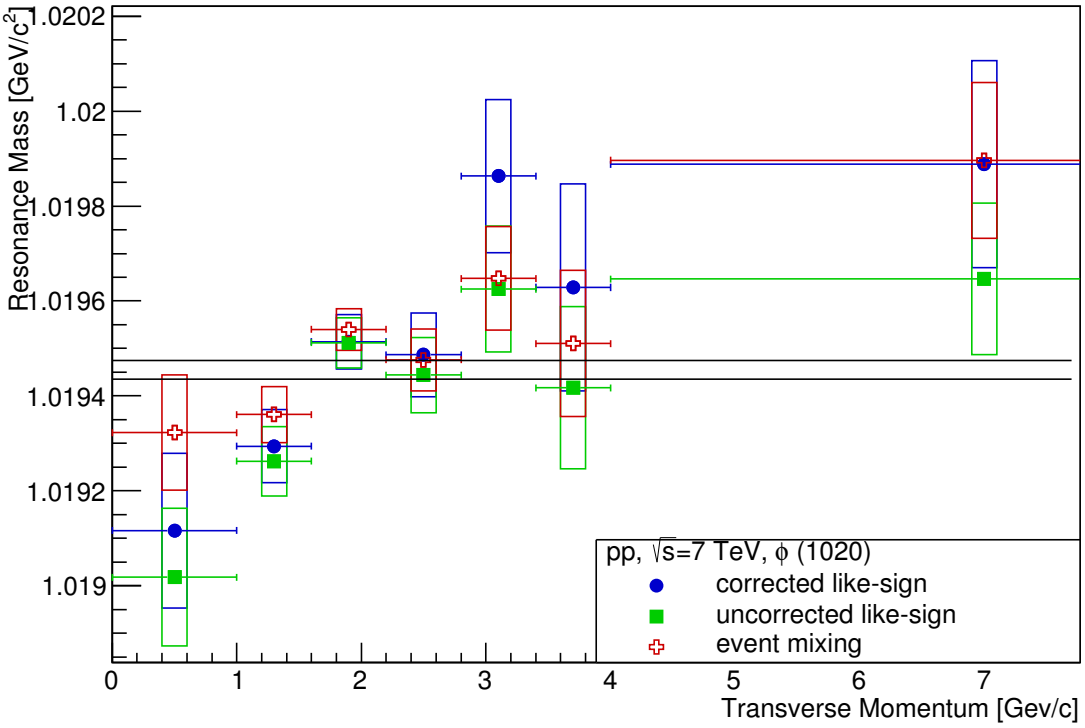

Figure D.1: ϕ(1020) mass determined by Breit-Wigner peak for different p_T bins. Weights have been applied to mix events. Errors are only statistical.

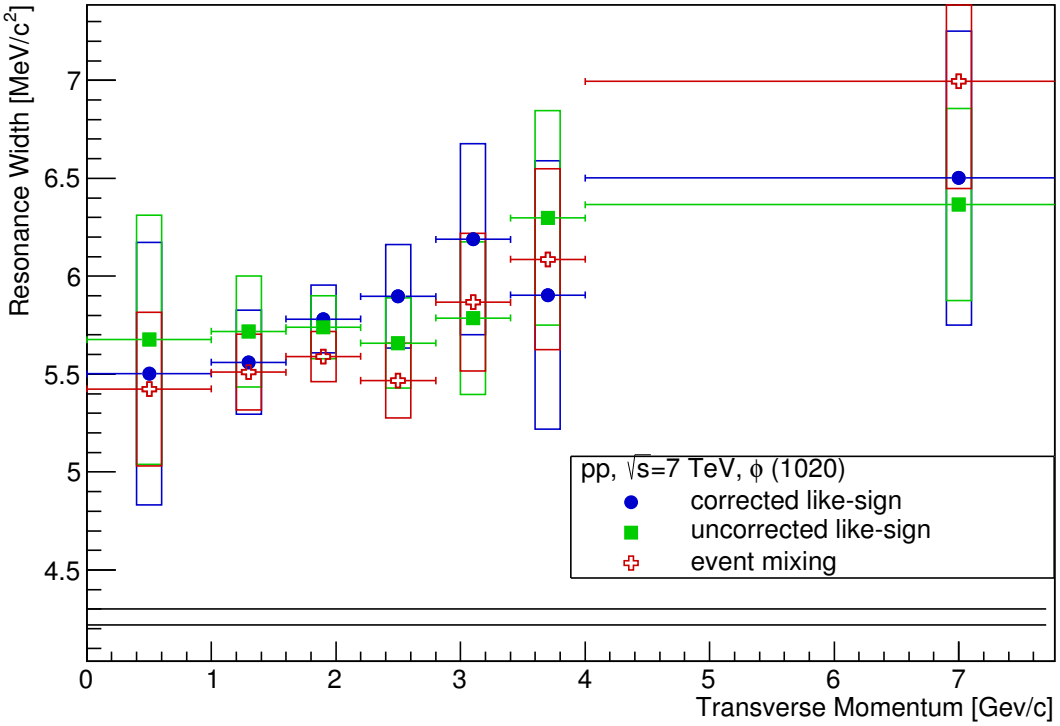

Figure D.2: $\phi(1020)$ width of Breit-Wigner peak for different p_T bins. Weights have been applied to mix events. Errors are only statistical.

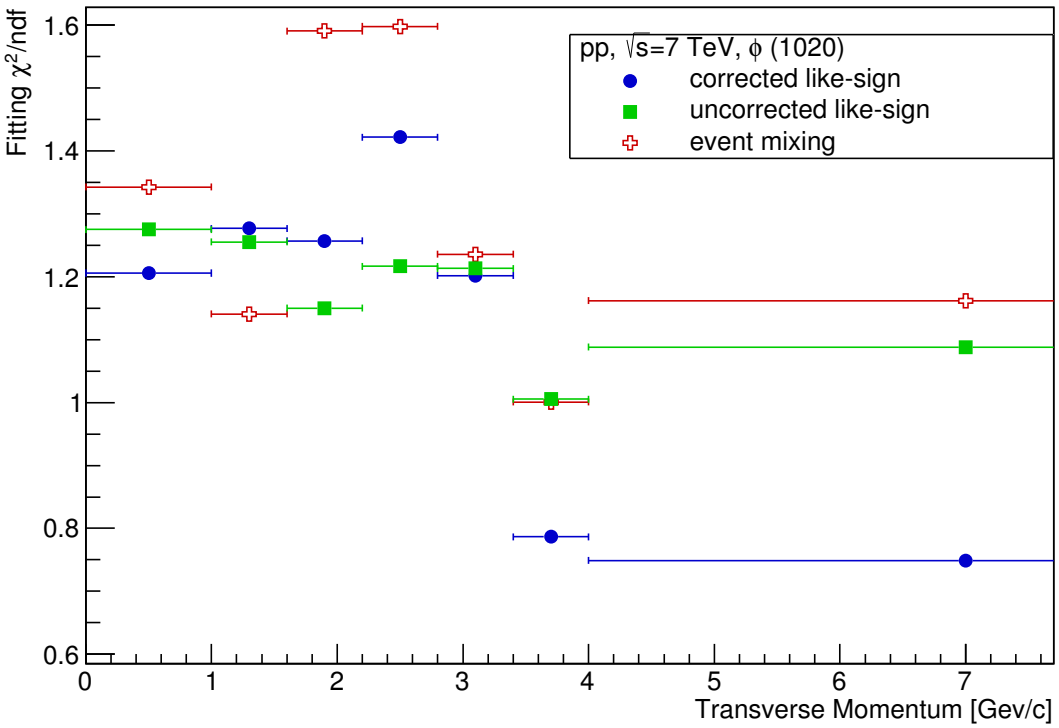

Figure D.3: $\phi(1020)$ fitting quality of Breit-Wigner peak and additional polynomial background for different p_T bins. Weights have been applied to mix events. Lower implies a better fit. Errors only indicate the bin sizes.

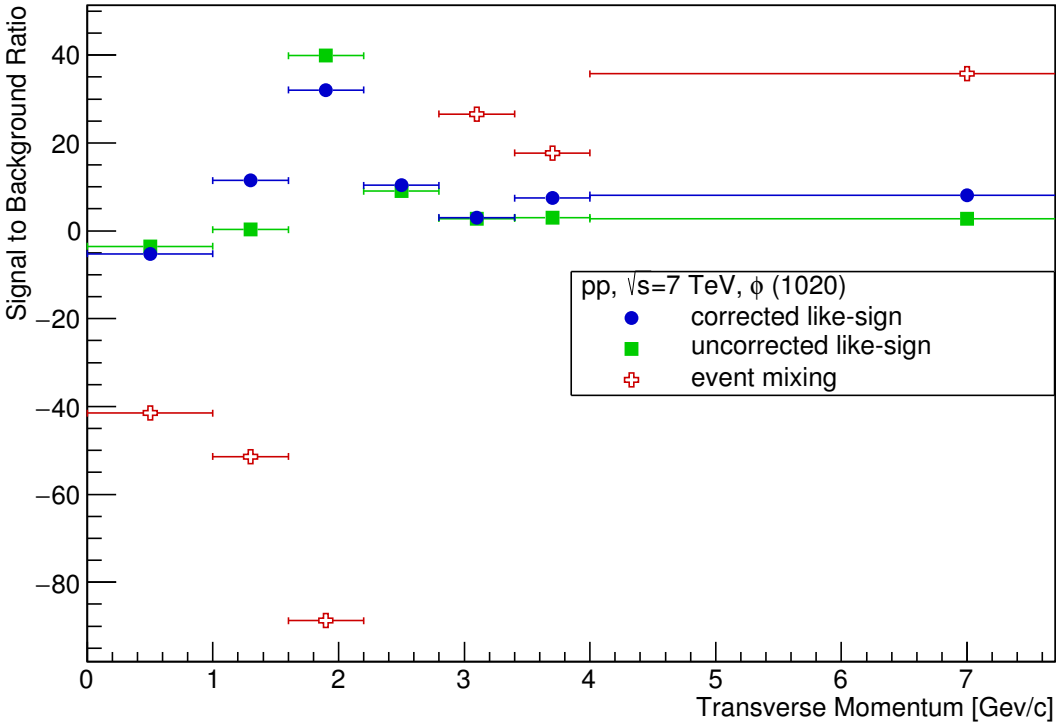

Figure D.4: $\phi(1020)$ signal to residual-background ratio for different p_T bins. Weights have been applied to mix events. Higher implies a better signal extraction. Errors only indicate the bin sizes.

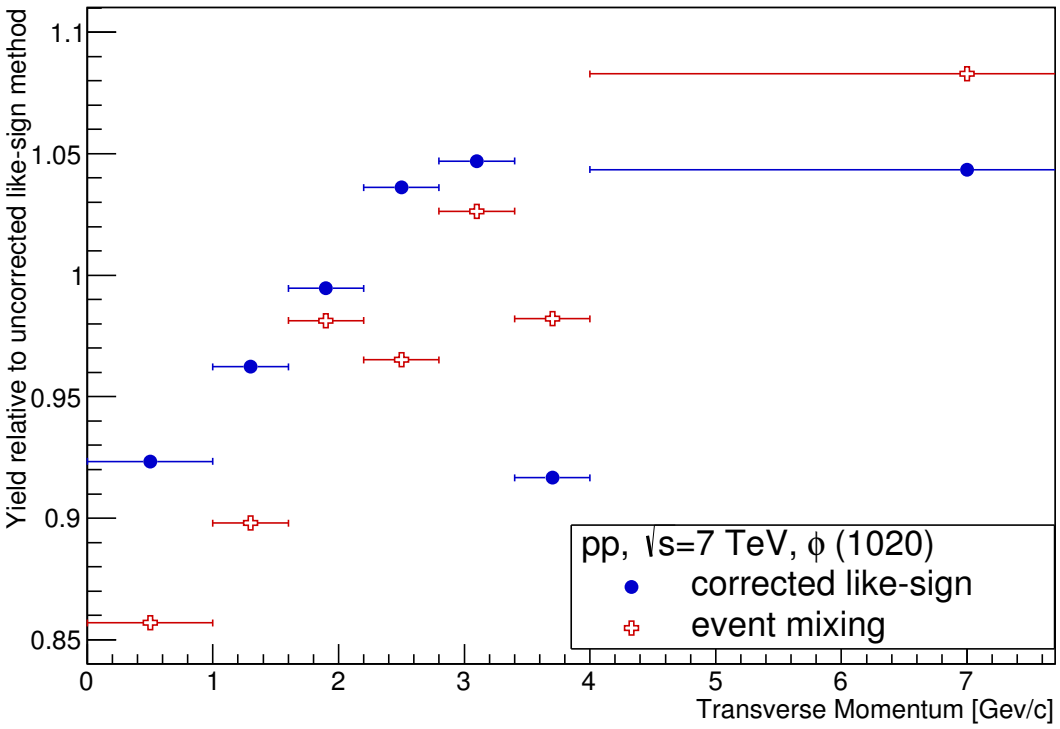

Figure D.5: $\phi(1020)$ relative yield for different p_T bins. Weights have been applied to mix events. Errors only indicate the bin sizes.

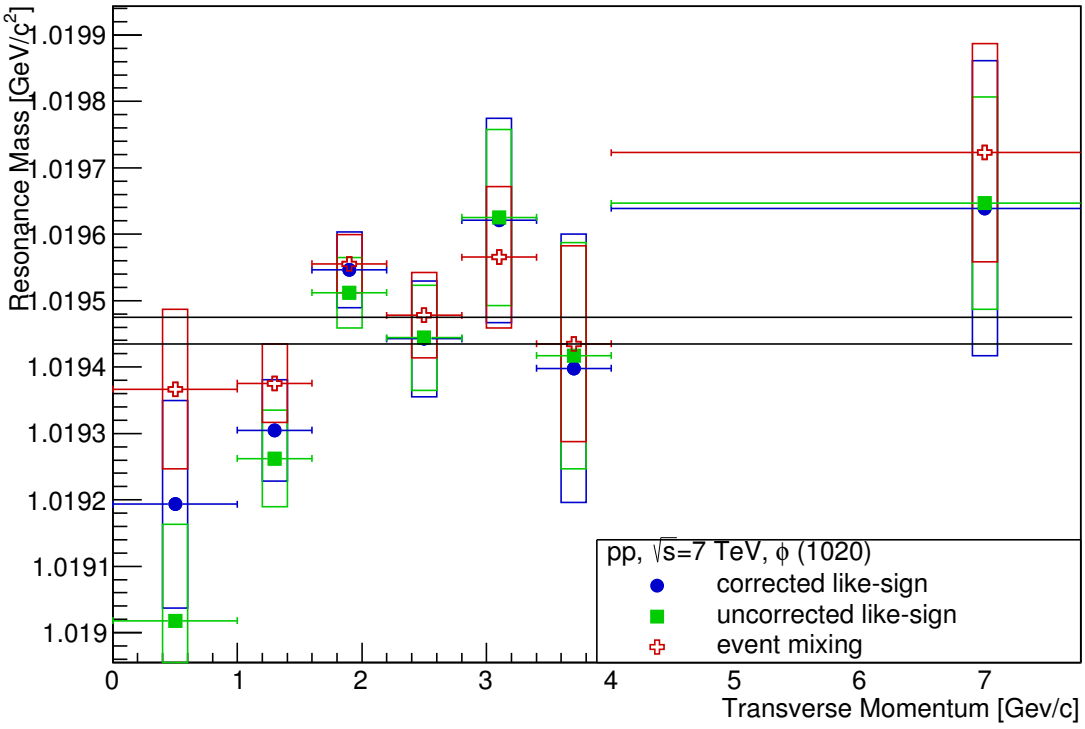

Figure D.6: $\phi(1020)$ mass determined by Breit-Wigner peak for different p_T bins. Inverted weights have been applied to mix events. Errors are only statistical.

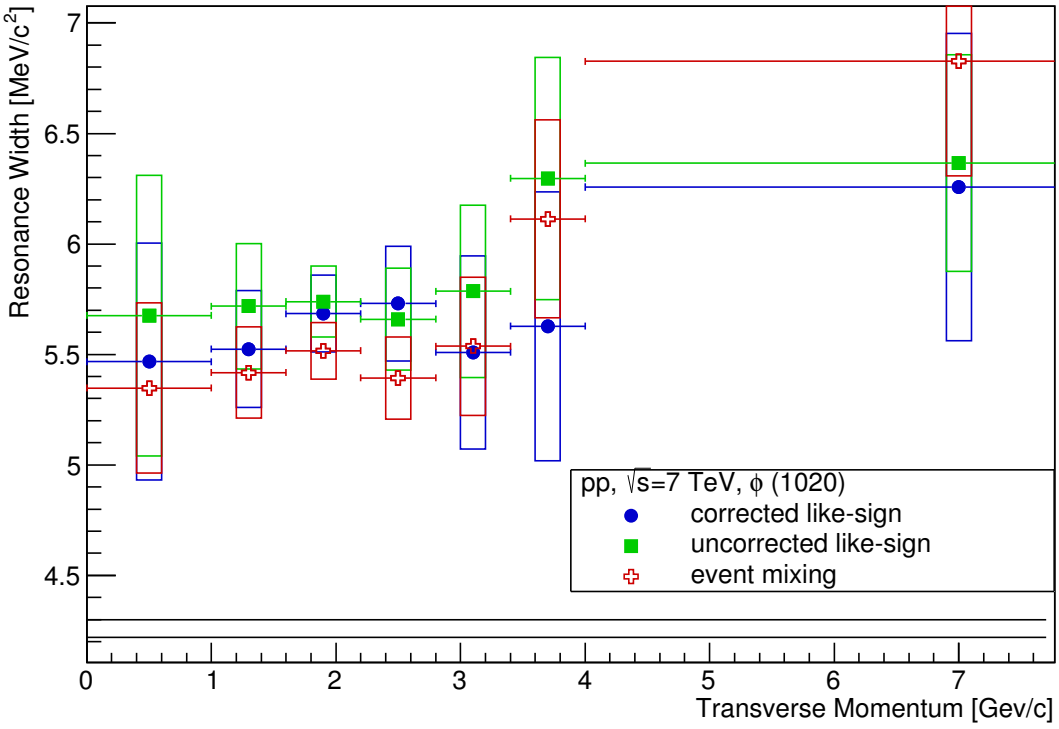

Figure D.7: $\phi(1020)$ width of Breit-Wigner peak for different p_T bins. Inverted weights have been applied to mix events. Errors are only statistical.

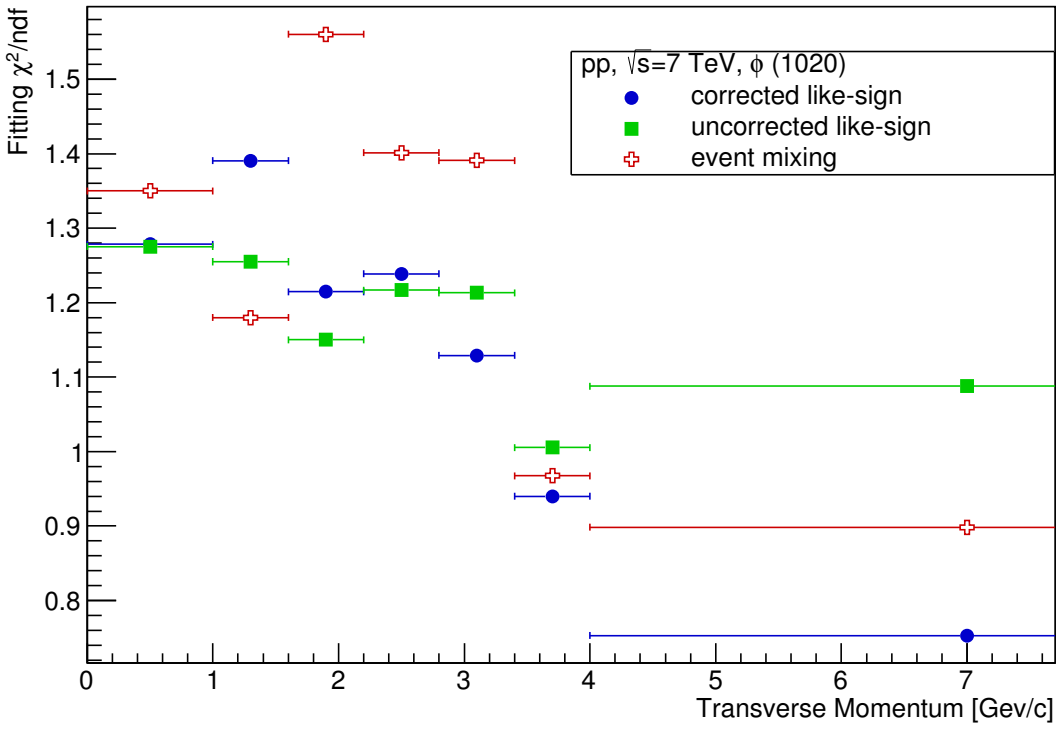

Figure D.8: $\phi(1020)$ fitting quality of Breit-Wigner peak and additional polynomial background for different p_T bins. Inverted weights have been applied to mix events. Lower implies a better fit. Errors only indicate the bin sizes.

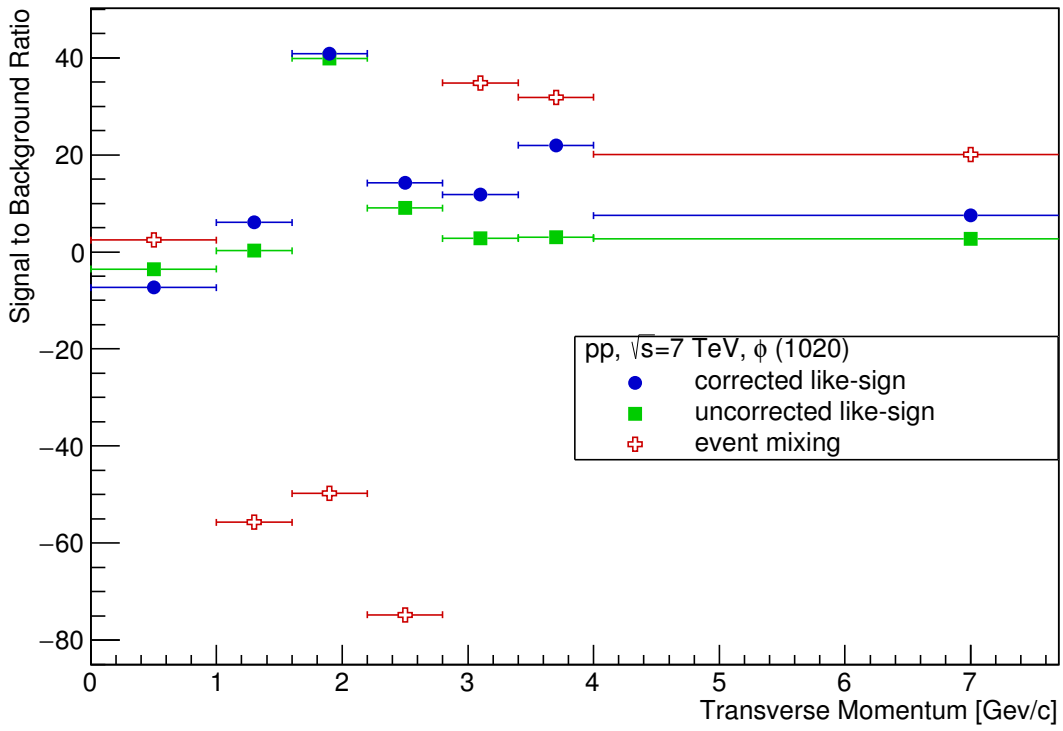

Figure D.9: $\phi(1020)$ signal to residual-background ratio for different p_T bins. Inverted weights have been applied to mix events. Higher implies a better signal extraction. Errors only indicate the bin sizes.

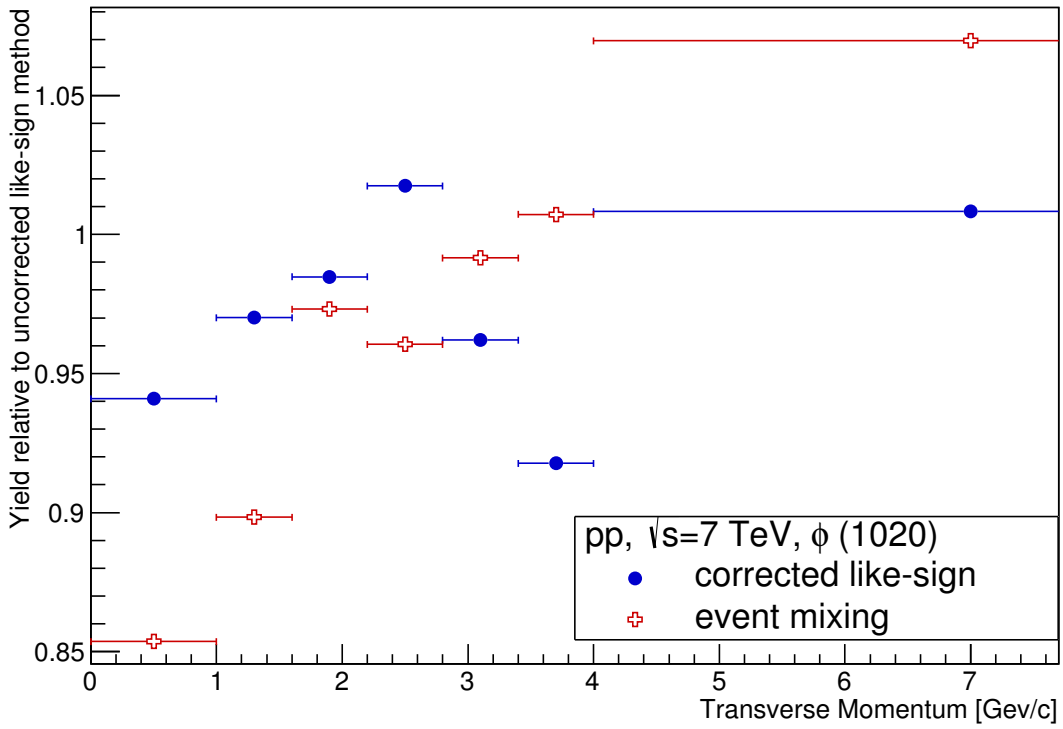

Figure D.10: $\phi(1020)$ relative yield for different p_T bins. Inverted weights have been applied to mix events. Errors only indicate the bin sizes.

D.2 $K^{*0}(892)$ resonance, weighted

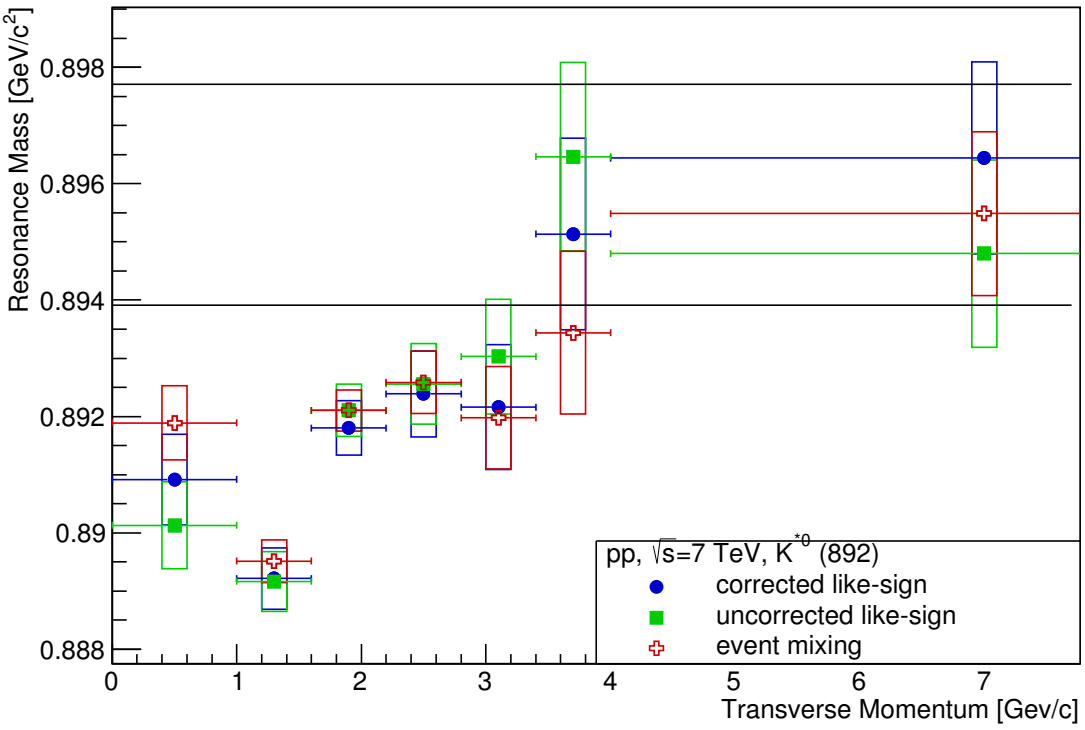

Figure D.11: $K^{*0}(892)$ mass determined by Breit-Wigner peak for different p_T bins. Weights have been applied to mix events. Errors are only statistical.

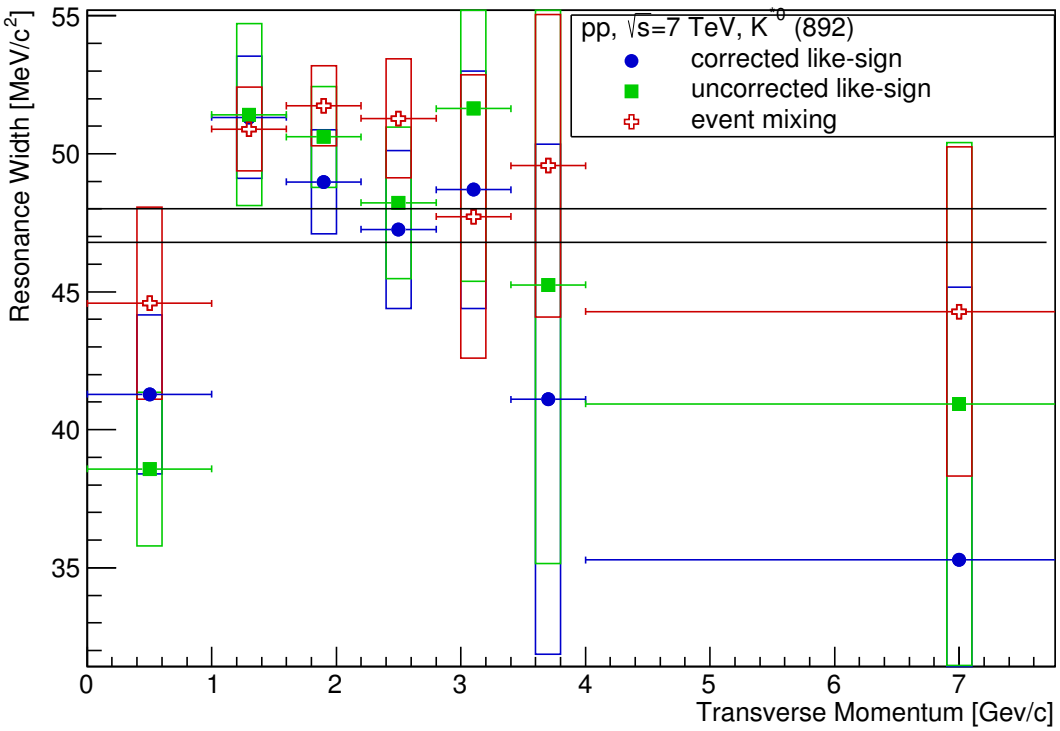

Figure D.12: $K^{*0}(892)$ width of Breit-Wigner peak for different p_T bins. Weights have been applied to mix events. Errors are only statistical.

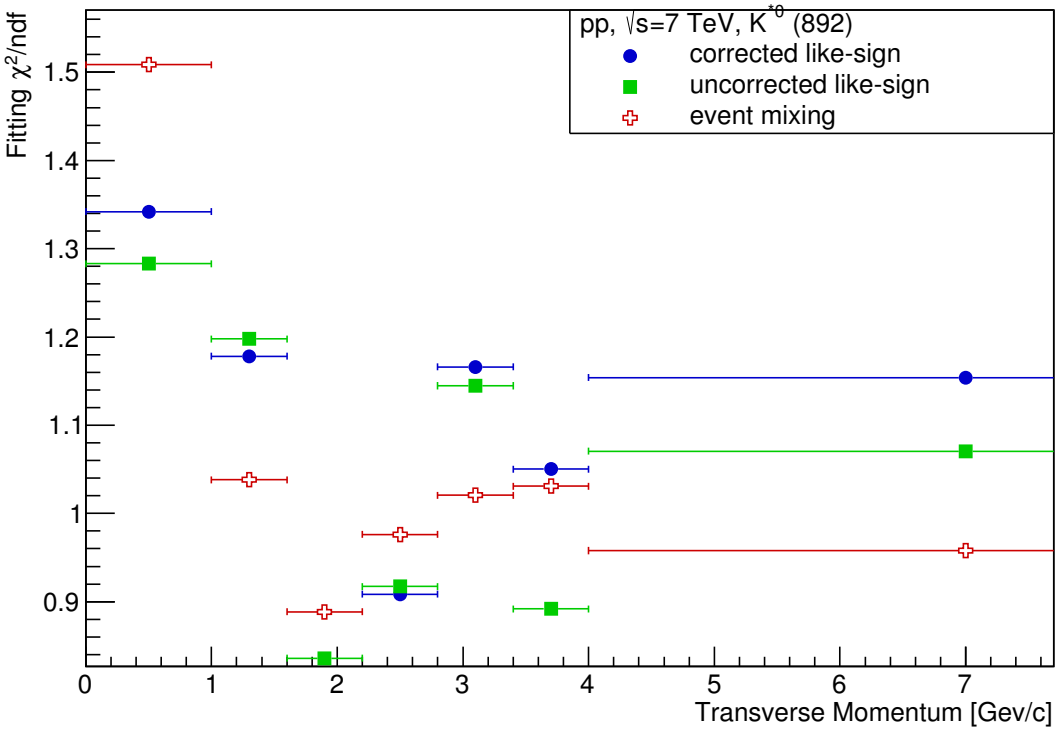

Figure D.13: $K^{*0}(892)$ fitting quality of Breit-Wigner peak and additional polynomial background for different p_T bins. Weights have been applied to mix events. Lower implies a better fit. Errors only indicate the bin sizes.

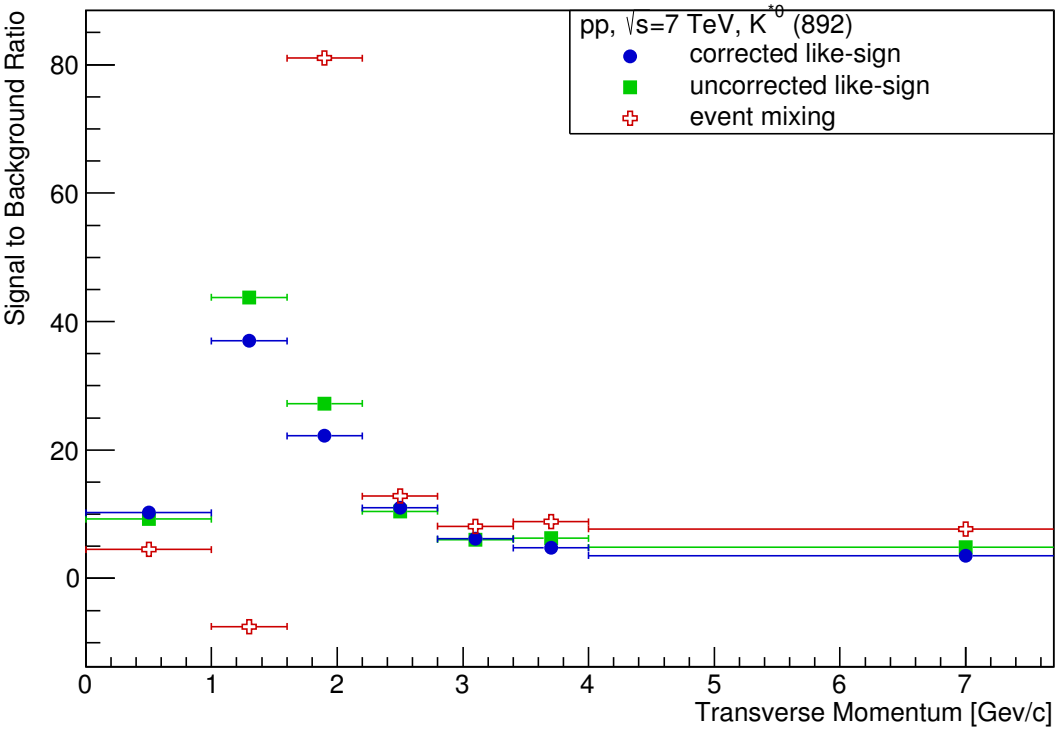

Figure D.14: $K^{*0}(892)$ signal to residual-background ratio for different p_T bins. Weights have been applied to mix events. Higher implies a better signal extraction. Errors only indicate the bin sizes.

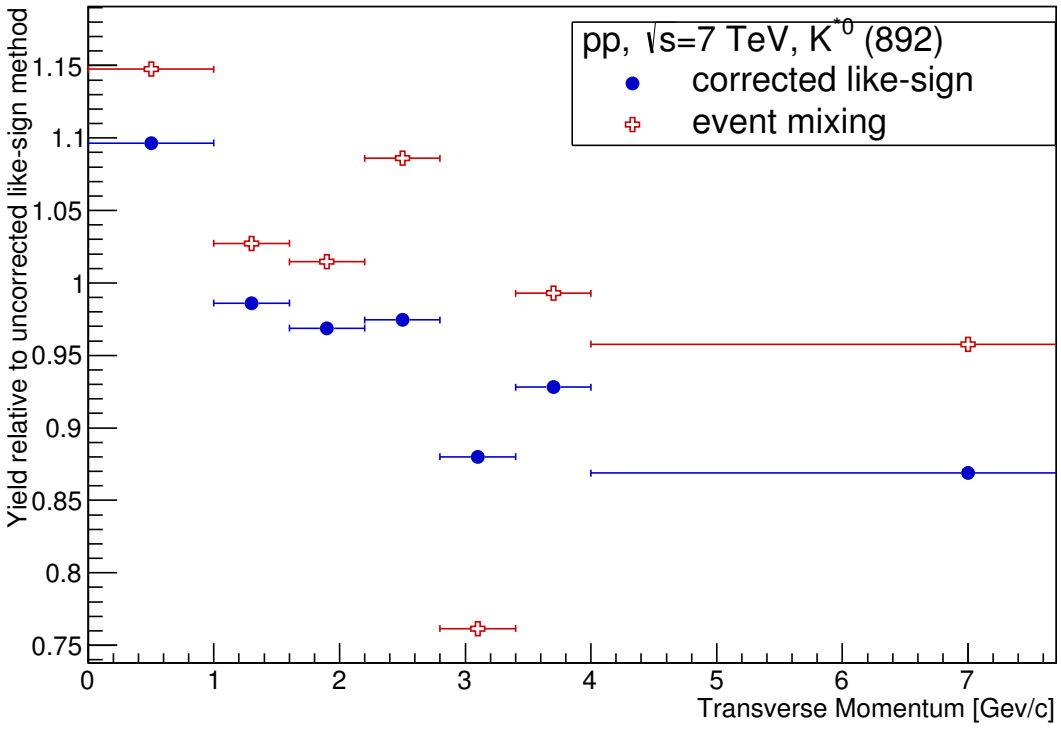

Figure D.15: $K^{*0}(892)$ relative yield for different p_T bins. Weights have been applied to mix events. Errors only indicate the bin sizes.

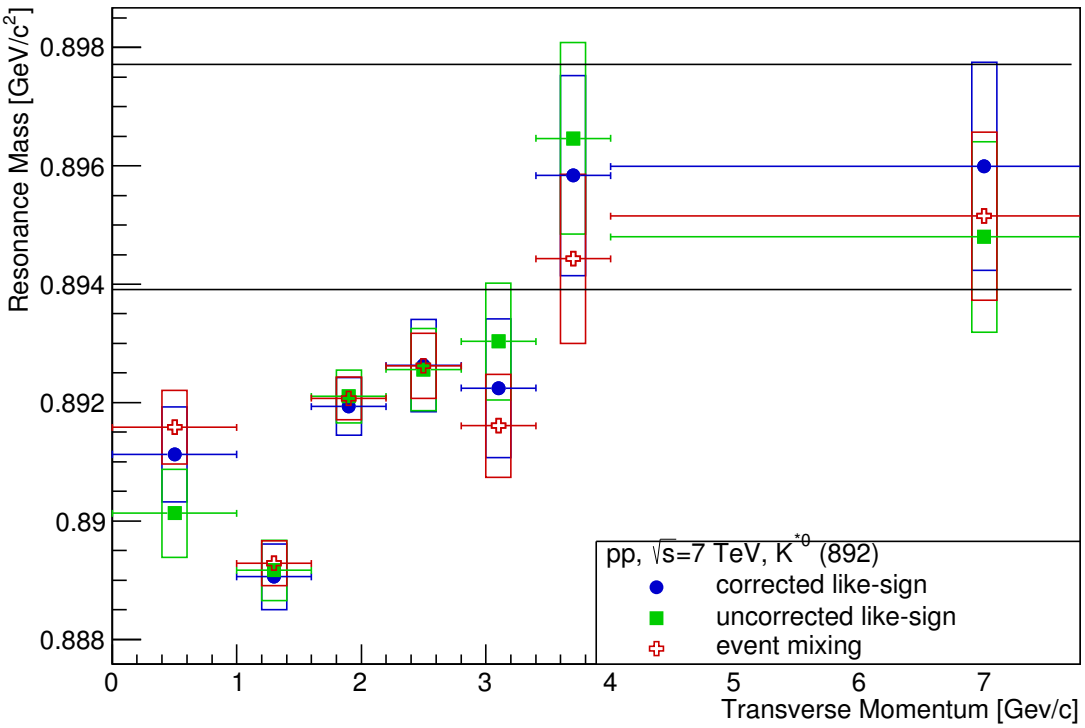

Figure D.16: $K^{*0}(892)$ mass determined by Breit-Wigner peak for different p_T bins. Inverted weights have been applied to mix events. Errors are only statistical.

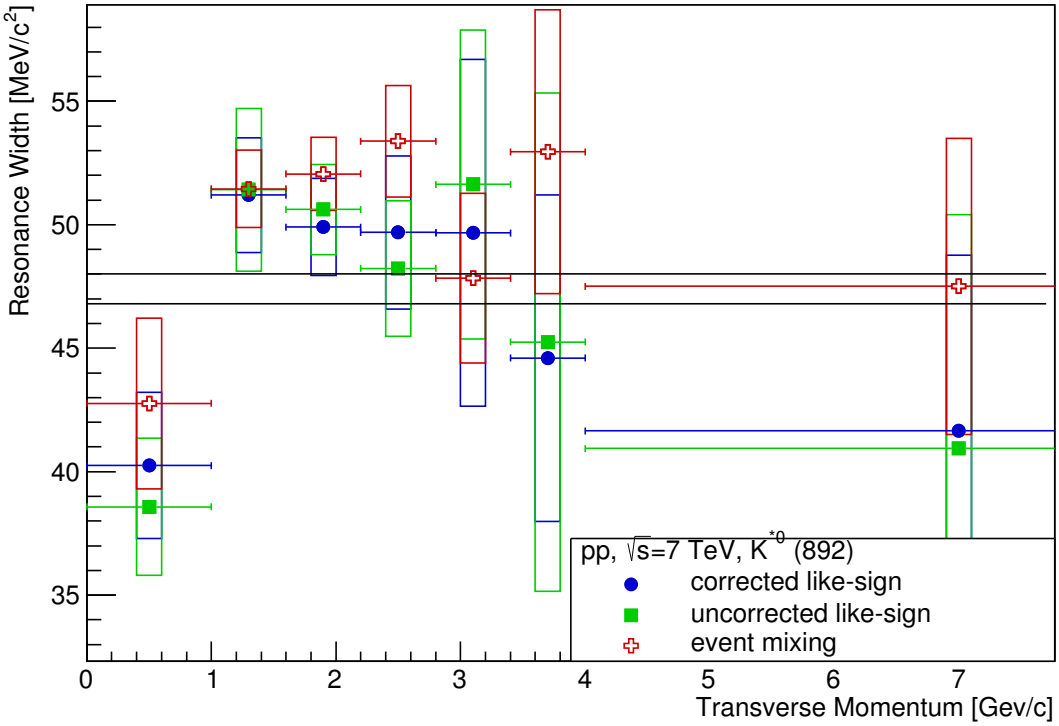

Figure D.17: $K^{*0}(892)$ width of Breit-Wigner peak for different p_T bins. Inverted weights have been applied to mix events. Errors are only statistical.

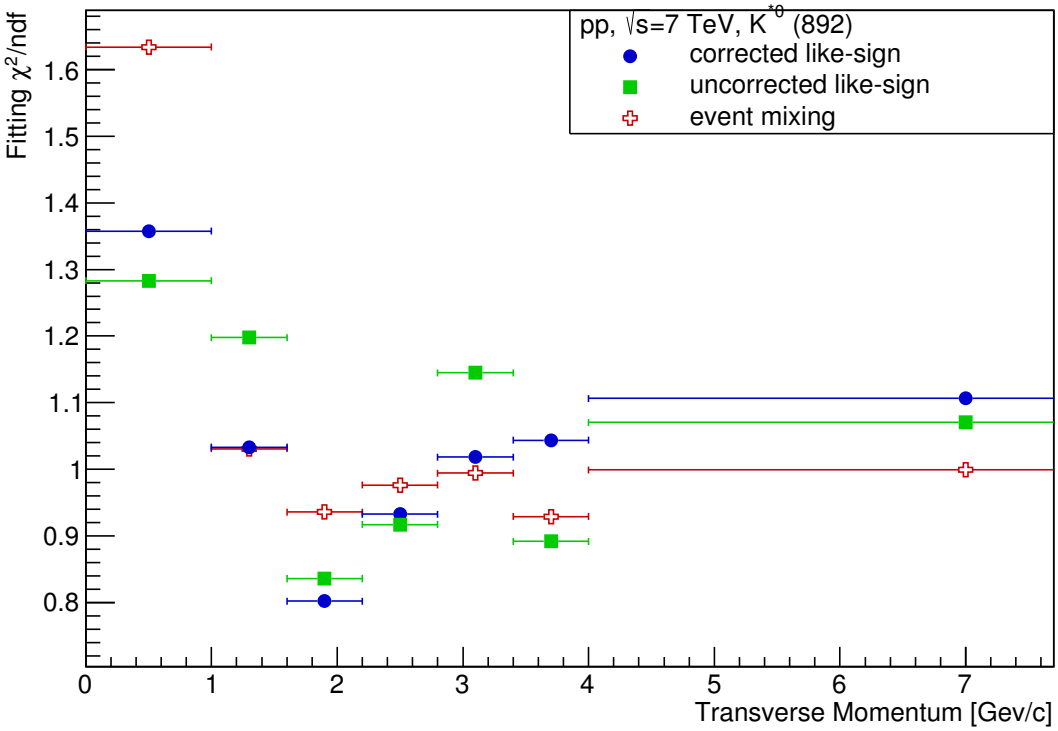

Figure D.18: $K^{*0}(892)$ fitting quality of Breit-Wigner peak and additional polynomial background for different p_T bins. Inverted weights have been applied to mix events. Lower implies a better fit. Errors only indicate the bin sizes.

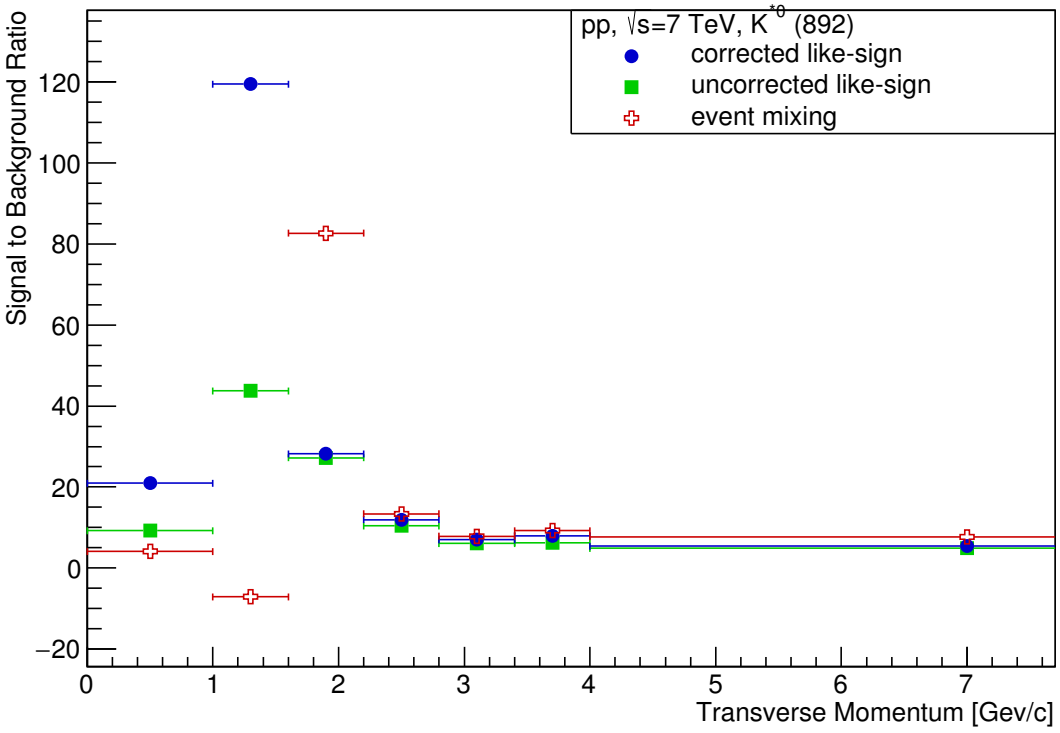

Figure D.19: $K^{*0}(892)$ signal to residual-background ratio for different p_T bins. Inverted weights have been applied to mix events. Higher implies a better signal extraction. Errors only indicate the bin sizes.

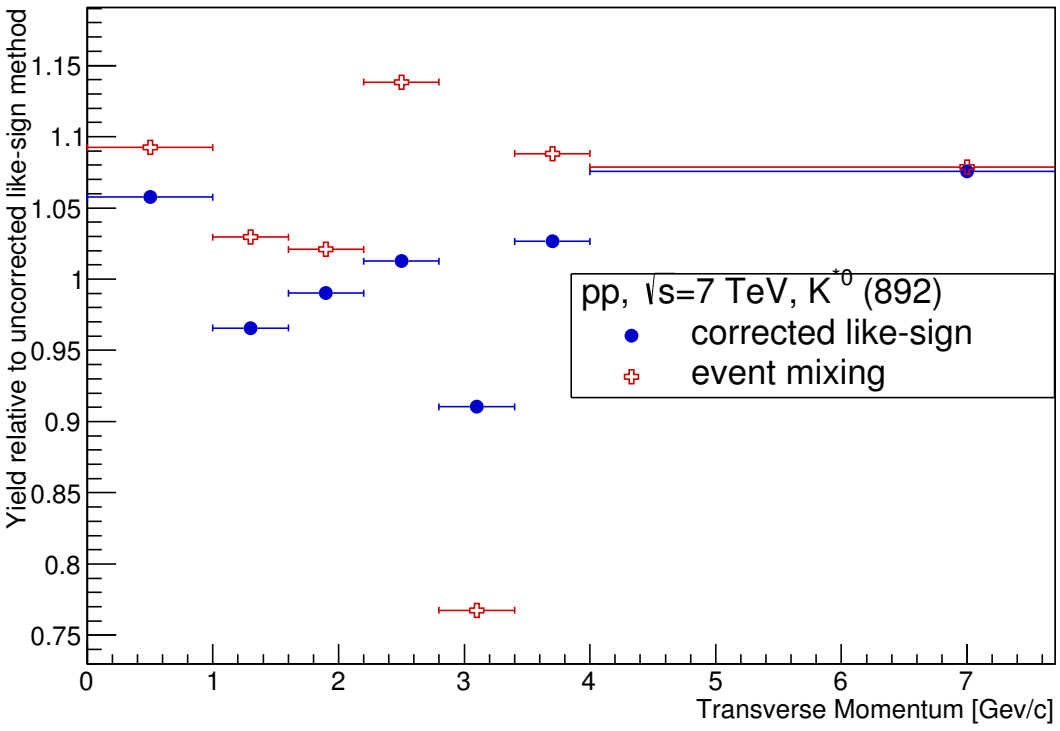

Figure D.20: $K^{*0}(892)$ relative yield for different p_T bins. Inverted weights have been applied to mix events. Errors only indicate the bin sizes.

APPENDIX E

Binning Effect

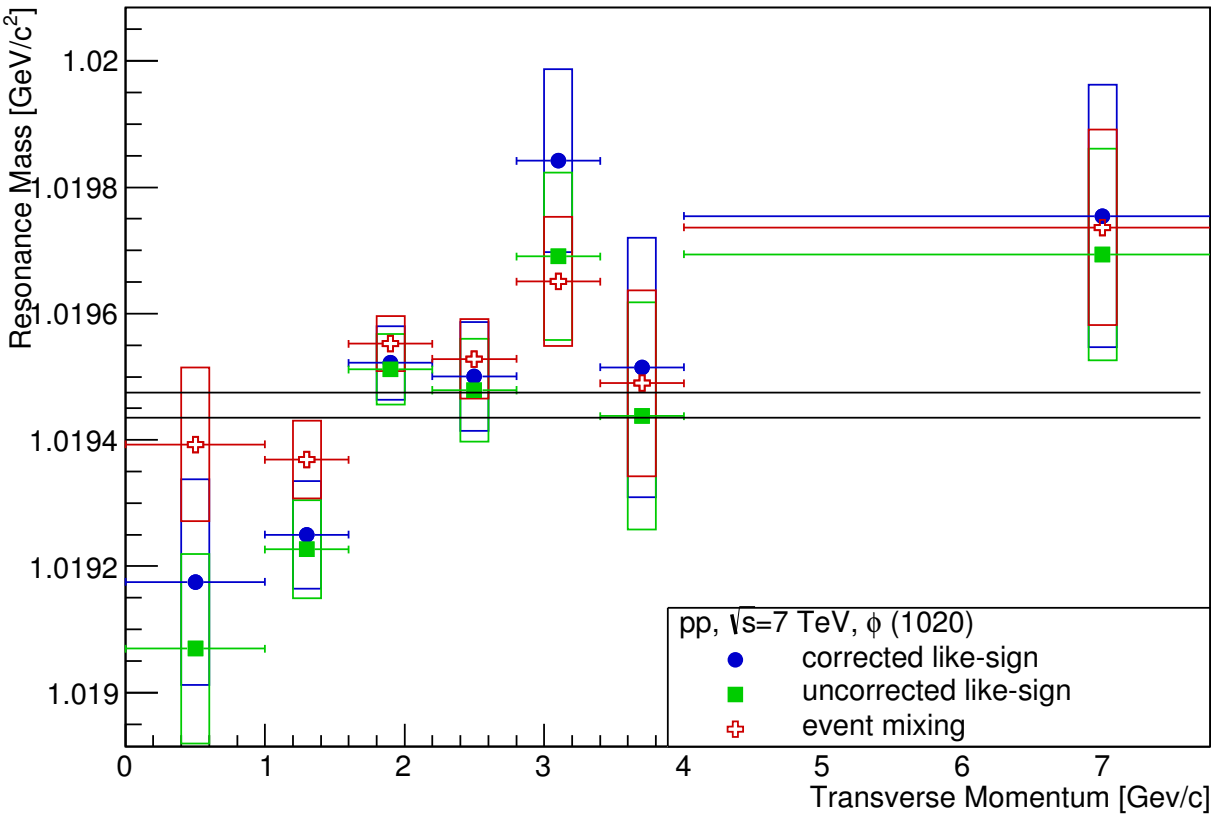

Figure E.1: $\phi(1020)$ mass determined by Breit-Wigner peak for different p_T bins. Binning size has been increased by a factor of four. Errors are only statistical.

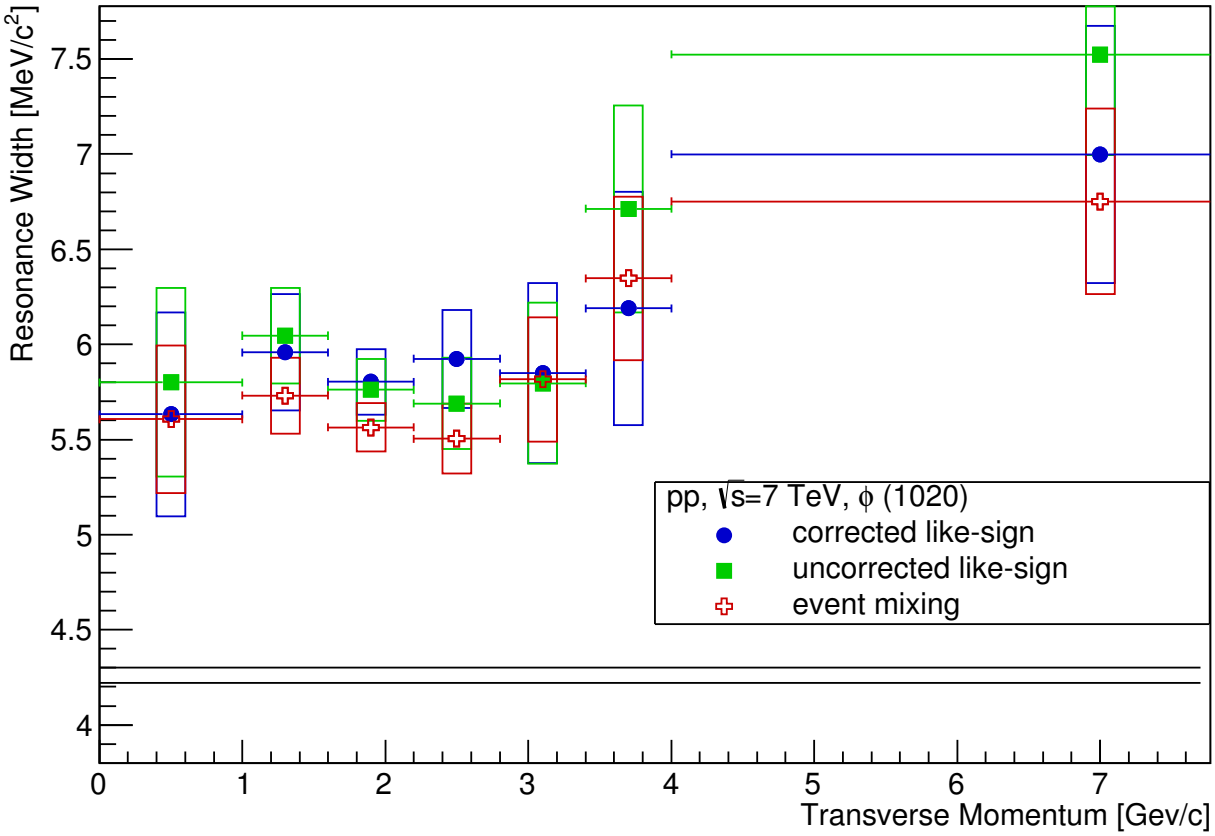

Figure E.2: $\phi(1020)$ width of Breit-Wigner peak for different p_T bins. Binning size has been increased by a factor of four. Errors are only statistical.

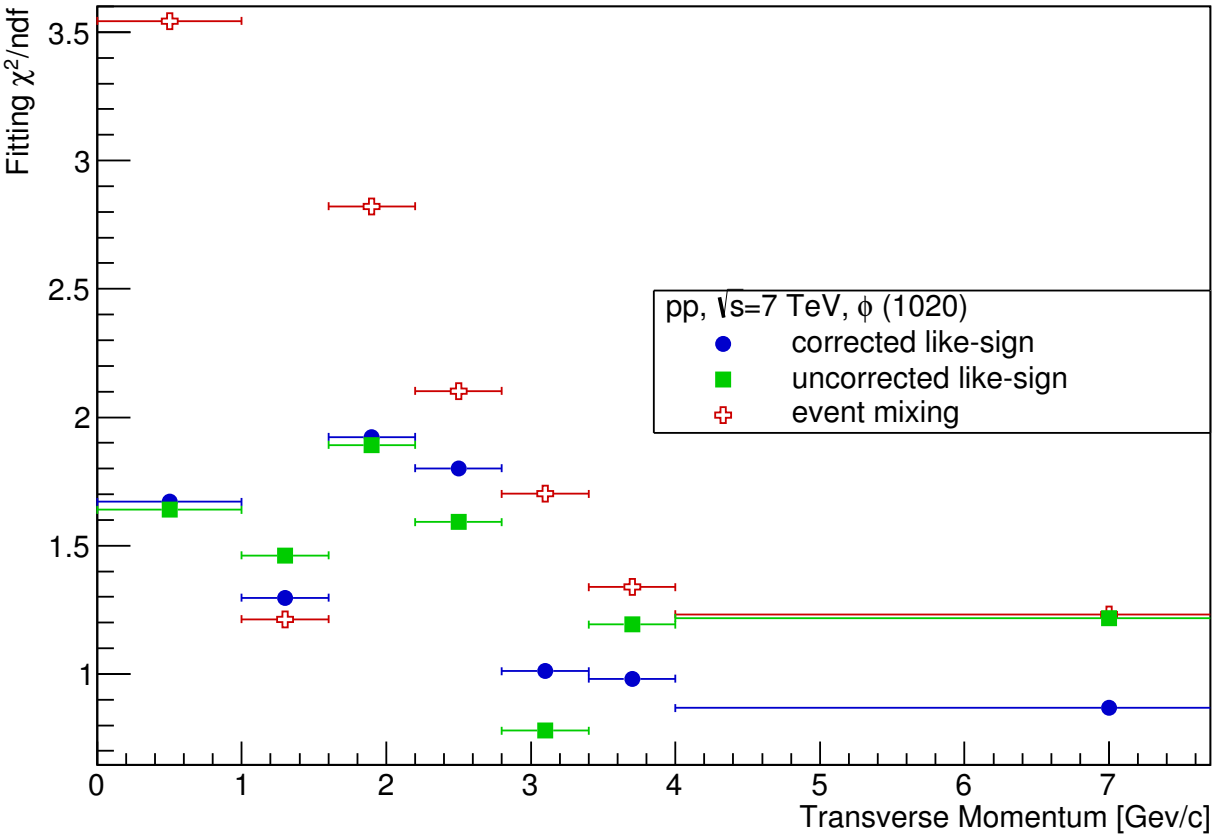

Figure E.3: $\phi(1020)$ fitting quality of Breit-Wigner peak and additional polynomial background for different p_T bins. Lower implies a better fit. Binning size has been increased by a factor of four. Errors only indicate the bin sizes.

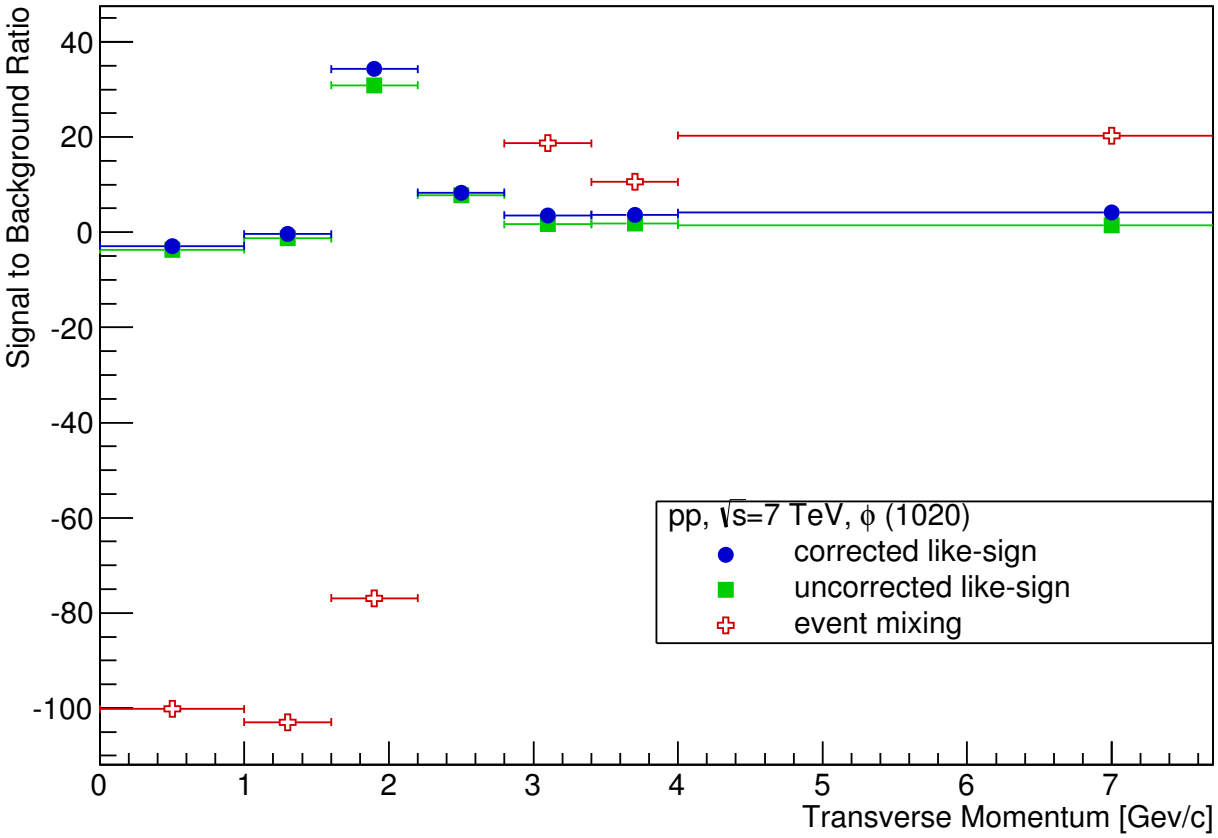

Figure E.4: $\phi(1020)$ signal to residual-background ratio for different p_T bins. Higher implies a better signal extraction. Binning size has been increased by a factor of four. Errors only indicate the bin sizes.

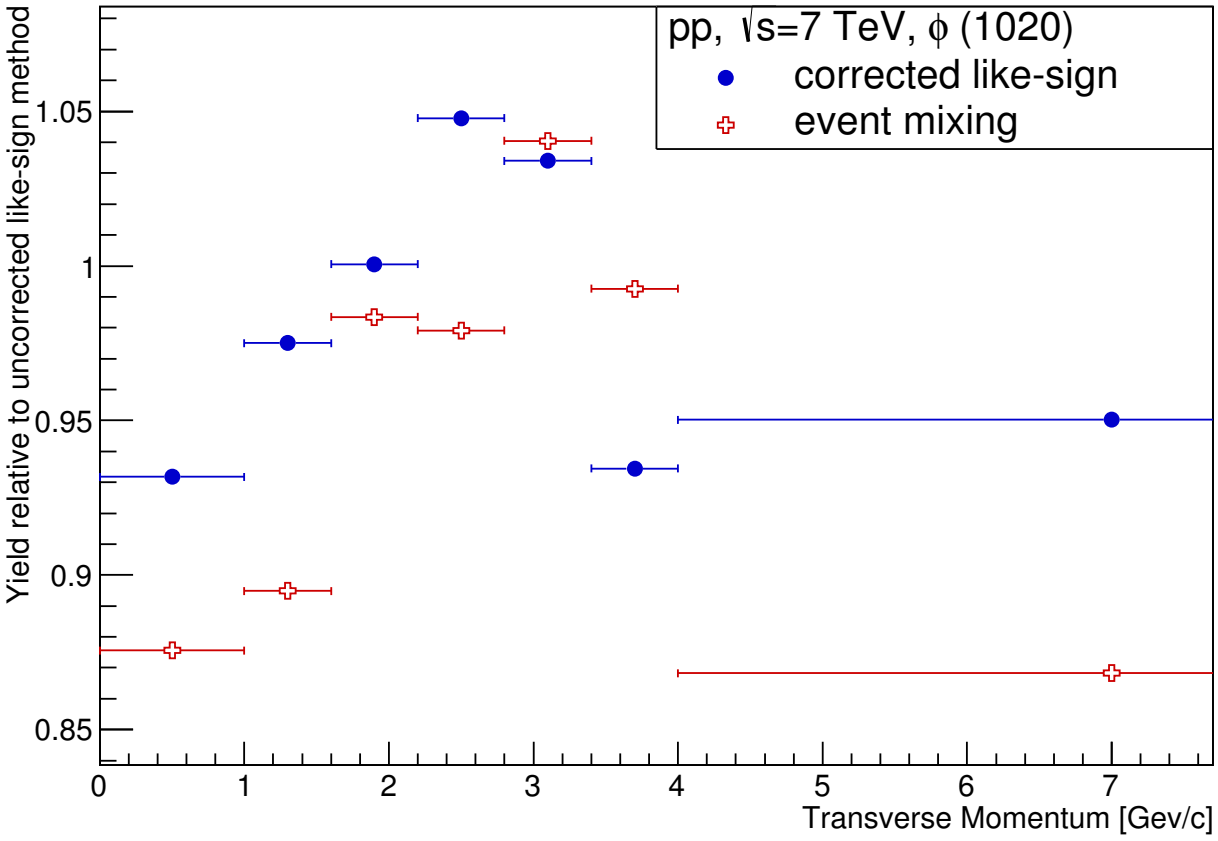

Figure E.5: $\phi(1020)$ relative yield of corrected like-sign and event-mixing method to uncorrected like-sign. Binning size has been decreased by a factor of four. Errors only indicate the bin sizes. Errors only indicate the bin sizes.

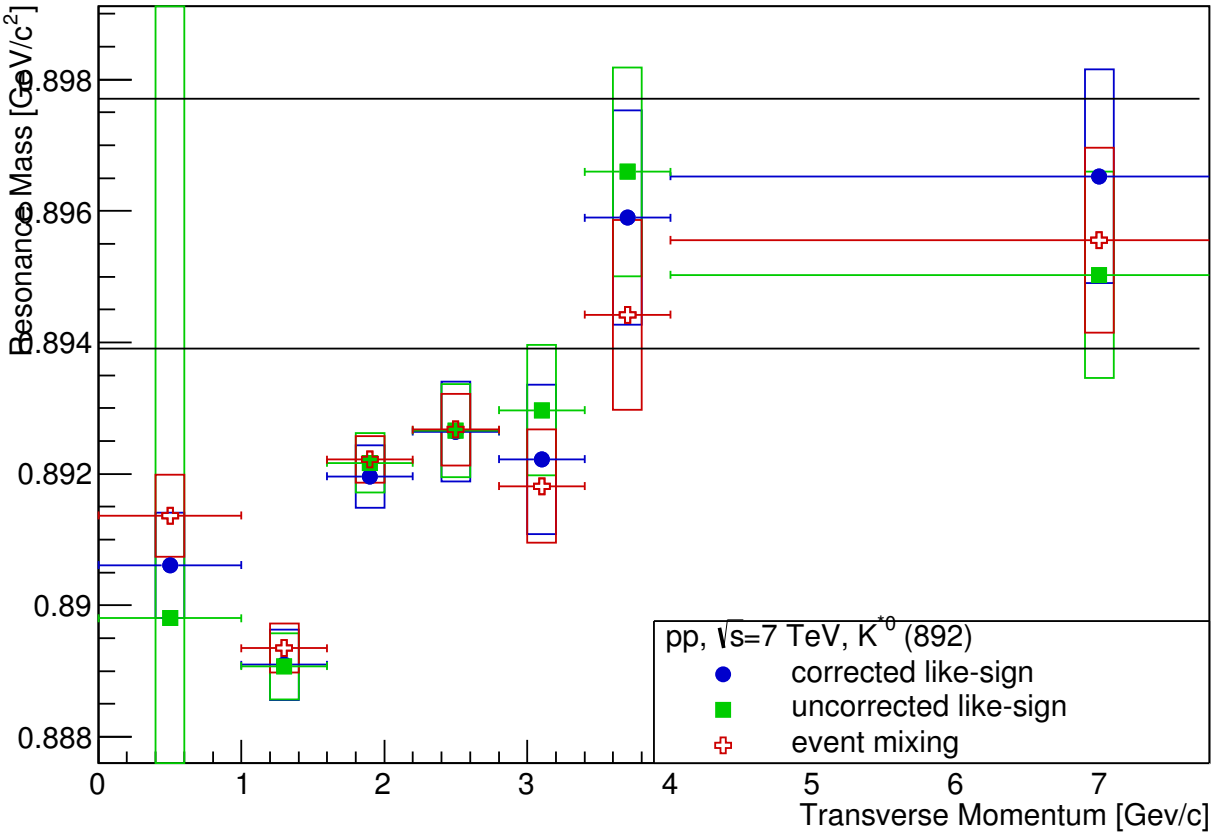

Figure E.6: $K^{*0}(892)$ mass for different p_T bins. Binning size has been decreased by a factor of four. Errors are only statistical.

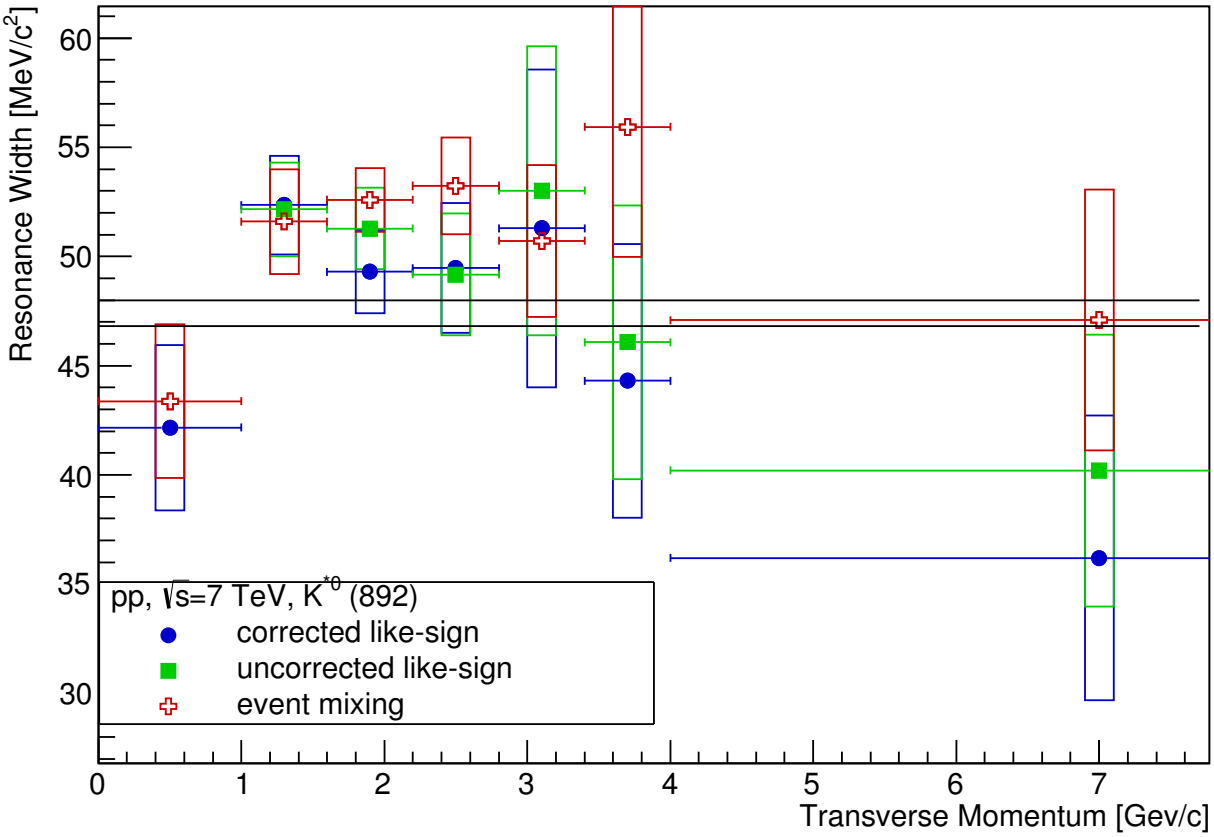

Figure E.7: $K^{*0}(892)$ width for different p_T bins. Binning size has been decreased by a factor of four. Errors are only statistical.

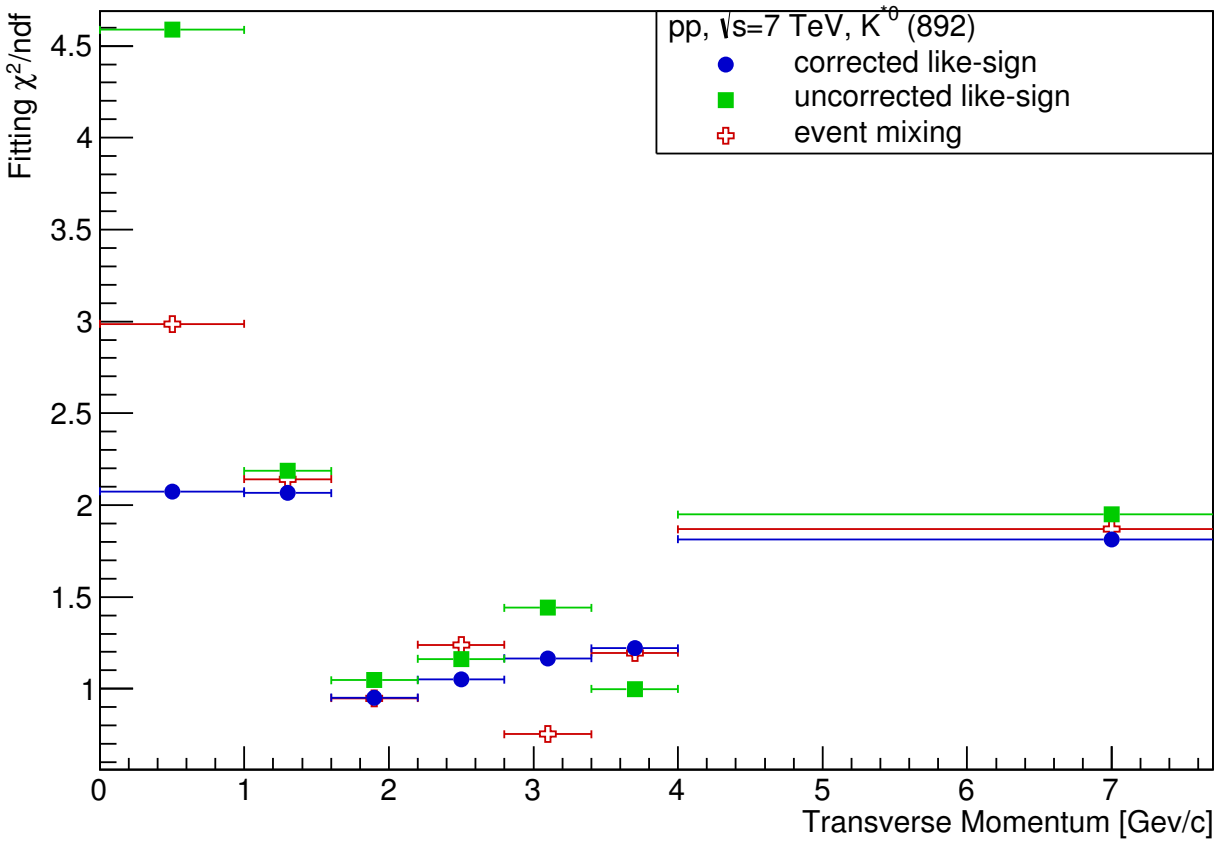

Figure E.8: $K^{*0}(892)$ fitting quality of Breit-Wigner peak and additional polynomial background for different p_T bins. Lower implies a better fit. Binning size has been decreased by a factor of four. Errors only indicate the bin sizes.

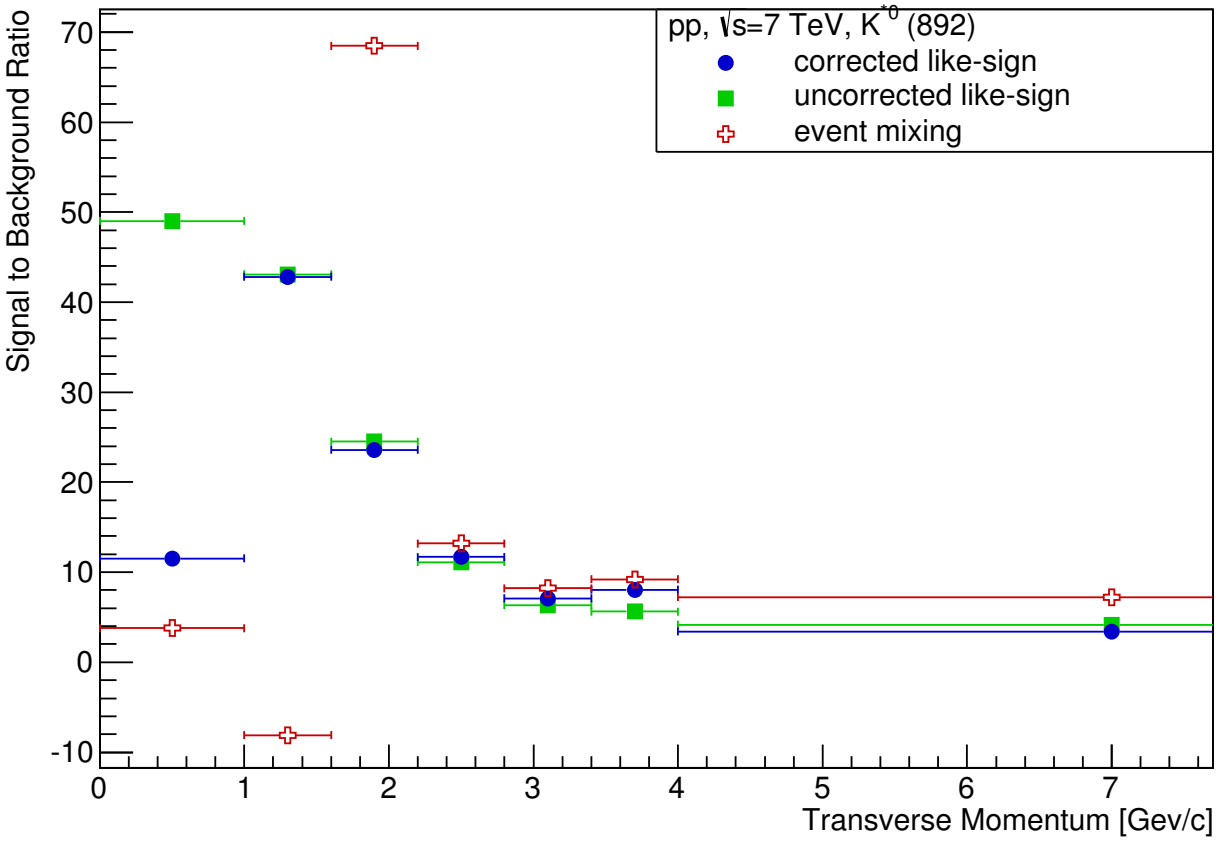

Figure E.9: $K^{*0}(892)$ signal to residual-background ratio for different p_T bins. Higher implies a better fit. Binning size has been decreased by a factor of four. Errors only indicate the bin sizes.

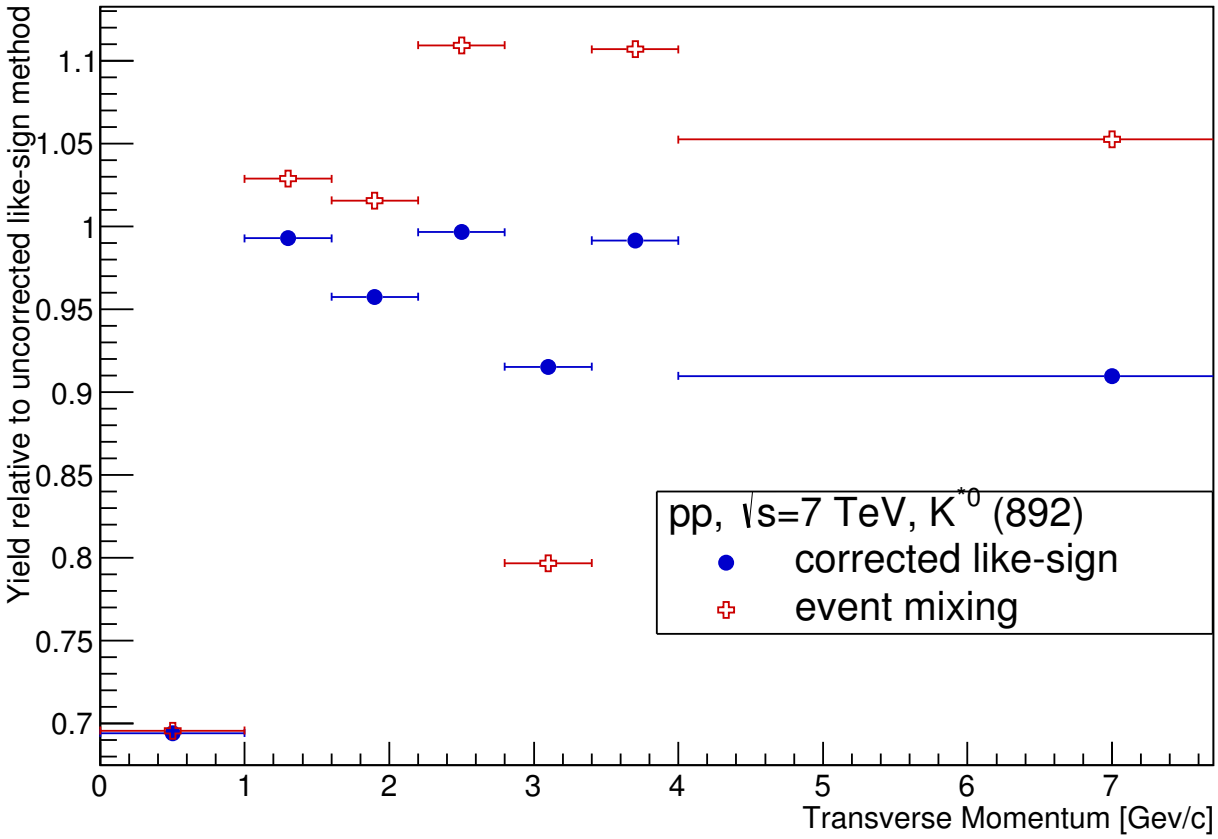

Figure E.10: $K^{*0}(892)$ relative yield of corrected like-sign and event-mixing method to uncorrected like-sign. Binning size has been decreased by a factor of four. Errors only indicate the bin sizes.